

Dissertation

submitted to the
Combined Faculties for the Natural Sciences and for Mathematics
of the Ruperto-Carola University of Heidelberg, Germany
for the degree of

Doctor of Natural Sciences

Put forward by

Dipl.-Phys. Rolf Bühler

born in Rüsselsheim

Oral examination: 28 January 2009

Two exceptional flares of the active galaxy PKS 2155-304
at Very High Energy γ -rays and their implications on
blazar and fundamental physics

Referees: Prof. Dr. Werner Hofmann
Prof. Dr. Heinrich Völk

Abstract

In this work an analysis and interpretation of the Very High Energy (VHE, photon energy > 200 GeV) γ -ray emission measured from the Active Galactic Nuclei (AGN) PKS 2155-304 is presented. The observations were carried out with the H.E.S.S. telescopes between 2005 and 2007. The source underwent two exceptional flares during this period, on 28 and 30 July 2006. The fluxes observed during these nights are among the highest ever observed in VHE astronomy and provided a very rich dataset. During the first flare the source showed a very fast flux variability (~ 200 s). No time delays could be observed between the emission at different photon energy bands; this lack of dispersion is used to set limits on the energy scale of Lorentz Invariance violations. The second flare was observed simultaneously by the Chandra X-ray satellite, yielding an unprecedented multi-wavelength view on this object. The most striking result of this night is a cubic decay of the γ -ray flux as a function of the X-ray flux. Such a correlation can not be explained with current blazar models and points towards an X-ray emission from multiple regions within the AGN.

Kurzfassung

In dieser Arbeit werden Messungen der Hochenergie γ -Strahlung (Photon Energie > 200 GeV) von der Aktiven Galaxie PKS 2155-304 präsentiert und interpretiert. Die Beobachtungen wurden zwischen 2005 und 2007 mit den H.E.S.S. Teleskopen durchgeführt. Während dieser Zeit zeigte die Quelle zwei außergewöhnlich starke γ -Strahlen Ausbrüche, am 28. und 30. Juli. Die Flüsse in diesen Nächten liegen mehr als einhundert mal über dem typischen Wert für diese Quelle, und gehören zu den höchsten, die je in der Hochenergieastronomie gemessen wurden. Während dem ersten Ausbruch wurde eine starke und schnelle Flussvariabilität gemessen, die ohne zeitliche Verzögerung in allen Energiebändern gleichzeitig auftritt. Das Fehlen einer messbaren Dispersion wurde genutzt, um untere Grenzen auf die Energieskala einer möglichen Lorentz Invarianz Verletzung zu bestimmen. Während dem zweiten Ausbruch, am 30. Juli, wurden die H.E.S.S. Beobachtungen gleichzeitig mit Beobachtungen des Chandra Röntgensatelliten durchgeführt. Eine der interessantesten Ergebnisse dieser simultanen Beobachtungen ist ein kubischer Abfall des γ -Strahlen Flusses als Funktion des Röntgen Flusses. Dies kann nicht mit üblichen Blazar Modellen erklärt werden und deutet darauf hin, dass die Röntgenstrahlung aus mehreren Regionen in der Quelle stammt.

Contents

1	Active Galactic Nuclei	1
1.1	Overview	1
1.2	Active Galactic Nuclei at Very High Energies	3
1.2.1	The active galaxy PKS 2155-304	6
1.3	Physics overview	7
1.3.1	Relativistic dynamics	7
1.3.2	Shock acceleration	9
1.3.3	Photon interactions	10
1.4	Blazar emission models	13
1.4.1	Leptonic models	13
1.4.2	Hadronic models	15
1.5	The Extragalactic Background Light	16
2	H.E.S.S. and its data analysis	19
2.1	The imaging atmospheric Cherenkov technique	19
2.1.1	Imaging Atmospheric Cherenkov Telescopes	19
2.1.2	The H.E.S.S. telescopes	21
2.2	Data analysis	21
2.2.1	Event reconstruction	22
2.2.2	Background rejection	24
2.2.3	Spectrum measurement	27
2.2.4	Lightcurve measurement	28
2.2.5	Systematic errors	28
2.2.6	Data quality	29
2.2.7	Software implementation	30
3	VHE observation of PKS 2155-304 from 2005 to 2007	33
3.1	Dataset description	33
3.2	Temporal analysis	34
3.3	Spectral analysis	37
3.3.1	Time-averaged energy spectrum	37
3.3.2	Spectral variability	40
3.4	The Big Flare	41
3.4.1	Temporal analysis	41
3.4.2	Spectral analysis	42
3.4.3	Interpretation within blazar models	45
4	The Chandra Flare - An unprecedented multi-wavelength view	47
4.1	Temporal analysis	48
4.1.1	γ -ray lightcurves	48
4.1.2	Comparison with X-ray and optical lightcurves	50
4.1.3	Inter-band time lags	53

4.2	Time-resolved spectral analysis	55
4.2.1	γ -ray spectra	55
4.2.2	X-ray spectra	60
4.2.3	Spectral Energy Distributions	64
4.3	X-ray vs. γ -ray correlations	65
4.4	Summary of the main observational facts	68
4.5	Discussion	69
5	The Big Flare as a testbed of Lorentz Invariance	73
5.1	Probing an energy dependence of the speed of light	73
5.1.1	The Modified Cross Correlation function	75
5.1.2	Systematic tests	76
5.1.3	Limits on an energy dependence of the speed of light	76
6	Summary & outlook	81
A	List of Very High Energy AGN	83
B	Measurement of the cosmic-ray iron spectrum with H.E.S.S.	85
B.1	First ground based measurement of atmospheric Cherenkov light from cosmic rays	85
B.1.1	Introduction	85
B.1.2	Event selection and reconstruction	88
B.1.3	Data analysis and simulations	89
B.1.4	Systematic checks	95
B.1.5	Spectrum extraction	97
B.1.6	Summary & outlook	100
B.2	Analysis improvements since the diploma thesis	101

List of Figures

1.1	Components of an AGN	2
1.2	Radio image of Cygnus A	3
1.3	AGN detected at VHE γ -rays	4
1.4	SED of PKS 2155-304 in 2003	6
1.5	Shock acceleration sketch	10
1.6	Klein-Nishina cross section	11
1.7	SSC sketch	14
1.8	SED of the EBL	16
1.9	EBL attenuation for PKS 2155-304	17
2.1	Air-shower simulation	20
2.2	The H.E.S.S. telescopes	21
2.3	Shower reconstruction sketch	23
2.4	Hillas parameters	23
2.5	Zenith angle dependency of the energy threshold	24
2.6	Scaled-parameter distributions	25
2.7	Reflected background model	26
2.8	Spectral index assumption in the flux reconstruction	29
2.9	Trigger rate during the Big Flare	30
2.10	Data flow in H.E.S.S.	30
3.1	Total γ -ray excess in 2005-2007	34
3.2	Run-wise flux distribution in 2005-2007	34
3.3	Overview lightcurve for 2005-2007	35
3.4	Run-wise lightcurve for 2005-2007	36
3.5	Time-averaged energy spectrum in 2005-2007	38
3.6	Photon index for each observation period in 2005-2007	40
3.7	Photon index as a function of flux in 2005-2007	41
3.8	Lightcurve and power spectrum of the Big Flare	42
3.9	Energy spectrum of the Big Flare	43
3.10	Photon index over time for the Big Flare	45
4.1	VHE lightcurves in energy bands for the Chandra Flare	49
4.2	Fourier power spectrum	50
4.3	Multi-wavelength lightcurves	51
4.4	SED multi-wavelength snapshot	52
4.5	Cross-correlation for X-ray and γ -ray bands	54
4.6	γ -ray and X-ray lightcurve	55
4.7	Spectral evolution over time above 300 GeV	56
4.8	Spectral evolution over time above 500 GeV	57
4.9	Selected γ -ray spectra	57
4.10	Evolution of the X-ray spectrum over time	61
4.11	Time-averaged X-ray spectrum	62

4.12	SED in the highest and lowest state	65
4.13	Flux over time at γ -rays and X-rays	66
4.14	Correlation between X-ray and γ -ray flux	67
4.15	SED of the flaring component	70
5.1	Oversampled lightcurves of the Big Flare	75
5.2	Sketch of light-curve simulations	76
5.3	MCCF for the Big Flare	77
5.4	CCPD response to dispersion	78
5.5	Bootstrap model for simulations	78
5.6	CCPD response in bootstrap simulations	79
5.7	Blazar dispersion measurements at VHE	79
B.1	Sketch of the Direct Cherenkov detection	86
B.2	Simulated Direct Cherenkov distribution on the ground	87
B.3	Direct Cherenkov emission as a function of height and energy	88
B.4	DC-ratio as a function of energy	90
B.5	Camera images of a Direct Cherenkov event from data	92
B.6	Detected events as a function of telescope multiplicity	93
B.7	Charge reconstruction	94
B.8	Parameter distributions in comparison with simulations	96
B.9	Charge distribution in the data	98
B.10	Differential iron flux	99

List of Tables

1.1	Length scale of AGN components	3
1.2	Blazar flares in VHE γ -rays	5
2.1	Current IACTs	20
2.2	γ -ray selection cuts	26
3.1	Spectrum fit results for the 2005-2007 spectrum	39
3.2	Spectrum fit results for the Big Flare	44
4.1	Dataset description for the Chandra Flare	48
4.2	Spectral fits of absorbed spectra	58
4.3	Spectral fits of deabsorbed spectra	59
4.4	Fits to the time-averaged X-ray spectrum	63
4.5	Fit results of the X-ray and γ -ray correlation	68
A.1	Detected AGN at VHE	83
B.1	Selection parameters	89
B.2	Elemental composition of the simulated flux	90
B.3	Iron fraction in the data	97

Chapter 1

Active Galactic Nuclei

1.1 Overview

It is believed nowadays that most galaxies harbor a Super Massive Black Hole (SMBH) in their center. If the SMBH is accreting significant amounts of matter, the central few parsecs of the galaxy become very bright, often outshining the entire galaxy. The luminosity from the core region is then typically in the range of 10^{45-49} erg s⁻¹, compared to a typical 10^{44} erg s⁻¹ for the rest of the galaxy. These galaxies are then called *active galaxies*, and the luminous center the *active galactic nucleus* (AGN). About 3% of all galaxies are active. In the following some of the basic properties of AGN will be reviewed.

AGN are subdivided into two main categories, radio-quiet and radio-loud. AGN which release more energy at radio frequencies (~ 5 GHz) than in the optical B-band are assigned to the second category. About 10-15 % of AGN are radio-loud. For reasons not yet understood, almost all radio-loud galaxies are also elliptical galaxies. AGN are very multifaceted objects, therefore they have been classified in various further subclasses, on which no details are given here (see e.g. Antonucci (1993)). In the last few decades however, a unified picture of AGN has emerged, which explains the main observational differences between AGN subclasses through different viewing angles of the AGN with respect to the observer (Urry & Padovani 1995). In this unified picture AGN consist of the following constituents (see figure 1.1):

- **Black hole:** The central SMBH has a typical mass in the range of 10^6-10^9 solar masses. This can be deduced from the motions of nearby stars and gas clouds. The size of the volume in which this mass is concentrated has not yet been constrained to the point where the creation of a black hole is unavoidable, therefore in principle there still exists the possibility that some other form of very dense and non-luminous matter is located at the center of the AGN. However, other objects (such as a cluster of neutron stars or white dwarfs) would not be stable over the lifetime of a galaxy (~ 10 Gyrs), leaving the black hole as the most likely candidate. Usually, the mass of the SMBH scales with the luminosity and velocity dispersion of the bulge of the galaxy (Ferrarese & Ford 2005; Bettoni et al. 2003).
- **Accretion disk:** The matter accreted by the black hole forms an accretion disk extending to $\sim 100-1000$ Schwarzschild radii ($R_S = \frac{2GM}{c^2}$). The accretion disk usually dominates the radiative energy output of AGN. Its electro-magnetic spectrum is thermal, meaning that the energy spectrum follows a Plank distribution. The maximum of the emission is usually at far ultraviolet frequencies, equivalent to a temperature of $\sim 10^5$ K. Since most electrons are not bound to nuclei at these temperatures, the disk is composed of a plasma. In this plasma thermal energy is radiated away mainly by the Bremsstrahlung of free electrons.
- **Broad-line region:** The broad-line emission region shows lines from atomic transi-

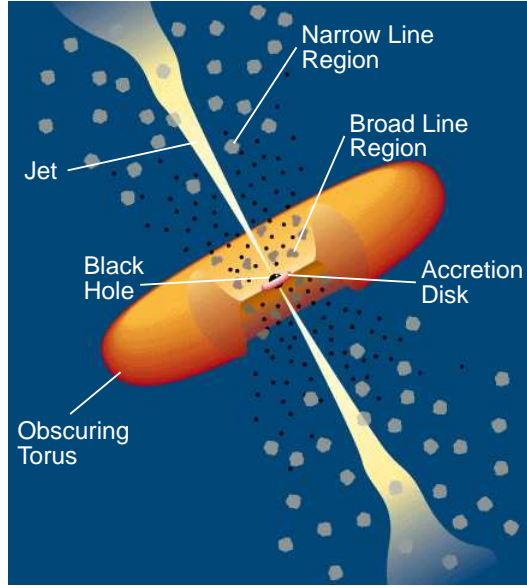


Figure 1.1: Components of an AGN (from Urry & Padovani (2008)).

tions broadened by the Doppler effect. The width of the broadening is equivalent to speeds of several thousand km s^{-1} . This is equivalent to a temperature of $\sim 10^{12}$ K. Since a temperature this high would not allow atoms to be stable, the mean components of the velocity must come from the bulk motion of gas clouds. This gas is being excited by the strong radiation coming from the accretion disk.

- **Narrow-line region:** In addition to broad emission lines, AGN often also exhibit much narrower lines, with a width equivalent to a velocity spread of $200\text{--}2000 \text{ km s}^{-1}$. They also originate gas clouds which are illuminated by the central region of the AGN.
- **Torus:** The accretion disk of an AGN is often surrounded by a dust torus. This torus absorbs the emission from the central region of the AGN and re-emits the energy at infrared frequencies.
- **Jets:** Radio-loud AGN show jet structures coming out into opposite directions from the central region (see figure 1.2). These jets have a featureless continuous spectrum, with strong emission from radio to X-ray frequencies. At radio and optical frequencies the emission is polarized. Inside of jets one can often resolve smaller structures, so-called “knots”. The velocity of these structures can be measured directly, showing that they have Lorentz factors up to ~ 30 . Jets are collimated outflows of plasma; to date, the exact composition of the plasma remains unclear (e.g. electrons and positrons or electrons and protons). It is also unclear how jets are created and collimated over such large distances, although it is generally thought that jets are created because the rotating plasma in the accretion disk produces a spiral magnetic field perpendicular to the disk, which forces the plasma above and below the disk to co-rotate with it (Blandford & Payne 1982). If the centrifugal force has a component in the direction of the magnetic field lines, the particles are accelerated outwards, producing the jet (an analogy often used to illustrate this mechanism are beads on rotating wires). Other models of jet creation have also been proposed (see e.g. Blandford & Znajek (1977)).

The large energy output of AGN is powered by the gravitational energy of the in-falling matter. The potential energy of the in-falling matter can be converted very efficiently into radiation energy in accretion processes. This can be seen as follows: imagine a mass m falling

Table 1.1: Typical size of the components of an AGN (from Rosswog & Brüggen (2007))

Component	Typical size [pc]
Black hole (R_S for $10^9 M_\odot$)	0.0001
Accretion disk	0.01
Broad-line region	1
Dust torus	10
Narrow-line region	1000
Host galaxy	10000
Jet	$\leq 10^6$

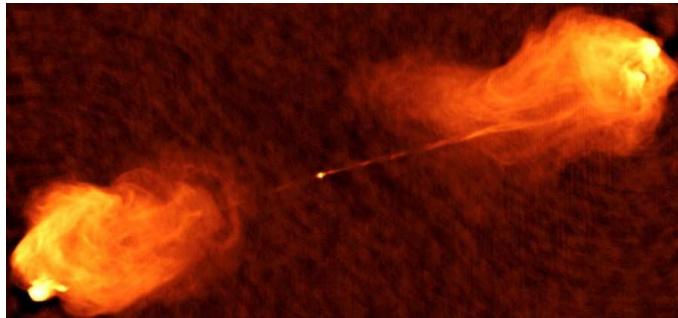


Figure 1.2: Radio image at 5 GHz of the active galaxy Cygnus A. The source is located at a redshift of 0.06 and the length of each jet is ~ 100 kpc (from Perley et al. (1984)).

into the accretion region from infinity onto a mass M . Its potential energy will transform to kinetic energy. Once the particle is stopped due to a collision at a radius R this energy will be converted into thermal energy, which is then radiated away. A mass accretion rate \dot{m} will therefore result in a luminosity L given by:

$$L = \frac{GM\dot{m}}{R} = \frac{1}{2} \frac{R_S}{R} \dot{m} c^2 = \xi \dot{m} c^2. \quad (1.1)$$

This process can result in an energy output comparable to the rest mass energy of the in-falling matter for small R . For accretion into black holes an efficiency $\xi \sim 0.3$ can be reached (for comparison the efficiency of nuclear fusion of hydrogen is only $\xi \sim 0.007$). It should be noted that the mass accretion rate cannot increase indefinitely, since at some point the radiative pressure will prevent further matter from falling into the accretion region. In reality there exists an upper limit on the possible luminosity if the source is in a state of equilibrium, the so-called *Eddington luminosity* (see e.g. Rosswog & Brüggen (2007)).

1.2 Active Galactic Nuclei at Very High Energies

At Very High Energy γ -rays (VHE, energies >100 GeV, in the following just referred to as γ -rays) 23 AGN have been detected to date (November 2008). Their distribution on the sky is shown in figure 1.3, together with their redshift (see table A.1 in the appendix for the discovery year and publication). With the exception of M 87, all belong to the blazars class. In this AGN subclass, the jet is pointing directly towards earth. The emission from the jet is therefore strongly Doppler boosted (see section 1.3.1) and usually dominates the electro-magnetic emission of these sources. Blazars usually show a strong flux variability in all wavebands on time scales from years to minutes.

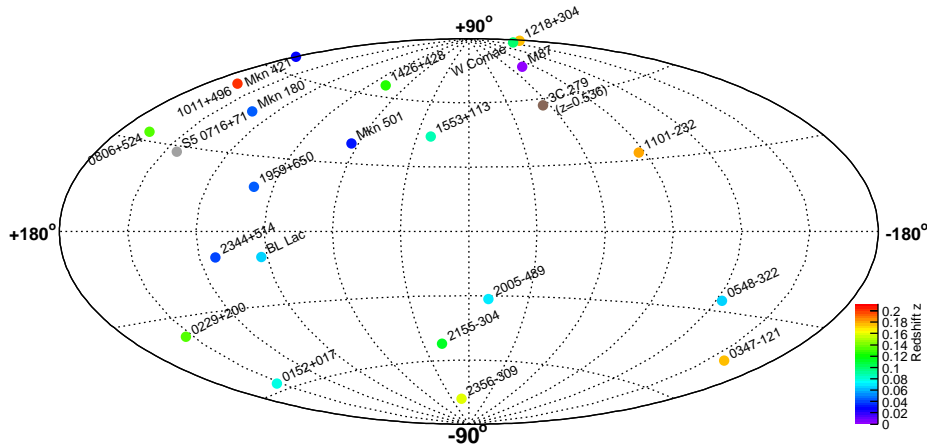


Figure 1.3: Coordinates of all AGN detected at VHE γ -rays to date in Galactic coordinates. The color indicates the redshift of the sources (from Wagner (2008)).

The Spectra Energy Distribution (SED) of blazars is characterized by two broad non-thermal components, one example of which is shown in figure 1.4. The first component typically peaks at meV-keV energies, whereas the second one peaks in the keV-TeV regime. It is thought that this double-humped structure is produced by synchrotron and Inverse Compton emission of relativistic electrons. Therefore – even though alternative models explaining this structure exist – the low and high energy bump are generally referred to as the *synchrotron* and the *Inverse Compton component* respectively. A more detailed discussion of the different emission processes and models will be given in sections 1.3 and 1.4.

At VHE the differential energy spectrum of blazars is usually steep and can be well described by a power law with a photon index around three. The typical flux from these objects corresponds to $\sim 2\%$ of the flux from the Crab Nebula¹. This flux value is however most likely not related to any physical constraint, but rather to the sensitivity of current VHE telescopes (see section 2.1.1). It is difficult to compare average flux levels of blazars at VHE, since they show a particularly strong flux variability in this energy regime. Additionally, for most of the detected sources, only a few tens of hours of observations have been performed. However, VHE observations in the last decade have shown that generally three AGN are significantly brighter than the others at VHE: Mkn 401, Mkn 501 and PKS 2155-304. These sources have typical flux values of a few tens of the Crab Nebula flux.

Particularly interesting for blazar observations are epochs of highly increased flux levels, so called flares. In these periods, which can last from hours to months, the VHE emission is often increased by up to an order of magnitude with respect to the typical values. During flares, the increased flux levels enable VHE instruments to resolve flux and spectral variability with more accuracy, giving a more detailed insight into the physical processes responsible for the VHE emission during these most violent periods. A list of the brightest historic VHE flares is given in table 1.2. During these flares some general properties of the VHE emission have emerged:

- A correlation between γ -ray and X-ray flux.
- A spectral hardening with increasing γ -ray flux.

The correlation between γ -rays and X-rays has led to the idea that both are emitted by

¹The Crab Nebula is the brightest steady source in the sky in VHE γ -rays. It has a flux of $\approx 2 \times 10^{-11}$ photons $\text{cm}^{-2} \text{s}^{-1}$ above 1 TeV (Aharonian et al. 2006a) and is usually used as a reference flux in VHE astronomy.

Table 1.2: Major historic flares of blazars at VHE γ -rays. F_{\max} denotes the maximum flux observed in units of the flux of the Crab Nebula, τ_{\min} is the smallest time scale at which flux variability was resolved. Both of the mentioned quantities should only be used as rough guidelines, as F_{\max} depends on the energy threshold of the observation and τ_{\min} is usually not quantified in an uniform way between measurements. The references for the different measurements in order of their listing are: Gaidos et al. (1996), Fossati et al. (2008), Aharonian et al. (1999b), Albert et al. (2007), Krawczynski et al. (2004). The flaring period of PKS 2155-304 will be presented in this work (chapters 3-5).

Source	Year	F_{\max}	τ_{\min}	Comment
Mkn 421	1996	10	15 min	- First detected γ -ray flare
	2001	5	15 min	- One week of high activity - Quadratic increase of γ -ray flux with X-ray flux in one night - Indication for time delay between γ -rays and soft X-rays in one night
Mkn 501	1997	10	10 h	- Six months of high activity
	2005	5	10 min	- Two months of high activity - Indication for a delay of high- to low-energy γ -rays during one night
1ES 1959-650	2002	5	1 h	- Two months of high activity - Bright γ -ray flare with no X-ray counterpart during one night
PKS 2155-304	2006	15	2 min	- One month of high activity - Major flares in two nights

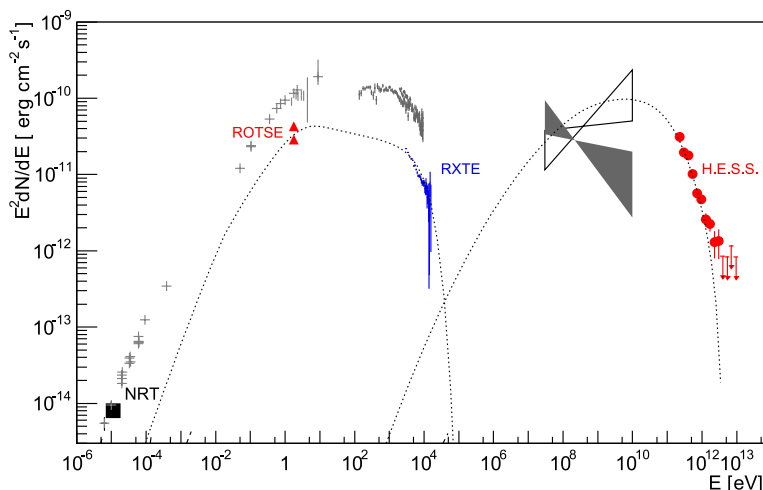


Figure 1.4: Average SED of PKS 2155-304 during a multi-wavelength campaign from October to November 2003. Only simultaneously taken data are labeled. The measurements were performed by the X-ray satellite RXTE (blue), the optical telescope ROTSE (red triangles), the radio telescope NRT (black square) and the VHE experiment H.E.S.S. (red circles). In this representation, equal Y-values denote equal energy output per decade of energy. The dotted line shows a Synchrotron Self Compton (SSC) model described in Aharonian et al. (2005b) (an additional radiation component needs to be introduced to explain the radio data). SSC models will be introduced in section 1.4.1. This figure was adapted from Aharonian et al. (2005b).

the same population of electrons (see section 1.4). However, it should be noted that there are also observations showing a more complex behavior. Particularly the γ -ray and X-ray flux do not always correlate, seen most evidently in the so called “orphan flare” of 1ES 1959-650 in 2002, where a γ -ray flux increase of a factor of ten was not accompanied by any measurable increase in the X-ray flux (see table 1.2). In this work, an exceptional flaring period of the blazar PKS 2155-304 will be presented. This flare reached its maximum brightness in the nights 28 and 30 July in 2006, where the source exhibited some of the highest flux values ever recorded at VHE γ -rays. These two flares will be referred to as the *Big Flare* (28 July) and the *Chandra Flare*² (30 July) throughout this work. In the following this source will be briefly introduced.

1.2.1 The active galaxy PKS 2155-304

The active galaxy PKS 2155-304 is located at a redshift of $z = 0.116$ (Falomo et al. 1993). The luminosity of the host galaxy is $M_R = -24.4$ (Kotilainen et al. 1998). From this luminosity a putative estimate of the mass of the central black hole of $1 - 2 \times 10^9$ solar masses can be derived (Aharonian et al. 2007b). The source belongs to the class of high frequency peaked BL Lac objects. This subclass of blazars is characterized by the high energy of the maximum of their synchrotron and Inverse Compton SED components, typically around ~ 0.1 keV and ~ 100 GeV respectively.

PKS 2155-304 was discovered in 1979 by the HEAO 1 X-ray satellite (Griffiths et al. 1979). It is one of the brightest extragalactic X-ray sources on the sky and it is regularly

²The name “Chandra Flare” was chosen since this flare occurred during simultaneous observations with the X-ray satellite *Chandra*. The name “Big Flare” was chosen directly after the event, since at this time it showed the highest VHE fluxes ever measured from this source. In retrospective, this name might be somewhat confusing, as the peak fluxes during the *Chandra Flare* are actually higher, as will be seen in chapter 3.

observed by X-ray instruments (Brinkmann et al. 1994; Chiappetti & Torroni 1997; Vestrand & Sreekumar 1999; Nicastro et al. 2002). The maximum power of the source is usually emitted in the UV and soft X-ray range (Wandel & Urry 1991). The Inverse Compton component of its SED was first detected at GeV energies by the *EGRET* detector on board the *Compton Gamma Ray Observatory* in 1995 (Vestrand et al. 1995). At VHE γ -rays, PKS 2155-304 was first detected in 1999 by the University of Durham Mark 6 telescope (Chadwick et al. 1999). In the following years, the same instrument and other VHE telescope failed to detect it again (Chadwick 1999; Nakase 2003). The source was seen again at VHE with the first light of the H.E.S.S. telescopes. Already during its commissioning phase, using only one of its four current telescopes, H.E.S.S. detected the source in 2002 (Aharonian et al. 2005a). Since then, the source has been monitored regularly and can be detected with high significance in each night of observation. PKS 2155-304 was established as one of the brightest VHE sources of the southern hemisphere, with an average flux value of $\sim 20\%$ of the Crab Nebula above 200 GeV.

From October to November 2003, H.E.S.S. took part in a multi-wavelength campaign on this object, yielding the first simultaneous SED measurement including the VHE domain (see figure 1.4). The source was found in a low flux state at X-ray and VHE γ -rays. No strong flux variations could be detected in the VHE domain. At X-ray and optical wavelengths, however, the source showed flux variations of factors greater than two within and between nights. No correlation between emissions at different wavelengths could be found (Aharonian et al. 2005b). In 2004 the source was monitored again in June and July. During this time dust clouds caused by bush fires disturbed the H.E.S.S. observations. Correcting for the dust absorption in the atmosphere is a major task which is still ongoing, therefore no firm quantitative statement can be made yet about the flux levels during this campaign (Nolan 2007). Qualitatively, the source was found in a quiet state, with no significant flaring activity. The observations of PKS 2155-304 between 2005 and 2007 will be presented in this work (chapter 3 and 4).

1.3 Physics overview

In this section the physical processes thought to be responsible for VHE emission in blazars are discussed. The general idea is that electrons or protons³ are accelerated to VHE in relativistic shocks inside AGN jets via first order Fermi acceleration. The principle of this acceleration process will be discussed in section 1.3.2. VHE photons are created when these energetic particles interact either with magnetic fields, diffuse photon fields or ambient matter. The different photon emission processes will be discussed in section 1.3.3. First, some aspects of relativistic dynamics which are relevant in jets will be discussed. In preparation of the limits on Lorentz Invariance violations presented later in this work (chapter 5), the concept of Lorentz Invariance will be briefly recalled in this context.

1.3.1 Relativistic dynamics

Lorentz Invariance

Special Relativity postulates that all laws of physics are Lorentz Invariant, meaning that their form remains unchanged under Lorentz transformations. This can be achieved formally by writing physical equations in a covariant form, meaning that they are written with Lorentz tensors. Lorentz tensors are defined by their behaviour under Lorentz transformation. A Lorentz tensors T of order n transforms as:

$$T^{\sigma'_1 \dots \sigma'_n} = \Lambda^{\sigma'_1}_{\sigma_1} \dots \Lambda^{\sigma'_n}_{\sigma_n} T^{\sigma_1 \dots \sigma_n}, \quad (1.2)$$

³In the following electrons and protons always also refer to positrons and heavier nuclei respectively.

where Λ is the Lorentz transformation matrix. In its simplest form Λ transforms between two coordinate systems S and S' which are moving with constant velocity v along their x -axis with respect to each other, and is then given by:

$$\Lambda_{\nu}^{\mu} = \begin{pmatrix} \gamma & -\gamma\beta & 0 & 0 \\ -\gamma\beta & 1 & 0 & 0 \\ 0 & 0 & 1 & 0 \\ 0 & 0 & 0 & 1 \end{pmatrix}, \quad (1.3)$$

with $\beta = \frac{v}{c}$ and $\gamma = \frac{1}{\sqrt{1-\beta^2}}$.

The Lorentz transformations can be derived from two basic principles: that the speed of light is constant and that the laws of physics are the same in all inertial systems (for a truly axiomatic derivation, the isotropy and homogeneity of space are required as further conditions (Einstein 2002)). The constancy of the speed of light particularly implies that c does not depend on the energy of the photon. Such an energy dependence was predicted by several models in the context of quantum gravity and would lead to Lorentz Invariance violations. The speed-of-light modifications expected within these models are minuscule, and will be sought for later in this work (chapter 5).

Relativistic beaming and Doppler effect

From the Lorentz transformation of the spacetime four-vector ($x^{\mu} = (ct, x, y, z)$), it follows that an object moving with speed u' at an angle θ' with respect to the x -axis in S' will appear to be moving at a smaller angle θ in S :

$$\tan \theta = \frac{u' \sin \theta'}{\gamma (u' \cos \theta' + v)}. \quad (1.4)$$

If we now consider an object radiating isotropically in S' , this leads to a beaming of the emission in the forward direction in the system S . Quantitatively, for a source moving at relativistic speeds ($v \approx c$) and radiating isotropically in S' , half of the emitted photons (all emitted at $\theta' < \frac{\pi}{2}$ in the rest frame) will be emitted within an angle $\theta \approx \gamma^{-1}$ in S . This effect is known as *relativistic beaming* and it strongly enhances the radiation we receive from blazars jets, as they are thought to move relativistically towards Earth.

Apart from beaming the emitted light, the relative motion of the emitter to the observer changes its frequency. If we consider a source radiating at a frequency ω_{source} at rest in a coordinate system S'' , which is moving at speed $-u$ at an angle θ with respect to the x -axis of a system S , the frequency ω_{obs} observed in S is given by:

$$\omega_{\text{obs}} = \frac{\omega_{\text{source}}}{\gamma \left(1 - \frac{u}{c} \cos \theta\right)} = D \omega_{\text{source}}, \quad (1.5)$$

where $D \equiv \frac{1}{\gamma \left(1 - \frac{u}{c} \cos \theta\right)}$ is called the *Doppler factor*. This effect is a combination of the classical Doppler effect and the relativistic time dilatation. Together with relativistic beaming, this leads to a strongly enhanced luminosity from sources which move towards us at relativistic speeds. For an intrinsic luminosity L'_{int} in the rest frame of a source, the apparent luminosity L_{app} at the observer is (Aharonian 2004):

$$L_{\text{app}} \approx D^4 L'_{\text{int}}. \quad (1.6)$$

Causality argument

The validity of the Lorentz transformations implies that no particle can move faster than the speed of light. This fact is often used to constrain the size of emission regions from their variability time scale: as information within in the emitting region can only propagate at the velocity c , the diameter R of a coherently radiating region, variable at a time scale

τ_{source} , must be smaller than $c \times \tau_{\text{source}}$, where τ_{source} and R are measured in the rest frame of the source. In the observer's frame τ_{source} gets Doppler shifted to τ_{obs} , resulting in an upper limit on R of:

$$R < D c \tau_{\text{obs}} (1+z)^{-1}, \quad (1.7)$$

for a source at redshift z . As a word of caution on this argument, it should be noted that its application might be more complicated in some scenarios, since coherent emission might also happen stochastically between multiple regions without causal connection.

1.3.2 Shock acceleration

The emission of VHE and hard X-ray photons from AGN jets shows the presence of highly relativistic, charged particles within them. It is believed that these particles are accelerated to VHE in AGN jets via first-order Fermi acceleration in relativistic shocks. This acceleration process will be discussed in this section under simplified conditions to show its principles. While Fermi acceleration is the most widely accepted model for particle acceleration, several other processes have been proposed, such as shear acceleration (Rieger & Duffy 2004), second order Fermi acceleration (Fermi 1949; Rieger et al. 2007) and photon breeding (Stern & Poutanen 2008). Most likely, all of these processes play a role to some extent. It is not known with certainty today if one process dominates the acceleration process of particles to VHE.

First-order Fermi acceleration

If matter is ejected at supersonic speeds into an ambient medium, the latter is compressed and a shock front emerges. In these shocks particles can be accelerated stochastically to VHE if the medium is magnetized due to a process called first-order Fermi acceleration, which will be described in the following.

If a particle of energy E crosses the shock front from the upstream to the downstream medium, it gets isotropized in the magnetic fields of the downstream medium and can randomly diffuse back into the upstream medium (see figure 1.5). The particle will on average gain energy each time it crosses the shockfront into the downstream medium. This can be understood intuitively, as the kinematics of this process are the same as for a head-on collision of the particle with the (much heavier) downstream medium, the particle therefore gets a “kick”. Quantitatively one can see this by transforming the momentum four-vector ($p^\mu = (E/c, p_x, p_y, p_z)$) of the particle into the rest frame of the downstream medium, averaging over all velocity angles, and transforming back into the rest frame of the upstream medium (see e.g. chapter two in Rosswog & Brüggen (2007)). Expanding the average relative energy gain afterwards to first order in the downstream velocity V for relativistic particles yields:

$$\left\langle \frac{\Delta E}{E} \right\rangle = \frac{4V}{3c}. \quad (1.8)$$

After k round trips a particles of energy E_0 will have an energy $E = E_0 \alpha^k$. If the probability for remaining in the acceleration region per round trip is P , there are $N = N_0 P^k$ particles at this energy after k round trips. Eliminating k with these quantities yields a power law energy distribution of the particles:

$$N = N_0 \left(\frac{E}{E_0} \right)^{\ln P / \ln \alpha}. \quad (1.9)$$

Under the assumption of an adiabatic shock in an ideal gas medium, thermodynamical calculations show that the velocity of the downstream medium is three quarters of the shock velocity u . Therefore Eq. 1.8 yields $\alpha = 1 + u/c$. Particles can leave the acceleration site if they diffuse far enough into the downstream medium to make the probability to diffuse back into the upstream medium negligible (note that particles can not escape into the upstream

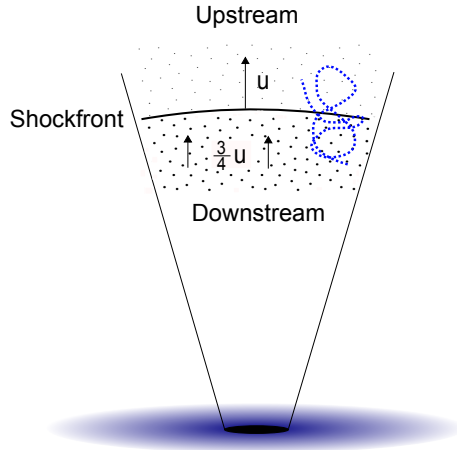


Figure 1.5: Sketch of first-order Fermi acceleration. The dotted line shows the random walk of a particle in random magnetic fields in the downstream and upstream medium.

medium, as the shock front will reach them again at some point during their random walk). The probability of particles leaving the acceleration region in the downstream medium can be estimated to $P = 1 - (u/c)$ (see Bell (1978)). As a result, for $u \ll c$ follows $\ln P / \ln \alpha = -1$, yielding a power law distribution for the particle energy spectrum with a spectral index of minus one, or minus two for the differential energy spectrum dN/dE .

In this discussion, several points were neglected which make the true picture more complicated:

- Shocks in AGN jets are thought to have relativistic velocities (Peacock 1981; Achterberg et al. 2001).
- The influence of the accelerated particles on the shock was neglected (Duffy et al. 1994; Berezhko & Ellison 1999; Lucek & Bell 2000; Malkov et al. 2000).
- The equations of state of interstellar matter differ from ideal gas conditions, resulting in different speeds for the swept up material.
- Electro-magnetic radiation produces energy losses at the acceleration site.

These points lead to modifications of the results derived above. However, the basic conclusion remains unchanged: a non-thermal particle population emerges which has a featureless differential energy spectrum, described approximately by a power law with a spectral index around two. For instance, taking into account radiative losses steepens the spectrum at higher energies, since high energy particles cool faster due to radiation (see next section). This is usually taken into account in blazar emission models by increasing the spectral index of the power law spectrum above some break energy (see section 1.4.1).

1.3.3 Photon interactions

Once charged particles have been accelerated to VHE in blazar jets, they can emit VHE photons via several processes, which will be discussed in the following. The most relevant γ -ray absorption process expected in blazars will also be discussed.

Synchrotron emission

Charged particles moving in magnetic fields emit synchrotron radiation. For a particle of a charge q , a mass m and a momentum p , moving in a magnetic field B , the mean amount of

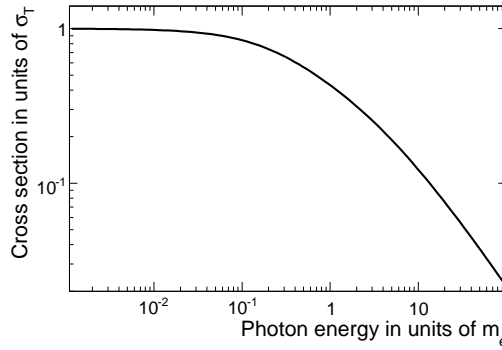


Figure 1.6: Klein-Nishina cross section as a function of photon energy x in units of $m_e c^2$ in the rest frame of the electron.

energy emitted per time due to this process is:

$$\left\langle \frac{dW}{dt} \right\rangle = \frac{16\pi}{9\mu_0 c^5} \frac{q^4 p^2 B^2}{m^4}. \quad (1.10)$$

The emission power in synchrotron radiation scales with the inverse of the fourth power of the mass. Therefore electrons – if present – are expected to dominate the synchrotron radiation over protons. The typical time scale in which a particle loses its energy is given by the cooling time. For a relativistic particle emitting synchrotron radiation it scales with the inverse of its energy:

$$\tau_{\text{cool}}^{\text{synch.}} := \frac{E}{\left\langle \frac{dW}{dt} \right\rangle} = \frac{9\mu_0 c^7}{16\pi} \frac{m^4}{q^4 E B^2}. \quad (1.11)$$

An electron of an energy ~ 1 TeV in a magnetic field of ~ 0.1 G has a cooling time of $\tau_{\text{cool}}^{\text{synch.}} \sim 1000$ s for example (these are typical parameter values expected in regions thought to be responsible for the VHE emission within their own rest frame; see section 1.4.1). The maximum power of the synchrotron radiation is emitted at a peak frequency ν_{peak} of:

$$\nu_{\text{peak}} \approx 0.3 \frac{q E^2 B}{m^3 c^5}. \quad (1.12)$$

For aligned magnetic fields inclined with respect to the observer, synchrotron radiation is polarized, as there is a preferred acceleration direction of the particles with respect to the observer (see chapter three in Rosswog & Brüggen (2007)).

Inverse Compton emission

Charged high energy particles can up-scatter low energy photons to higher energies. This process is called *Inverse Compton emission*. The cross section of this process is the so-called *Klein-Nishina cross section* and is proportional to the inverse of the mass squared of the radiating particle; the process is therefore again suppressed for protons with respect to electrons. In the rest frame of an electron the Klein-Nishina cross section as a function of the photon of energy E in units of the electron rest mass $x = E/m_e c^2$, is given by:

$$\sigma_{\text{KN}} = \frac{3}{8} \sigma_{\text{T}} \frac{1}{x} \left(\left(1 - \frac{2(x+1)}{x^2} \right) \ln(2x+1) + \frac{1}{2} + \frac{4}{x} - \frac{1}{2(2x+1)^2} \right), \quad (1.13)$$

where $\sigma_{\text{T}} = \frac{1}{6\pi\epsilon_0^2} \frac{e^4}{m^2 c^4} \approx 6.5410 \cdot 10^{-25} \text{ cm}^2$ is the Thomson cross section. The Klein-Nishina cross section approaches this value for $x \ll 1$. For $x \gg 1$ the cross section decreases as $\sigma_{\text{KN}} \propto \frac{1}{x}$ (see figure 1.6).

For electrons of energy E up-scattering photons at an energy E_{ph} , the resulting energy spectrum of up-scattered photons is peaked at an energy⁴:

$$E_{\text{peak}} = \frac{4}{3} \frac{E^2 E_{\text{ph}}}{m_e^2 c^4}. \quad (1.14)$$

The average energy loss per time of an electron of momentum p in a photon field of an energy density u_{rad} increases quadratically with the electron energy, if the photons are upscattered with the Thomson cross section:

$$\left\langle \frac{dW}{dt} \right\rangle = \frac{4}{3} \sigma_T c u_{\text{rad}} \frac{p^2}{m_e^2 c^2}, \quad (1.15)$$

resulting in a cooling time for relativistic electrons proportional to the inverse of the electron energy:

$$\tau_{\text{cool}}^{\text{IC-T}} = \frac{3}{4 \sigma_T c u_{\text{rad}}} \frac{m_e^2 c^2}{E}. \quad (1.16)$$

The energy loss per time of electrons with higher energies – upscattering with the reduced Klein-Nishina cross section – rises only logarithmically with increasing electron energy, leading to an approximately linear increase of the cooling time with energy (the complete formulas for this case can be found in chapter three in Aharonian (2004)).

Pion decay emission

Another mechanism capable of producing γ -rays is the decay of neutral pions created in proton collisions with interstellar matter. After a mean life time of 10^{-16} s these pions decay into two γ -rays. The mean energy loss per time due to this process, for a proton with an energy of ~ 1 TeV traversing matter of a density n , is:

$$\left\langle \frac{dW}{dt} \right\rangle \approx \frac{n \sigma_{\text{pp}} c}{6} \approx \frac{n}{4 \times 10^{15}} \text{ TeV s}^{-1}, \quad (1.17)$$

where n is measured in particles per cm^3 .

Pair-production absorption

The most relevant process for γ -ray annihilation in blazars is the γ - γ absorption ($\gamma\gamma \rightarrow e^+e^-$). This process is substantial at the site of the VHE emission, as high intensity photon fields are expected to be present. Additionally, this process is responsible for the absorption of γ -rays on the Extragalactic Background Light during their travel to the Earth, as will be discussed later in section 1.5.

The cross section for pair production for photons of energies E_1 and E_2 at an interaction angle θ is given by Heitler (1960):

$$\sigma_{\gamma\gamma} = \frac{3\sigma_T}{16} (1 - \zeta^2) \left(2\zeta (\zeta^2 - 2) + (3 - \zeta^2) \ln \frac{1 + \zeta}{1 - \zeta} \right), \quad (1.18)$$

with $\zeta = \sqrt{1 - \frac{2m_e^2 c^4}{E_1 E_2 (1 - \cos \theta)}}$. The cross section is strongly peaked; for a isotropic distribution of photons it peaks at energies:

$$E_1 E_2 \approx 4 m_e^2 c^4, \text{ or } \lambda_1(\mu\text{m}) \approx 1.24 E_2(\text{TeV}). \quad (1.19)$$

The peak value of the angle-averaged cross section is $\approx 0.2 \times \sigma_T$. The optical depth at these energies is therefore given by $\tau \approx 0.2 \sigma_T n_{\text{ph}} L$, where L is the traversed distance of a γ -ray in a photon field of a particle density n_{ph} .

⁴In Quantum Field Theory, synchrotron radiation corresponds to Inverse Compton emission of virtual photons in a magnetic field. The formulas therefore show the same energy dependence as the ones discussed previously for synchrotron radiation.

1.4 Blazar emission models

Emission models attempt to explain the SED of blazars and their double humped structure. Additionally, they should explain the dynamical SED variations observed during blazar flares. In these models, particles are assumed to be injected into a radiation region. Inside this region, which is moving with high relativistic speed towards the observer, the particles emit photons by the processes discussed in the previous sections. One distinguishes between leptonic and hadronic models, depending on the particles responsible for the emission. Most likely all the processes discussed in the following take place in blazars at some level. The question not answered with certainty to date is if one of the following emission mechanisms dominates the blazar energy output.

1.4.1 Leptonic models

In leptonic models the particles injected into the radiation region are electrons. The low energy bump in the SED is produced by synchrotron emission in magnetic fields inside this region. This is consistent with the fact that blazar emission is usually polarized at these frequencies. The high energy bump in the SED is emitted via Inverse Compton emission from the same particles. The seed photons for this process can be the synchrotron radiation of the same particle population (*Synchrotron Self Compton*, SSC) or come from external photon fields (*External or Ambient Compton*). In both models the electro-magnetic emission responsible for the SED comes from the same particles, as is strongly suggested by the correlated variability patterns between X-rays and γ -rays during flares (see section 1.2).

Synchrotron Self Compton

In SSC models, relativistic electrons and positrons are injected into a spherical blob of radius R and a uniform magnetic field B , moving with respect to the observer with the Lorentz factor Γ , as shown in figure 1.7 (other shapes of the emitting region – e.g. cylindrical –, and non-homogeneous magnetic fields have also been used). The energy spectrum of the injected leptons is usually described by a broken power law:

$$\begin{aligned}\Phi(E) &= \Phi_0 E^{-\Gamma_1} & \text{for } E < E_{\text{break}}, \\ \Phi(E) &= \Phi_0 E_{\text{break}}^{\Gamma_2 - \Gamma_1} E^{-\Gamma_2} & \text{for } E > E_{\text{break}},\end{aligned}\tag{1.20}$$

where Γ_1 is usually around two, following the result from section 1.3.2, and Γ_2 is typically around three. This steepening of the spectrum towards higher energies is used to take into account radiative cooling at the source, which is faster for particles of higher energies (see equations 1.11 and 1.16). The radiative output coming from this region can be calculated with the formulas given in the previous section. There are several implementations of this model for which binary files are publicly available (see Krawczynski (2008), Tramacere (2008), or Georganopoulos et al. (2008)). In these implementations, the photon-photon absorption of VHE photons by synchrotron photons is taken into account. This absorption can be substantial and may even result in the fact that γ -rays cannot leave the radiation region for certain combinations of the parameters Γ , R , B and the electron density. The $\gamma\gamma$ -absorption becomes significantly reduced with increasing Lorentz factor of the radiating region. The reason is that for an increasing Lorentz factor the observed synchrotron luminosity corresponds to an increasingly lower photon density in the rest frame of the source due to the Doppler boosting (see section 1.3.1).

In the past, SSC models have been very successful in modeling the SED of blazars (see e.g. Maraschi et al. (1992); Ghisellini et al. (1998)). However, it should be noted that even though these models make several simplifying assumptions, the number of free parameters is often still of the same order than the number of data points, as a wide simultaneous multi-wavelength coverage of blazars is still rare. Also, additional radiation components often need to be added to explain part of the optical or radio emission (see figure 1.4 or

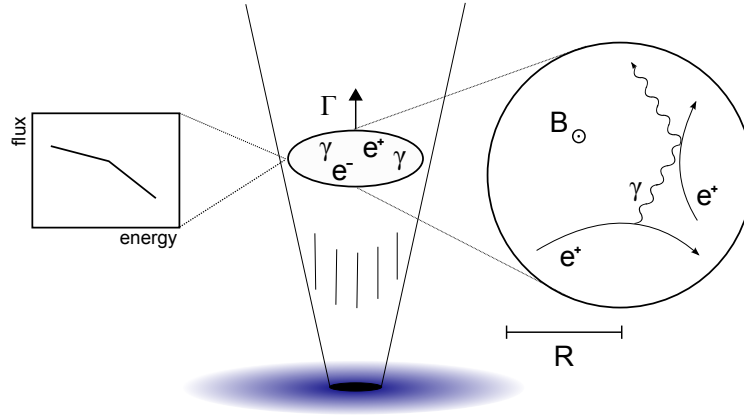


Figure 1.7: Sketch of a Synchrotron Self Compton model. The emission region is moving with a Lorentz factor Γ within an AGN jet. The zoom into the emission region shown on the right illustrates the synchrotron and Inverse Compton emission of the electrons inside of the emission region. Also shown are the magnetic field B and radius R of the emitting region in its rest frame. The panel on the left side of the figure illustrates the electron energy spectrum within the emission region.

Aharonian et al. (2008a)). The best fit values from SSC models typically reveal magnetic fields of the order of 0.1 G and Doppler factors of the order of ten.

In preparation of the multi-wavelength observations taken during the Chandra Flare that will be presented in chapter 4, it is interesting to analyze the expected correlation between the two SED component expected in SSC models, particularly between the X-ray and γ -ray band. Within SSC models, electrons can upscatter their own synchrotron photons either with the Thomson cross section or the reduces Klein-Nishina cross section, depending on the parameters B , Γ and the energy range in question (see equations 1.12 and 1.13). A blazar is said to be in the *Thomson regime* or *Klein-Nishina regime* in a certain photon energy band, depending on which of these two cases is valid for the electrons responsible for the photon emission. The correlation of the SED components is expected to be different in both regimes; while the exact dependency of the γ -ray flux (F_γ) from the X-ray flux (F_x) is very complex, qualitatively one expects a quadratic dependency ($F_\gamma \propto F_x^2$) if the source is in the Thomson regime (see chapter 10 in Aharonian (2004)), and a less than quadratic dependency in the Klein-Nishina regime, as will be explained in the following.

To first order the variations seen during flares are expected to result from varying electron densities n_e . These variations are caused by electron injection during the rise of flares and by electron cooling at their falling edges. The flux F_{sync} observed in a certain energy range of the synchrotron component is proportional to the density of the radiating electrons around an energy E_1 :

$$F_{\text{sync}} \propto n_e(E_1). \quad (1.21)$$

The flux F_{IC} observed in a certain energy range of the Inverse Compton component is proportional to the density of electrons around an energy E_2 . Additionally F_{IC} is proportional to the density of the up-scattered photon field n_{ph} (equation 1.15). If the source is radiating in the Thomson regime, the density n_{ph} is again proportional to $n_e(E_2)$, resulting in:

$$F_{\text{IC}} \propto n_{\text{ph}}(E_2) \times n_e(E_2) \propto n_e(E_2)^2 \quad (1.22)$$

X-ray and γ -ray observations of HBL typically cover the high energy part of the synchrotron and Inverse Compton peak of the SED; one therefore expects the high energy part of the electron population to be responsible for both emissions ($E_1 \approx E_2$). Inserting equation 1.21 in equation 1.22 therefore yields $F_\gamma \propto F_x^2$ in the Thomson regime. The correlation

is more complex if the source is in the Klein-Nishina regime, since electrons of a certain energy typically upscatter synchrotron photons emitted by electrons of lower energies in this regime (as these photons have lower frequencies and are therefore upscattered with a larger cross section, see equations 1.12 and 1.13). During the decaying part of flares, the density of lower energy electrons can be considered constant in time (as high energy electrons cool faster); in this approximation one obtains $F_\gamma \propto n_e(E_2)$, resulting in $F_\gamma \propto F_x$.

The correlations between γ -ray and X-ray flux discussed so far relied on several simplifying assumptions. Generally in SSC models:

- The emission observed in a given photon band is emitted by electrons of multiple energies.
- The emission observed by X-ray and γ -ray experiments is emitted by electrons around different energies ($E_1 \neq E_2$).
- Flux variations are not only related to changes in the electron density, but also to a varying size, magnetic field and Doppler factor of the emitting region.

Katarzyński et al. (2005) performed a detail study of the possible correlations within SSC models, taking these aspects into account. Their result is that the correlation is always less than quadratic for the phase space considered reasonable for HBL. Obtaining a more than quadratic dependency of F_γ from F_x requires an unrealistic fine-tuning of the parameters and their variations in time, particularly if both observed energy ranges are above their respective SED peaks and during the decaying phase of flares (Katarzyński et al. 2005; Tavecchio et al. 2001).

External and Ambient Compton

In contrast to SSC models, the seed photons which are scattered via Inverse Compton can also come from regions outside of the emission region. They can be produced outside of the jet (*External Compton*), for example by the disk (Dermer & Schlickeiser 1993), by the Broad Line Region – illuminated either by the disk (Sikora et al. 1994) or by the jet itself (Ghisellini & Madau 1996) – or by the dusty torus (Sikora 1994; Wagner & Witzel 1995; Sikora et al. 2002). The target photons can also be provided by different parts of the jet itself (*Ambient Compton*), as recently proposed for example by Georgantopoulos & Kazanas (2003) or Ghisellini et al. (2005).

1.4.2 Hadronic models

In hadronic models, the high energy component of the SED is explained with γ -ray emission induced by VHE protons. These protons can produce secondary γ -rays when interacting with matter inside the jet (Pohl & Schlickeiser 2000). However, the low density of the plasma in blazar jets results in a long cooling time of relativistic protons, failing to explain the fast variability observed during flares (Aharonian et al. 1999a). Alternatively, ultra high energy protons ($E \sim 10^{19}$ eV) can produce γ -rays directly – via synchrotron emission in a highly magnetized blob ($B \sim 30$ -100 G; Proton Synchrotron model, Aharonian (2000)) – ,or indirectly, through secondary electrons produced in a cascade induced by proton interactions with external photons ($p - \gamma$ model, Mannheim (1993)), or both (Mücke & Protheroe 2001). However, it has been shown that in blazars the cooling times or the photo-meson process are much longer than for the synchrotron process or than the observed variability times, leaving the proton-synchrotron mechanism as the most effective channel (Aharonian 2000).

As in leptonic models, in hadronic models the low energy component of the SED is produced via synchrotron emission of VHE electrons. These electrons are either accelerated together with the protons responsible for the high energy SED component, or created as secondary products in reactions of VHE protons with photon fields or matter. Hadronic models can therefore also account for the correlations between the high and low energy

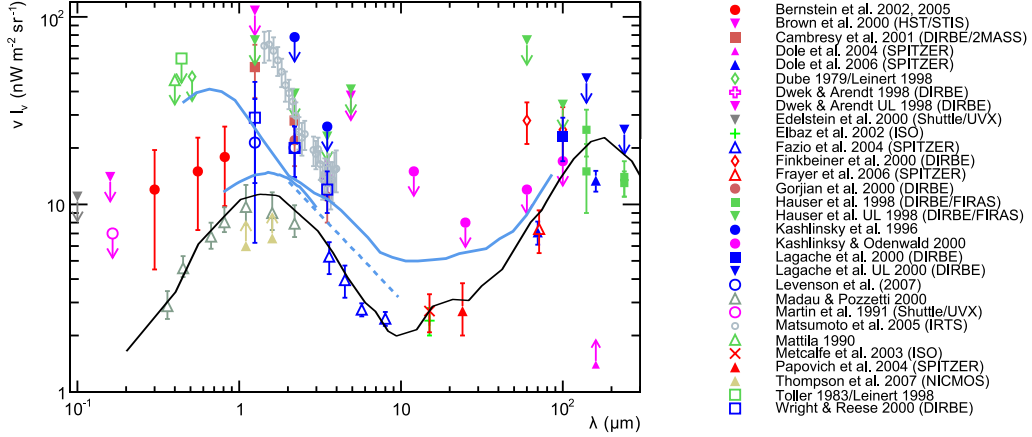


Figure 1.8: Spectral Energy Distribution of the Extragalactic Background Light in the wavelength range of 0.1 to 200 μm for a redshift of zero. Markers with arrows indicate lower or upper limits on the EBL. Open triangles show measurements where the light from all resolved extragalactic sources was integrated. The blue lines refer to upper limits on the EBL obtained from spectral measurements of blazars at VHE (Aharonian et al. 2006b; Mazin & Raue 2007; Aharonian et al. 2007a). The black line shows the EBL model of Franceschini et al. (2008) used in this work. The data compilation of EBL measurements was provided by Martin Raue.

component seen during flares. However, generally hadronic models require more extreme and fine-tuned parameters than leptonic models, given that the synchrotron (and Inverse Compton) mechanism is more efficient in the case of electrons. Additionally, the faster acceleration and cooling times due to the low electron mass can more easily account for the fast variabilities observed during flares. For these reasons, leptonic models are preferred to explain the VHE emission from blazars.

1.5 The Extragalactic Background Light

One important point for the interpretation of VHE measurements from extragalactic sources has been neglected so far in this chapter: the photon-photon absorption of VHE γ -rays by the Extragalactic Background Light (EBL) in the optical to infrared waveband. For extragalactic sources this attenuation is severe and needs to be taken into account in the modeling of blazars. If a source at a redshift z emits a photon number flux $F_0(E)$ at a given energy E , an attenuated flux:

$$F(E) = F_0(E) e^{-\tau(E,z)} \quad (1.23)$$

will reach Earth. The optical depth τ is determined by integrating the particle density of the EBL $n(\epsilon)$ along the line of sight for all interaction angles $\mu = \cos \theta$ and energies ϵ . Neglecting cosmological evolution effects of the EBL, which become important only for $z > 0.5$, this results in:

$$\tau(E, z) = \frac{cz}{H_0} \int_{-1}^1 d\mu \frac{1-\mu}{2} \int_0^\infty d\epsilon n(\epsilon) \sigma_{\gamma\gamma}(\epsilon, E, \mu), \quad (1.24)$$

where H_0 is the Hubble constant and $\sigma_{\gamma\gamma}$ is the pair-production cross section from equation 1.18.

The energy dependence of the optical depth – which is determined by the spectrum of the EBL – causes a steepening of the emitted γ -ray spectrum, more or less severe according

to the energy band affected (Aharonian 2001). In order to obtain source-intrinsic VHE spectra, the measured spectra need to be deabsorbed. This complicates the interpretation of deabsorbed spectra due to the uncertainties in the EBL level. However, flux variability studies, and also correlations between the VHE emission and other wavelength, are not affected.

To date the SED of the EBL is not well known in the optical to infrared wavelength bands. Figure 1.8 shows a composition of current measurements and limits, showing a double peaked structure. The peak in the optical ($\lambda \sim 1\mu\text{m}$) is attributed to starlight from galaxies. The second peak in the infrared ($\lambda \sim 100\mu\text{m}$) is attributed to re-emission of the optical photons by dust clouds. Currently, measurements of the EBL still have large discrepancies of more than a factor of two in the relevant wavebands for VHE γ -ray absorption. This is due to large systematic uncertainties of the measurements related to the subtraction of foreground emission of zodiacal light (emitted within our solar system). Due to this large experimental uncertainty VHE spectra are deabsorbed with EBL models. In this work the recent model from Franceschini et al. (2008) was used. This model predicts an EBL level close to the level expected from integrating the light from all resolved extragalactic sources (see figure 1.8). It therefore represents a lower limit on the EBL density, and will be referred to as the *minimal EBL model* throughout this work. The γ -ray attenuation as a function of energy predicted by this model for a source at the distance of PKS 2155-304 ($z = 0.116$) can be seen in figure 1.9.

Measurements of distant blazars by the H.E.S.S. collaboration show that the EBL level must be very close to the minimal EBL model (Aharonian et al. 2006b; Mazin & Raue 2007; Aharonian et al. 2007a); however, it might still be higher by $\sim 30\%$ (see figure 1.8). Therefore, fluxes deabsorbed with the minimal EBL model represent lower limits on the intrinsic source fluxes. In order to obtain an upper limit, fluxes will also be deabsorbed with a *maximal EBL model*. This model corresponds to the upper bound on the EBL level compatible with the mentioned H.E.S.S. upper limits and is obtained by scaling the SED of the minimal EBL model by a factor of 1.3.

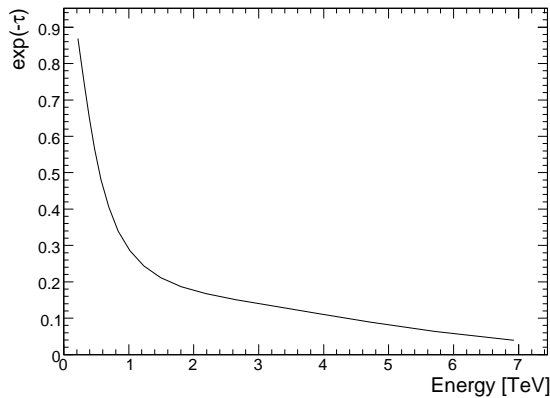


Figure 1.9: Attenuation of γ -rays as a function of energy for a source at a distance of $z = 0.116$. The attenuation was calculated with the EBL model of Franceschini et al. (2008).

Chapter 2

H.E.S.S. and its data analysis

The techniques applied by H.E.S.S. to detect γ -rays at VHE energies are presented in this chapter. H.E.S.S. is an array of Imaging Atmospheric Cherenkov Telescopes (IACT). The principles of this technique and the specific hardware implementation for H.E.S.S. are discussed in section 2.1. The different steps of the software analysis used to derive lightcurves and energy spectra are discussed in section 2.2.

2.1 The imaging atmospheric Cherenkov technique

The imaging atmospheric Cherenkov technique was pioneered by the Whipple Observatory in Arizona. In 1989, it detected the first VHE γ -ray source, the Crab Nebula (Weekes et al. 1989). The technique relies on the indirect detection of γ -rays using the particle showers they induce in the atmosphere. In the following section, this technique is briefly described. Afterwards, in section 2.1.2, the specific properties of the H.E.S.S. telescopes are presented.

2.1.1 Imaging Atmospheric Cherenkov Telescopes

A VHE photon entering the atmosphere interacts in the electric field surrounding a nucleus in the air, producing a $e^+ e^-$ pair. This process typically takes place after traversing a mean atmospheric depth of $7/9 X_0$, where $X_0 = 37.2 \text{ g cm}^{-2}$ is the radiation length in air. The total thickness of the Earth's atmosphere is $\sim 1000 \text{ g cm}^{-2}$, therefore no γ -rays reach the ground. After having produced the electron-positron pair, these secondary particles emit γ -rays via Bremsstrahlung, typically after one radiation length. This results in a particle cascade (see figure 2.1). The cascade dies out once the ionization losses of the produced electrons and positrons are greater than the ones due to Bremsstrahlung. The shower maximum – defined as the height at which the shower contains the maximum number of electrons – is typically reached at a depth of $\sim 300 \text{ g cm}^{-2}$, which corresponds to a height of $\sim 10 \text{ km}$. The width of the shower at this height is $\sim 100 \text{ m}$, mainly due to the Coulomb deflections of the electrons and positrons on atomic nuclei.

The particles in the electro-magnetic shower emit Cherenkov light if they have energies greater than $m_e c^2 / \sqrt{1 - n^{-2}}$, where n is the refractive index. The opening angle of the Cherenkov emission is typically 1° , hence, for a typical observation height of $\sim 2000 \text{ m}$ above sea level, the Cherenkov photons will be emitted into a *light pool* of $\sim 100 \text{ m}$ radius. The photon density on the ground scales approximately linearly with the energy of the primary γ -ray and is around 100 photons per square meter for an energy of 1 TeV. The Cherenkov photons arrive at the ground within a very narrow time window of a few tens of ns (see figure 2.1).

IACTs image the Cherenkov light from air showers from the ground. From these images the properties of the primary γ -ray are inferred, in particular its direction and energy (more details on this will be given in section 2.2.1). The main advantage of IACTs is that within

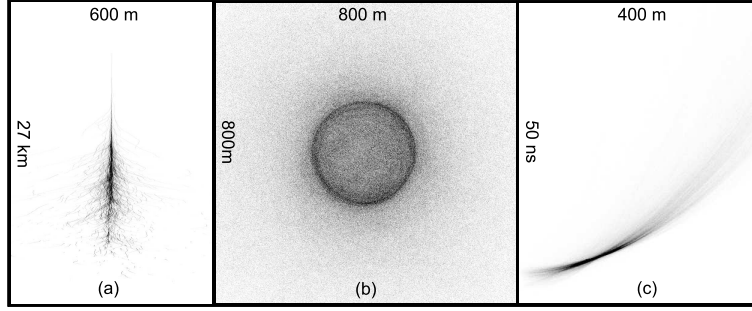


Figure 2.1: Simulation of a 300 GeV γ -ray entering the atmosphere from zenith. Panel (a) shows the tracks of the secondary particles created in the shower projected on a plain parallel to the shower axis. The height is given above see level. Panel (b) shows the distribution of Cherenkov photons on the ground. Panel (c) shows the relative arrival time of these photons on the ground as a function of the distance from the core. The arrival times are given with respect to the extrapolated arrival time of the primary γ -ray. The figures were provided by Konrad Bernlöhner.

Table 2.1: Properties of the four major IACTs arrays currently in operation (2008). Shown are the position of the telescopes in latitude and longitude, the diameter of their field of view, the lower energy threshold E_{thr} and the sensitivity. The table is reproduced from Hinton (2008).

Instrument	Lat. [°]	Long.[°]	FoV [°]	E_{thr} [TeV]	Sensitivity (% Crab)
H.E.S.S.	-23	16	5	0.1	0.7
VERITAS	32	-111	3.5	0.1	1
MAGIC	29	18	3.5	0.06	2
CANGAROO-III	-31	137	4	0.4	15

a typical field-of-view of $\sim 4^\circ$ diameter an effective collection area of $\sim 10^5 \text{ m}^2$ is covered, a vast improvement over γ -ray satellites used at lower energies. One caveat is that the very small Cherenkov photon densities imply the need for a very low night sky background level. This can only be achieved in moonless nights, reducing the duty cycle of IACTs to $\sim 10\%$. Exceptions are possible at the expense of a higher energy threshold (see Rico et al. (2007)).

The major challenge of the IACT technique is the presence of the very large background of showers induced by cosmic rays. Even for strong γ -ray sources, this background is at least a factor 1000 stronger than the signal from the source. Fortunately, a large fraction of the background can be rejected by applying selection criteria to the shape of the shower images. This is possible since cosmic-ray induced showers are generally wider than γ -ray induced showers for the following reason: cosmic rays consist mainly of protons and helium; when these particles interact with the atomic nuclei in the atmosphere they create hadrons (mainly pions and fragments of nuclei). As these particles interact via the strong force, they obtain higher transverse momenta than the particles in electro-magnetic showers, which make hadron-induced showers wider. After applying these so-called *shape cuts*, described in more detail in section 2.2.2, there still remains a significant background. This background is removed on a statistical basis by modeling it from regions in the sky with no γ -ray signal.

To date, four major IACT arrays are imaging the γ -ray sky. Two of them, MAGIC (Cortina 2005b) and VERITAS (Maier 2007), are located in the northern hemisphere, while the H.E.S.S. and CANGAROO (Kubo et al. 2004) arrays are located in the southern hemi-



Figure 2.2: The H.E.S.S. telescopes.

sphere. The main properties of these four instruments are summarized in table 2.1. Their sensitivities ranges between $\sim 1\text{-}15\%$ Crab. This sensitivity refers to the minimum flux as a percentage of the Crab Nebula flux above 1 TeV ($\approx 2 \times 10^{-11}$ photons $\text{cm}^{-2} \text{s}^{-1}$) the system can detect with a significance of 5σ in 50 hours of observation. The H.E.S.S. telescope system will be introduced in more detail in the following section.

2.1.2 The H.E.S.S. telescopes

H.E.S.S. is an array of four IACTs located in the Khomas highlands of Namibia at an altitude of 1800 m. The telescopes are positioned on the corners of a square with 120 m length. H.E.S.S. is a stereoscopic system, meaning that showers are simultaneously imaged from multiple directions, allowing a better reconstruction of the geometry of the shower (see section 2.2.1). The spacing is therefore a compromise between the need to have multiple telescopes within the light pool of a γ -ray shower and covering a large stereo angle.

The telescope mirrors are mounted in a Davis-Cotton design (Davies & Cotton 1957); they collect the Cherenkov light from air-showers on a total surface of 107 m^2 and image it onto a camera located at a focal length of 15 m. The camera consists of an hexagonal array of 960 pixels, each composed of a single photomultiplier. The shower images are sampled with a resolution of 0.16° , given by the angular spread of each pixel. For more details on the telescope layout, see Bernlöhner et al. (2003).

The telescopes have a three-level trigger (Funk et al. 2005). Each pixel is first required to have recorded a signal equivalent to at least 4 photo-electrons (p.e.) within an interval of 1.5 ns. In order for the camera to be read out, a second trigger requires at least 3 pixels within one sector - a square of 64 pixels - to have triggered. If these criteria are met, the camera sends a signal to a central trigger, which requires at least two telescopes to have triggered within 80 ns. This final stereoscopic trigger condition significantly reduces the deadtime of the system, by rejecting a large fraction of the background (primarily due to single muons created in cosmic-ray induced showers). The typical deadtime of the system is $\sim 5\%$, varying with the zenith angle of the observations.

In an offline analysis, the camera images are calibrated to take into account different photon efficiencies for different pixels following the prescriptions in Aharonian et al. (2004a). Pixels which contain mainly night sky background are removed from the image. This is done with a two-level filter, which requires one pixel to have an minimum intensity of 5 p.e. and a neighboring pixel with at least 10 p.e., or vice versa. The resulting “cleaned” set of pixels containing Cherenkov light is hereafter referred to as the *shower image*.

2.2 Data analysis

H.E.S.S. data are taken in time intervals of 28 minutes, referred to as *runs*. Each run contains about ~ 300000 recorded events. These events are reconstructed following the pre-

descriptions explained in section 2.2.1. In section 2.2.2, the techniques to remove the hadronic background from the recorded signal are explained. Sections 2.2.3 and 2.2.4 discuss the techniques used to derive spectra and lightcurves from these signals. The systematic errors of these measurements are discussed in 2.2.5. This section closes with a discussion of tests of the quality of the taken data in section 2.2.6 and a brief discussion of the practical implementation of the analysis in section 2.2.7.

2.2.1 Event reconstruction

The properties of the primary γ -ray, such as its energy, direction and extrapolated impact position on the ground (the *core position*), can be derived by using the shower images of each camera. Here, one method of reconstructing these properties is described.

Direction and core reconstruction

The core position can be inferred from the relative alignment of the shower images with respect to each other. This is possible since images of a shower with a non-zero core distance – defined as the distance from the telescope to the core position – are elongated and their major axis points back to the core position (see figure 2.3). To quantify this, the shower images are parameterized by *Hillas parameters*, illustrated in figure 2.4. These are based on the first and second moments of the intensity distribution in the camera. The matrix of the second moments can be visualized as an ellipse of a given width and length, with the major axis pointing back to the core position. The core position is obtained by averaging the intersecting points of the major axes from multiple shower images. In this average, several weighting factors are used to take into account the different quality of the shower images (for more details see Berge (2006)). The direction of the primary particle can be reconstructed in a similar way, by intersecting the major axes of the shower images in the combined focal plane of the different telescopes (see figure 2.3). The accuracy achieved with this method depends on multiple factors, e.g. the energy of the primary particle and the number of telescopes that imaged the shower (Berge 2006). The typical accuracy of the reconstruction is $\sim 0.1^\circ$ for the shower direction and ~ 20 m for the core position.

Energy reconstruction

The energy of the primary γ -ray is estimated from the total shower image intensity and the core distance from each telescope, using a lookup table generated from detailed shower and instrument simulations. This is possible because the total Cherenkov photon number on the ground is approximately proportional to the energy of the primary γ -ray. The core distance estimate is needed since the photon intensity on the ground of a shower varies with the distance from its core (see figure 2.1). The simulations are made with the shower simulation program CORSIKA 6 (Heck et al. 1998) and the telescope simulation program `sim_hess_array`. The uncertainties in this simulation lead to a systematic uncertainty in the energy estimate, which will be discussed in section 2.2.5.

Besides the image intensity and the core distance, the lookup parameters include the zenith angle of the observations and the angular distance between the shower direction and the camera center in the focal plane (*Offset*), since these quantities also affect the total image intensity in the camera for a given energy. The energy is reconstructed using these lookup tables for each telescope image individually and averaged afterwards for each event. The single telescope energy estimate is corrected for the loss of optical efficiency over time of the telescope with respect to the simulations. This relative efficiency loss is determined from imprints of single muons in the shower images from hadrons during normal observations. These muons produce distinctive rings in the shower images, which were emitted with a fixed photon intensity per arc length, allowing to estimate the total optical efficiency of each telescope (Bolz 2004).

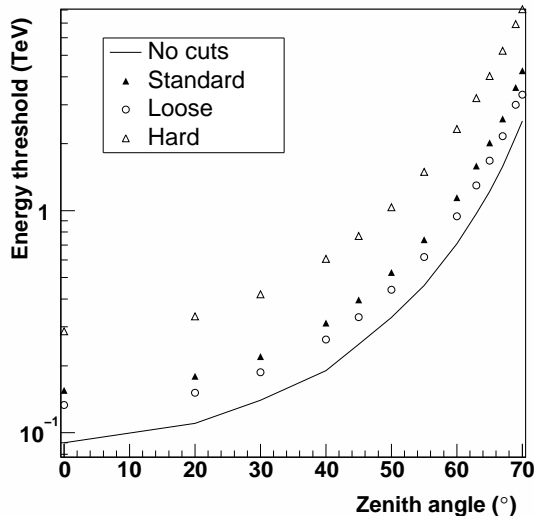


Figure 2.5: Safe threshold as a function of the zenith angle of the observation for several γ -ray selection cuts specified in section 2.2.2 (taken from Aharonian et al. (2006a)).

The accuracy of the energy reconstruction is typically $\sim 15\%$ (the exact value again depends on multiple observation parameters, see Berge (2006)). At lower energies, the energy reconstruction systematically overestimates the energies of the events due to a selection effect: close to the lower energy threshold of the instrument, showers with higher intensities than average fulfill the γ -ray selection cuts discussed in section 2.2.2. In order to minimize the effect of this bias on lightcurve and spectrum measurements, a safe threshold is defined (Aharonian et al. 2006a). For energies above this threshold the energy bias is under 10%. The safe threshold depends on the zenith angle of the observations, as shown in figure 2.5.

2.2.2 Background rejection

In order to obtain a γ -ray signal, one has to remove the background from cosmic-ray induced showers. This is achieved by selecting γ -ray events based on the properties of their shower images and afterwards removing the remaining background statistically with the help of sky regions containing no γ -ray signal.

γ -rays selection cuts

As mentioned in section 2.1.1, γ -ray showers are on average narrower than cosmic-ray induced showers. This fact is reflected in γ -ray shower images having a smaller width of the Hillas ellipse. In order to quantify this, shower images are compared to the width of the shower expected from γ -ray simulations. To facilitate selection, a single parameter describing the average shower width from the telescope images is generated - the *Mean Reduced Scaled Width* (MRSW):

$$MRSW = \frac{1}{N_{\text{tels}}} \sum_{\text{tels}} \frac{width_i - \langle width \rangle_i}{\sigma_i},$$

where N_{tels} is the number of shower images and $\langle width \rangle_i$ and σ_i are the width and the standard deviation expected from γ -ray simulations. The MRSW therefore represents the mean deviation from the width of the shower images with respect to the one expected from simulations in units of σ . The expected values of $\langle width \rangle_i$ and σ_i are read out from lookup

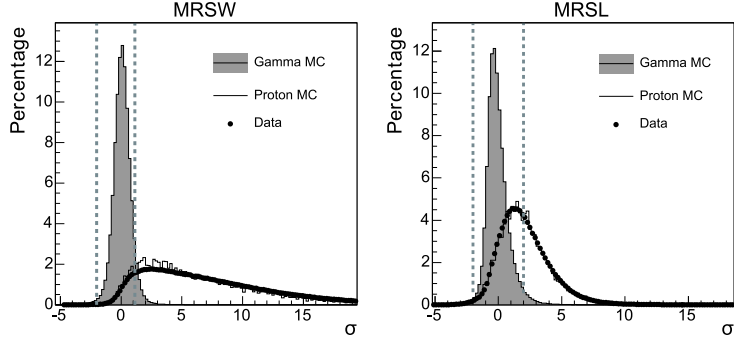


Figure 2.6: Distributions of MRSW (left) and MRSL (right) for simulated γ -rays and protons and for off-source data. The dotted lines shows the γ -ray selection limits for *loose cuts* specified in table 2.2 (adapted from Funk (2005)).

table for each shower image, as a function of the total image intensity, the core distance and the offset. In analogy to the MRSW one defines the *Mean Reduced Scaled Length* (MRSL) to compare the length of the shower image to the expected one for γ -rays:

$$MRSL = \frac{1}{N_{\text{tels}}} \sum_{\text{tels}} \frac{\text{length}_i - \langle \text{length} \rangle_i}{\sigma_i}.$$

The MRSW and MRSL distribution of γ -rays are approximately Gaussian with a mean value of zero¹; cosmic rays, however, have a wider distribution centered at higher values (see figure 2.6), allowing to set cuts on these parameters to select γ -rays. The exact cut value which optimizes the statistical significance of the γ -ray signal depends on the energy spectrum of the source. Therefore several sets of cuts have been defined a priori, maximizing the significance for different source types (Aharonian et al. 2006a). The cut values are summarized in table 2.2. In the analysis presented in this work *loose cuts* will be used, which were optimized for a source with a flux level similar to the Crab Nebula and an energy spectrum described by a power law with a spectral index of 3.0. These cuts yield the lowest energy threshold due to the low required minimal image intensity (see figure 2.5). This is optimal for sources with a soft energy spectrum, as typically found for AGN at VHE. On the other hand, because the shower reconstruction is worse for low intensity images, the average reconstruction accuracy for *loose cuts* is $\sim 0.13^\circ$ for the direction, ~ 25 m for the core position and $\sim 20\%$ for the energy, slightly worse than the typical values mentioned in section 2.2.1.

It should be mentioned that several other types of cut parameters have been introduced to select γ -ray induced showers from hadronic ones (see e.g. Piron et al. (2001); de Naurois (2006); Lemoine-Goumard et al. (2006)). While these more sophisticated methods will likely play a bigger role in the future, the scaled parameter cuts presented here are the standard in VHE astronomy to date because of their robustness and fast application.

Background modeling

After having reduced the hadronic background with the γ -ray selection cuts – typically by a factor >100 from the direction of the source – there still remains a background of hadronic showers in the recorded signal. This background is still substantial, typically of the same order as the γ -ray signal, depending on selection cuts and source strength. In order to measure the γ -ray excess in the on-region – defined by a circular region around

¹The width of the Gaussian varies with the number of telescope images N_{tel} , with higher multiplicity events having a narrower distribution. This is desired to implicitly prefer higher multiplicity events with the γ -ray selection cuts.

Table 2.2: Shown are different sets of γ -ray selection cuts used by H.E.S.S.. The cuts are applied on MRSW and MRSL, on the total image intensity and on the squared angular distance from the source position to the reconstructed direction θ^2 (see figure 2.4). All cuts also require at least two shower images per event. The images are required to have a maximal distance from the center of gravity of the images to the camera center smaller than 2° , to avoid images being truncated at the camera edges.

Configuration	MRSW Min.	MRSW Max.	MRSL Min.	MRSL Max.	θ^2 Max. [degree ²]	Image int. Min. [p.e.]
Standard	-2.0	2.0	-2.0	0.9	0.0125	80
Hard	-2.0	2.0	-2.0	0.7	0.01	200
Loose	-2.0	2.0	-2.0	1.2	0.04	40

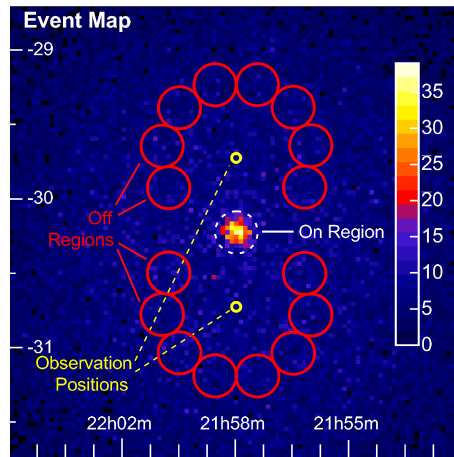


Figure 2.7: Illustration of the reflected-region background model for two runs with opposite wobbles in Declination. The color scale shows the γ -ray excess in each bin from PKS 2155-304 in 2005 (Aharonian et al. 2005b) (from Berge et al. (2007)).

the source position with a radius θ – the remaining background is subtracted statistically. There are several methods to do this, for a discussion see e.g. Berge et al. (2007). In this work the *reflected-region model* is used, as it avoids systematic uncertainties due to detector acceptance modeling, required by other methods (Berge et al. 2007).

In the reflected-region model, the background level in the on-region is estimated for each run from off-regions with the same size and offset with respect to the camera center. As the detector acceptance of H.E.S.S. is radially symmetric in the camera, this assures the same acceptance for the on- and off-regions. In order to apply this method, H.E.S.S. observations are usually taken in *wobble mode*, where the source is observed at a typical offset of 0.5° with respect to the camera center (see figure 2.7). The wobble positions are alternated between runs in RA and Dec coordinates. The total γ -ray excess in one run $N_{\text{excess}}^{\text{run}}$ with $N_{\text{on}}^{\text{run}}$ events in the on region and $N_{\text{off}}^{\text{run}}$ events in n_{off} off-regions is given by:

$$N_{\text{excess}}^{\text{run}} = N_{\text{on}}^{\text{run}} - \frac{N_{\text{off}}^{\text{run}}}{n_{\text{off}}}. \quad (2.1)$$

The total γ -ray excess is given by the sum of the excess of all runs, which can be written as:

$$N_{\text{excess}} = \sum_{\text{run}} N_{\text{on}}^{\text{run}} - \alpha \sum_{\text{run}} N_{\text{off}}^{\text{run}}, \text{ with } \alpha = \frac{1}{N_{\text{off}}^{\text{total}}} \sum_{\text{run}} \frac{N_{\text{off}}^{\text{run}}}{n_{\text{off}}^{\text{run}}}. \quad (2.2)$$

Signal excess error and significance

The statistical significance S of the γ -ray excess signal N_{excess} is estimated following the prescription of Li & Ma (1983):

$$S = \sqrt{2} \left(N_{\text{on}} \ln \left(\frac{(1 + \alpha) N_{\text{on}}}{\alpha (N_{\text{on}} + N_{\text{off}})} \right) + N_{\text{off}} \ln \left(\frac{(1 + \alpha) N_{\text{off}}}{N_{\text{on}} + N_{\text{off}}} \right) \right)^{\frac{1}{2}}. \quad (2.3)$$

The upper and lower bound of a 68% confidence interval of a γ -ray excess is derived from N_{on} , N_{off} and α following the method of Feldman & Cousins (1998). This method is applied in the limit of Gaussian probability errors for the on- and off-event counts. This assumption is no longer a good approximation if the on or off counts fall below ten. In this case the method from Rolke et al. (2005) is used.

2.2.3 Spectrum measurement

In order to measure the energy spectrum of a given γ -ray excess, the total collection area on the ground of the detector as a function of energy needs to be known. The effective collection area A_{eff} is defined as the equivalent physical area a perfect detector with an efficiency of one would have on the ground. It is derived from a simulated γ -ray spectrum described by a power law with a spectral index Γ . For a given offset O and zenith angle θ the effective collection area is derived as²:

$$A_{\text{eff}}(O, \theta, E, \Gamma) = \frac{N_{\text{detected}}(E, \Gamma)}{N_{\text{sim}}(E_{\text{MC}}, \Gamma) A_{\text{sim}}}, \quad (2.4)$$

where N_{sim} is the total number of simulated γ -rays with a reconstructed energy E , N_{detected} is the number of γ -rays after selection cuts for a given Monte Carlo energy E_{MC} and A_{sim} is the physical area over which the γ -rays were simulated.

The differential energy flux in an energy interval ΔE at an energy E can be calculated as the sum of the on- and off-events weighted by the inverse of the effective area corresponding to each event:

$$\Phi(E) = \frac{1}{t_{\text{live}} \Delta E} \left(\sum_{\text{on}} \frac{1}{A_{\text{eff}}} - \sum_{\text{off}} \frac{1}{n_{\text{off}} A_{\text{eff}}} \right). \quad (2.5)$$

Since the effective areas depend on the spectral index Γ of the γ -ray spectrum, they are re-weighted according to the measured energy spectrum in an iterative procedure.

As discussed in section 2.2.1, the optical efficiency of the telescope system degrades over time with respect to the simulations. A reduced optical efficiency leads to a decrease of the effective area for a given energy range. This is taken into account in equation 2.5 by looking up the effective area for each event for the reconstructed energy before optical efficiency corrections (Aharonian et al. 2006a). This can be understood as follows: the effective area is to first order not directly dependent on the energy, but on the total amount of light detected in the camera. The latter is proportional to the reconstructed energy without correction for the optical efficiency for a given set of lookup tables. Therefore, the effective area read out for the uncorrected energy of an event will give its corresponding effective area.

²In order to correct for spillover effects between neighboring energy bins due to the uncertainty in the energy reconstruction, the effective areas are derived as a function of the reconstructed energy (Aharonian et al. 2006a).

The statistical error on the differential flux is set according to the errors of the γ -ray excess in the given energy range, as described in the last section. The statistical error on the effective area due to the limited number of Monte Carlo simulations is negligible. The systematic uncertainties due to uncertainties in the underlying γ -ray and detector simulations are however significant and will be discussed in section 2.2.5.

2.2.4 Lightcurve measurement

For small time intervals or weak sources, the on- and off-event counts from a given γ -ray source might not provide enough statistics to derive an energy spectrum. However, under the additional assumption that the γ -ray energy spectrum is well approximated by a power law with a photon index Γ , an integral flux can be derived. The normalization of this power law can be estimated by comparing the total excess to the excess expected for a power law with a normalization of one between the energies E_1 and E_2 , defined as the *exposure* Δ :

$$\Delta = \int \int_{E_1}^{E_2} E^{-\Gamma} A_{\text{eff}}(E, t, \Gamma) dE dt. \quad (2.6)$$

The optical degradation of the telescope system with respect to the simulations is taken into account by integrating over the effective areas corresponding to the uncorrected energies, in analogy to the spectrum reconstruction. The normalization of the power-law energy spectrum of the source is then given by:

$$\Phi_0 = \frac{N_{\text{excess}}^{E_1-E_2}}{\Delta}, \quad (2.7)$$

resulting in an integral flux between the energies E_1 and E_2 of:

$$F_{E_1-E_2} = \int_{E_1}^{E_2} \Phi_0 E^{-\Gamma} dE = \Phi_0 \frac{E_1^{-\Gamma+1} - E_2^{-\Gamma+1}}{\Gamma - 1}. \quad (2.8)$$

The statistical error of the integral flux is obtained by propagating the uncertainty of the γ -ray excess. In addition to the systematic error due to the simulations, there is the systematic uncertainty caused by the assumption of a power-law spectrum with a spectral index Γ . However, as will be shown in the next section, the integral flux is not very sensitive to this assumption.

2.2.5 Systematic errors

The main source of systematic errors are the uncertainties in atmosphere properties used in the simulations, such as density, or cloud and dust profiles. These quantities directly affect the total Cherenkov light yield in the H.E.S.S. camera for a given energy. Additional systematic errors arise from the detector and shower interaction simulations.

These systematic uncertainties can be divided in two components. The first one is the uncertainty in the overall normalization of the energy scale. This component is dominated by uncertainties in the mean detector response and uncertainties on the mean values of atmospheric profiles. This error is estimated to be $\sim 15\%$ by comparing the reconstructed energies of events obtained with different shower and detector simulations. For energy spectra and integral fluxes this yields an uncertainty depending on the spectral slope of the source. For sources such as PKS 2155-304 with a spectral index around ~ 3.4 , this yields an uncertainty of $\sim 35\%$ on the normalization of the fluxes. Furthermore, the energy dependence of these uncertainties also leads to a systematic error on the slope of energy spectra of ~ 0.1 in spectral index.

The second component of the systematic error is variable in time and comes from changes in the atmospheric conditions and the detector response. These changes are hard to quantify and depend on the time scale in question. The main component comes from the seasonal

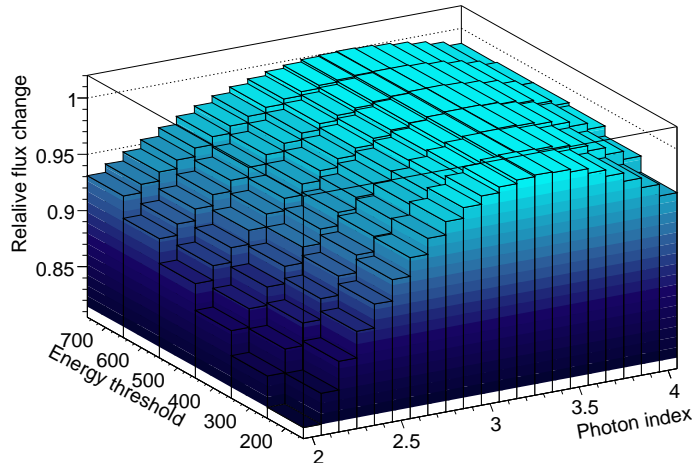


Figure 2.8: Relative changes of the integral flux above an energy E as a function of the assumed spectral index. The relative flux variations have been normalized to the flux derived for a spectral index of 3.4 for each energy. The figure was derived for *loose cuts*, an offset of 0.5° and a zenith angle of 20° .

changes in atmospheric conditions. This leads to a variation in the energy scale of $\sim 10\%$ at the H.E.S.S. site (Bernlohr 2000; Aharonian et al. 2006a). This effect is partly compensated by the fact that H.E.S.S. usually observes sources around one fixed period of the year. This is because observations are usually taken around the highest culmination of the source at the H.E.S.S. site to assure the lowest possible energy threshold.

On shorter time scales, between minutes and nights, systematic errors have not been studied in detail. While the detector is expected to be stable on these time scales, atmospheric conditions are generally not. However, the stability of the atmospheric conditions can be tested by observing the overall trigger rate of the H.E.S.S. telescopes. As mentioned before, the dominant part of triggered events come from cosmic rays. As the cosmic ray flux is constant, any change in the overall trigger rate must come from changes in the atmospheric conditions. The stability of the overall trigger rate is therefore a robust test of the atmospheric stability and was always performed if time scales of this order are discussed in this work, as will be presented in the next section.

In addition to these systematic errors due to uncertainties in the simulations, integral fluxes derived with the technique described in the last section have a systematic error related to the assumed photon index. The dependency of the integrated flux on this assumption is complex, because the spectral index enters multiple times in equations 2.6 and 2.8. Additionally, the dependency of the effective area on this parameter depends on the selection cuts used, the zenith angle and wobble offset of the observations. Figure 2.8 shows the relative dependency of the integral flux on the assumed spectral index above a given energy for typical parameters throughout this work. The typical spectral index of PKS 2155-304 is ~ 3.4 , with variations on the order of 0.2. As shown in figure 2.8 the integral flux depends only very weakly on the assumed spectral index in this range, with relative flux variations smaller than 2%, making this systematic error negligible.

2.2.6 Data quality

In order to assure a good quality of the data, several quality selection cuts are applied. For a summary of the run selection criteria see Aharonian et al. (2006a). The main parameter

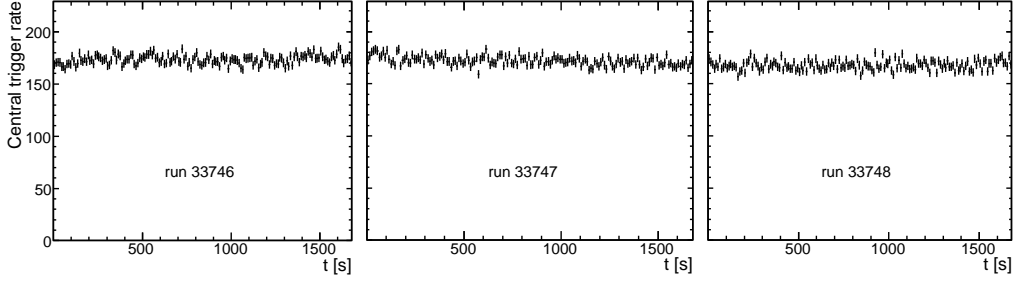


Figure 2.9: System trigger rate during the three runs taken on the night of the Big Flare (28 July 2006; for an example of a run with a rejected trigger rate see Aharonian et al. (2006a).

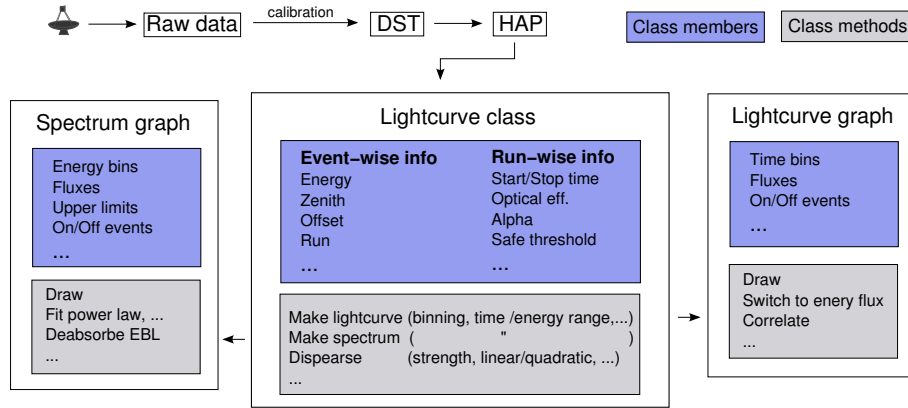


Figure 2.10: Data flow in H.E.S.S..

to check the atmospheric conditions during a run is the system trigger rate. Data with a mean trigger rate below 70% of the predicted value are not considered in the analysis (as discussed by Funk et al. (2005)). Also, runs with a RMS of the trigger rate above 10% from the mean value are not considered.

For runs where short time scale analysis is performed, the quality of the data is checked in more detail by visual inspection. This was the case in this work for the night of the two flares presented in chapter 3. As an example, figure 2.9 shows the trigger rate during the three runs taken on the night of 28 July. As can be seen, the trigger rate remains stable during the night. In addition to the system trigger rate, multiple other parameters are checked, such as the event rates after selection cuts, the distribution of the center of gravity of shower images in the cameras, or the participation level of each telescope to the triggered events.

2.2.7 Software implementation

The data flow of the H.E.S.S. analysis is shown in figure 2.10. Events are written to raw data files. Afterwards, they are calibrated and written into *Data Summary Tables* (DST), which contain a reduced set of calibrated data taken from the raw images. The DSTs are then analyzed by the *H.E.S.S. Analysis Program* (HAP), which is the main analysis software used within H.E.S.S.. It was developed during the implementation of this work with the aim to restructure existing code in a more comprehensive way and to make the analysis application more user-friendly. Several other software frameworks are also used within the H.E.S.S. collaboration and used to cross-check results.

During this work a lightcurve and spectrum generating software for HAP was developed.

The general structure is shown in figure 2.10. After background modeling, all events within the on- and off-regions are written into a *Lightcurve* object, which contains only the reduced set of information necessary for generating lightcurves and spectra. These are generated with the methods described in the sections 2.2.3 and 2.2.4. The *Lightcurve* object may be written to disk, avoiding the need to reanalyze the entire data when changing the parameters of the analysis. This greatly improves the speed of the analysis, allowing to generate new lightcurves and spectra for a given data set in a few seconds. Spectra and lightcurves are saved into corresponding *Lightcurve Graph* and *Spectrum Graph* classes. These classes contain several methods which are typically applied on these objects, such as cross-correlations for light curves or fitting for spectra.

Chapter 3

VHE observation of PKS 2155-304 from 2005 to 2007

In this chapter the results of the H.E.S.S. observations of PKS 2155-304 between 2005 and 2007 are presented. The source had a typical flux level of approximately $\sim 20\%$ of the Crab Nebula flux during these observations. In July 2006, however, the source showed a strong flaring activity, which reached its maximum on the nights of 28 and 30 July. Before focusing on this exciting event, an overview over the observations during the entire 2005 to 2007 observations will be given in this chapter, which is organized as follows: an overview of the analyzed dataset is given in section 3.1, the temporal flux variations are discussed in section 3.2 and a time-resolved spectral analysis will be given in section 3.3.

An in depth analysis of the flare of 28 July will be presented at the end of this chapter, in section 3.4. During this flare the source revealed a particularly fast flux variability. The flare observed on July 30 occurred during simultaneous observations of X-ray and optical instruments. The results of this multi-wavelength campaign will be presented in the next chapter, together with a detailed VHE analysis of this flare.

3.1 Dataset description

As all known VHE-emitting blazars in the southern hemisphere, PKS 2155-304 is monitored on a regular basis with the H.E.S.S. telescopes. It is typically observed during a few hours during the observation periods¹ of June to September, where the source is visible under small zenith angles. Between 2005 and 2007, the source was observed for 235 runs of 28 minutes each. Out of these runs, 180 fulfill the standard quality criteria specified in section 2.2.6. Out of these 180 runs, 170 were taken with four telescopes in operation. In order to have a homogenous dataset – minimizing systematic effects – only these runs are considered in this work. They yield a total live time of 74.4 hours after dead-time corrections.

The γ -ray excess from the direction of the source is shown in figure 3.1. In total, 82222 γ -ray excess events were detected, yielding a source significance of 265.5σ (equation 2.3). The excess is point like, taking into account the point spread function of H.E.S.S., with a best fit position of $\alpha_{RA} = 21^h 58^m 52.6^s \pm 0.1^s_{stat} \pm 1.5^s_{sys}$ and $\delta_{dec} = -30^\circ 13' 29.8'' \pm 1.3''_{stat} \pm 20''_{sys}$, consistent with the position of PKS 2155-304: $\alpha_{RA} = 21^h 58^m 52.0651^s$ and $\delta_{dec} = -30^\circ 13' 32.118''$ (Ma et al. 1998).

The mean zenith angle of the observations is 19.4° and the mean safe energy threshold of the analysis is 200 GeV. Due to the exceptional flares recorded during these observations, some runs were taken at unusually high zenith angles; therefore, their energy threshold can deviate a few hundred GeV from this mean value. This will make flux extrapolations to

¹One observation period is defined by one moon cycle. They are usually referred to according to the month where most of the observation time was taken.

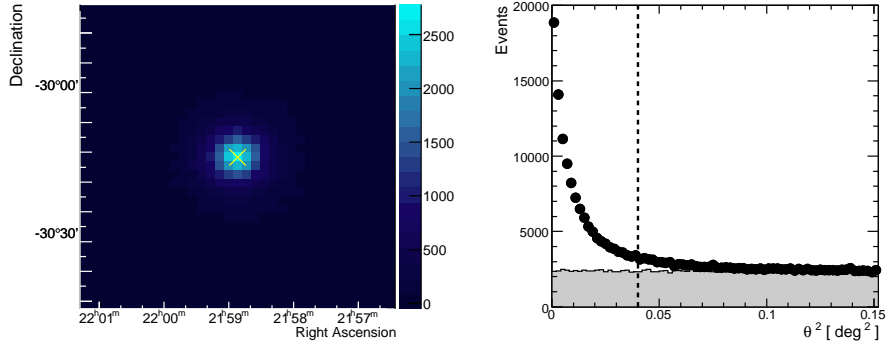


Figure 3.1: *Left panel:* γ -ray excess from the direction of PKS 2155-304 between 2005 and 2007 (uncorrelated). The yellow cross marks the nominal position of the blazar. *Right panel:* γ -ray excess as a function of the squared angular distance θ^2 from the nominal source position (black markers). The gray area shows the expected γ -ray background, estimated from regions of the source. The dashed line shows the cut on θ^2 applied during the γ -ray selection (see 2.2.2).

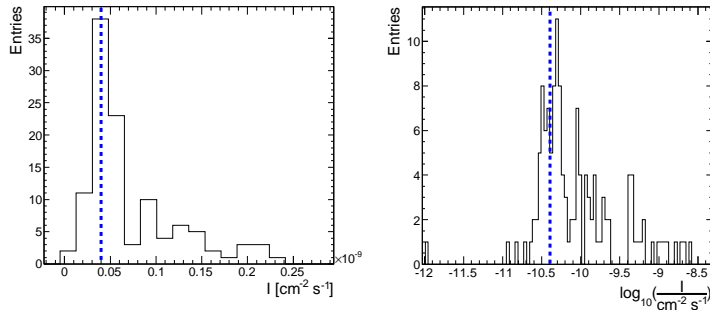


Figure 3.2: Distribution of the integral flux for each run of observations between 2005 and 2007. The right panel shows the entire distribution in logarithmic scale. The left panel is zoomed in around the maximum of the distribution in a linear scale. The blue dashed line corresponds to the reference flux (see text).

lower energies necessary at some points for a unified representation of the data, as will be discussed in the next section.

3.2 Temporal analysis

The typical flux observed from PKS 2155-304 above 200 GeV is approximately $I_0 = 4 \times 10^{-11} \text{ cm}^2 \text{ s}^{-1}$, which corresponds to $\sim 20\%$ of the flux from the Crab Nebula. As can be seen in figure 3.2, the distribution of integral fluxes measured in each run is peaked around I_0 and has a wide tail towards higher fluxes. The flux I_0 is also compatible with the average fluxes found in the 2002 to 2004 campaigns on this source (Aharonian et al. 2005a,b; Punch 2007) and is therefore defined as a *reference flux*².

²Whether or not this flux represents a quiescent state – in the sense that it is a steady flux component of this source, which is present at all times – is a question which remains to be answered. This matter is currently being investigated and is not trivial, since observation runs are not taken randomly in time, but preferably during periods of high activity of the source.

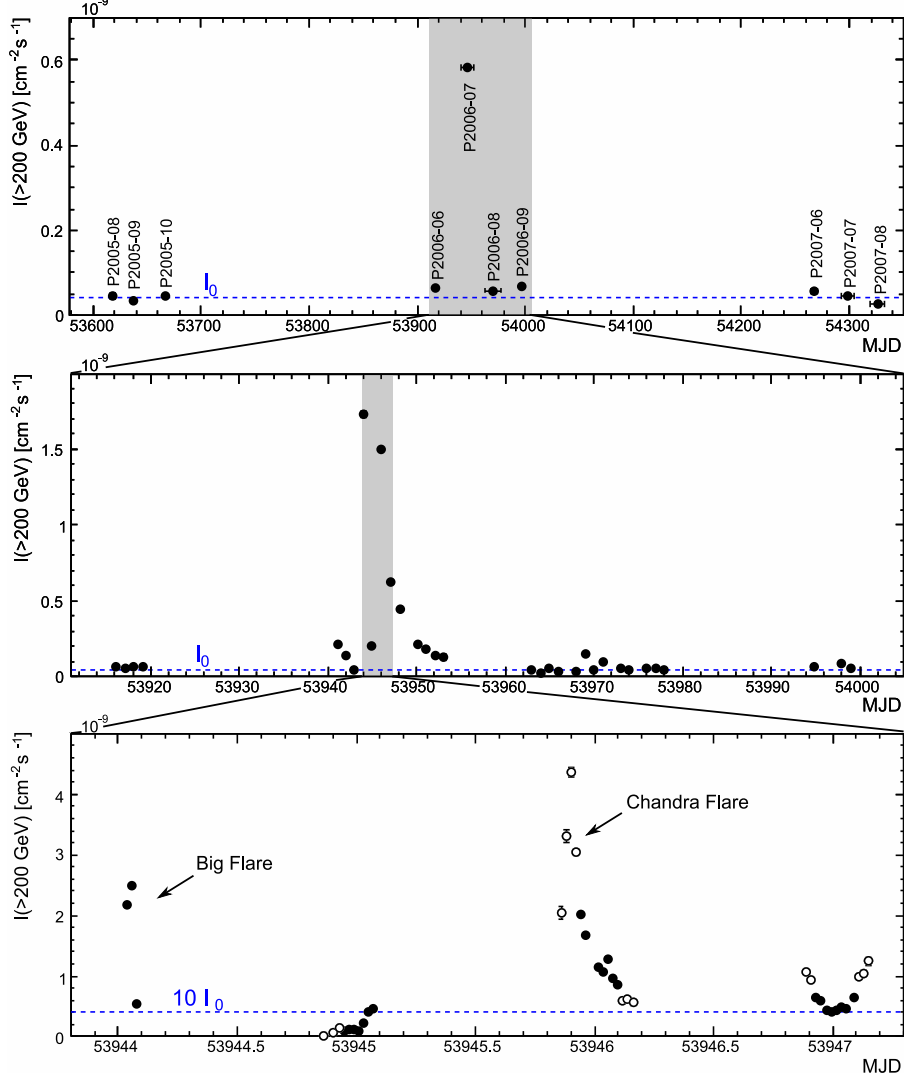


Figure 3.3: Integral flux above 200 GeV over time from PKS 2155-304 during the 2005 to 2007 observations. The top panel shows the average flux values measured in each observation period; the middle panel shows the average fluxes measured in each night for the 2006 campaign (corresponding to the shaded area in the top panel); the lowest panel the run-wise fluxes for the night of MJD 53944 to 53947 (corresponding to the shaded area in the middle panel). Open symbols show flux values where flux extrapolations were performed, since the safe threshold of these runs was above 200 GeV. These extrapolations were done over an average energy range of ~ 150 GeV, assuming a power-law spectrum with a photon index of 3.4. For a photon index variation of 0.2, this leads to an additional uncertainty of $\lesssim 10\%$ on the flux. This error is not considered in the error bars, which only show statistical errors. The blue dashed line shows the reference flux.

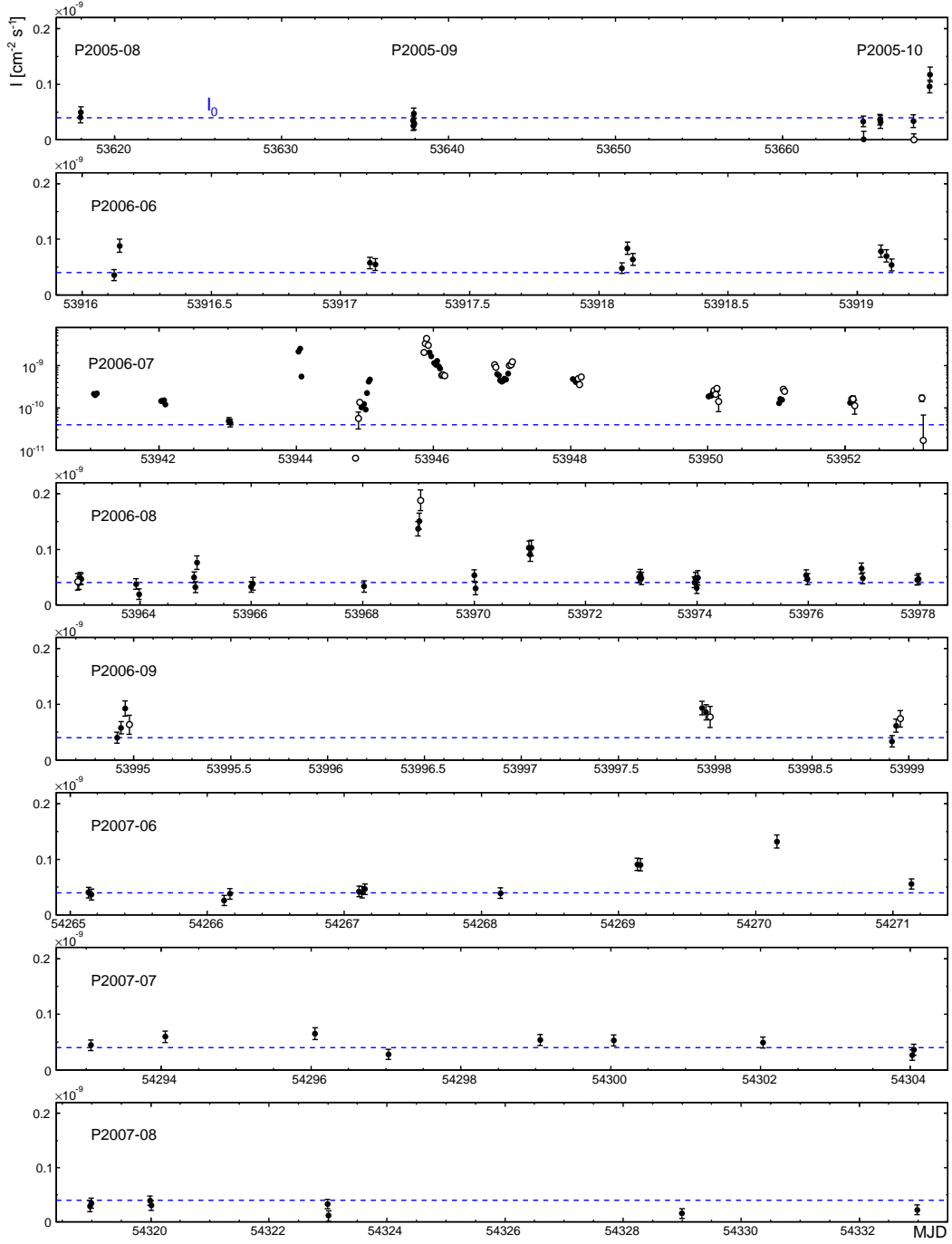


Figure 3.4: Run-wise integral flux above 200 GeV over time during the 2005 to 2007 observations. The Y-axis of the July 2006 period P2006-06 is shown in logarithmic scale to show the full range of flux variations. Open symbols mark flux values where flux extrapolations to the given energy were performed, leading to an additional flux uncertainty of $\lesssim 10\%$ (see caption of figure 3.3).

In 2005 and 2007, the mean flux observed from PKS 2155-304 was close to the reference flux. In 2006, however, it was significantly higher during the entire observation campaign (see figure 3.3). This activity peaked in July, where the source was highly active. During two nights, on 28 and 30 July (MJD 53944 and MJD 53946 respectively), the source exhibited flux values exceeding $4 \times 10^{-9} \text{ cm}^2 \text{ s}^{-1}$, more than 100 times above the reference flux. As mentioned in chapter 1, these flares are referred to as the Big Flare (28 July) and the Chandra Flare (30 July). The fluxes measured during these nights are among the highest ever measured in VHE astronomy; γ -rays were detected at a frequency of a few Hz. These extraordinary events will be analyzed in more detail in section 3.4 and chapter 4.

PKS 2155-304 shows flux variability on all the time scales which can be resolved, from monthly flux variations (apparent in figure 3.3), down to minute time scales (as will be discussed in sections 3.4 and 4.1). It can therefore be misleading to speak about “nightly” or “monthly” fluxes, as the values measured during the limited time of the observations might not be representative for the entire night or month. A more accurate picture of the flux variations can be gained by considering run-wise fluxes. The evolution of the run-wise fluxes over time for the entire 2005 to 2007 campaign is shown in figure 3.2. It can be seen that outside of the phase of high activity in July 2006, the run-wise flux is usually close to the reference flux, although even during less active periods there are a few runs with fluxes significantly higher than the reference flux (e.g. on the nights of MJD 53669, 53969 and 54269-70). During the active period of July 2006, the fluxes are high for most of the observation runs. Only the fluxes measured on MJD 53943 and MJD 53953 are not above the reference flux. There is significant intra-night variability during most of the observed nights in July 2006, most pronounced during the two major flares and their following nights.

3.3 Spectral analysis

Spectral analysis often entails a compromise. On the one hand, one wants to maximize the event statistics to resolve finer structures by increasing the time window of the measurement. On the other hand, if the energy spectrum of the source is variable in time, it is difficult to interpret spectra averaged over long time periods. As will be shown later in section 3.3.2, PKS 2155-304 indeed shows spectral variability. Since these variations are relatively small, the overall time-averaged spectrum will be discussed first to give a general overview.

3.3.1 Time-averaged energy spectrum

The time-averaged energy spectrum of PKS 2155-304 during the 2005 to 2007 observations is shown in figure 3.5. In order to maximize the energy coverage, only runs with a safe threshold below 200 GeV were considered for this measurement. The measured spectrum is generally steep, with a photon index of 3.35 ± 0.01 for a power-law fit. A simple power-law, however, gives no good representation of the data at higher energies, as the spectrum is significantly curved. In order to parameterize this curvature the spectrum was fitted with a three-parameter function: a *log-parabolic model* ($\Phi(E) = \Phi_0 E^{-\Gamma-b \log(E)}$) and a four-parameter function: a *broken power-law* (see equation 1.20). A summary of the fit results is given in table 3.1. The χ^2 -probabilities P_{χ^2} of the fit show that the measured spectrum is best described by a broken power law with a break around 400 GeV, where the photon index softened by $\Delta\Gamma \sim 0.7$. A log-parabolic model with a curvature parameter of $b = 0.77 \pm 0.05$ only gives a marginally acceptable description of the data, with $P_{\chi^2} = 2\%$.

As discussed in section 1.5, the VHE emission from blazars is severely affected by absorption on the Extragalactic Background Light. In order to infer the intrinsic spectrum of the source, the measured one is deabsorbed with the maximal and minimal EBL models introduced in section 1.5. The intrinsic source spectrum obtained with each model is shown in figure 3.5. These spectra are softer than the measured spectrum, with photon indices around 2.5. The spectra are still significantly curved with respect to the pure power-law. However,

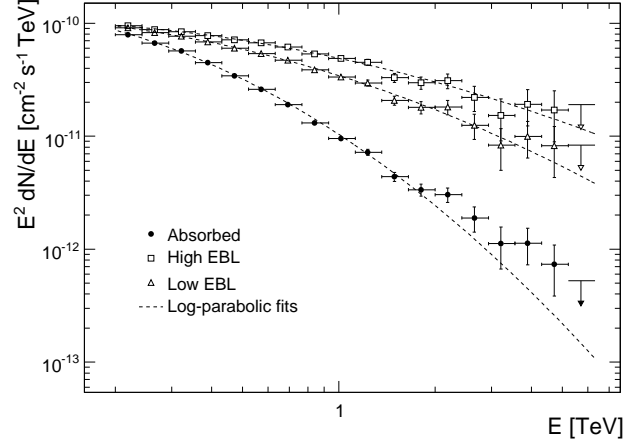


Figure 3.5: Time-averaged energy spectrum during the 2005 to 2007 observations. Black circles show the measured spectrum. Open symbols show the intrinsic source spectra, obtained after deabsorption with the minimal (triangles) and maximal (squares) EBL model.

this curvature is less pronounced after deabsorption, with best fit value of $b \sim 0.33$ for the log-parabolic model (see table 3.1). In contrast to the measured spectrum, the deabsorbed ones are well described by this model, showing that the break around 400 GeV measured in the absorbed spectra is not intrinsic to the source: it is a result of the convolution of the source intrinsic curvature in the spectrum and the strong increase in EBL absorption with increasing γ -ray energies up ~ 1 TeV (see figure 1.9).

It should be noted that power-law with an exponential cutoff ($\Phi(E) = \Phi_0 E^{-\Gamma} e^{-E/E_{\text{cut}}}$) also provides a good description of the data. This function has the same degrees of freedom as the log-parabolic model and is often used to fit VHE spectra. For the energy spectra shown throughout this work, it yielded similar χ^2 -probabilities than the log-parabolic model, with typical break energies of $E_{\text{cut}} = 1 - 2$ TeV. However, in the absence clear break in the spectrum – as found throughout this work – the log-parabolic model is usually preferred, as the exponential cutoff model tends to match a given curvature by using a specific section of its cutoff region, pushing the power-law component outside the observed energy range. A further advantage of the log-parabolic model is that it fits well the typical shape the Spectral Energy Distribution of blazars around the maximum of the Inverse Compton peak (E_{peak} , defined by $\Gamma(E_{\text{peak}}) = 2$). This allows a straightforward estimate of the peak position of the SED from the curvature itself, with a minimum number of free parameters (see e.g. Tramacere et al. 2007). Interestingly for the spectra at hand, the SED peak estimate is almost independent of the EBL level, ranging between 70 and 90 GeV (see table 3.1). This peak position is just below the energy range covered by H.E.S.S..

Table 3.1: Fit results for the time-averaged energy spectrum of the 2005 to 2007 observations (shown in figure 3.5) and for the spectra obtained after EBL deabsorption with the minimal and maximal EBL model introduced in section 1.5. The last two columns show the χ^2 per degree of freedom of the fit and the according χ^2 -probability. Also shown is the energy flux between 0.3 and 3 TeV for the fitted model. The latter will be given for all the spectra fitted in this work, for an easy comparison of the energy output between different spectra (the energy range was chosen as such, that it is covered by most of the spectra presented in this work). The estimated peak E_{peak} position of the SED obtained by extrapolating the log-parabolic model to lower energies is also shown. No statistical errors are given on E_{peak} , as its uncertainty is expected to be dominated by the assumed extrapolation function and the assumed EBL level for deabsorbed spectra.

PL	Φ_0 $\text{cm}^{-2}\text{s}^{-1}\text{TeV}^{-1}$	Γ			$F_{0.3-3 \text{ TeV}}$ $\text{ergs cm}^{-2} \text{s}^{-1}$	χ_r^2 (d.o.f.)	P_{χ^2}
Absorbed	$1.13 \pm 0.02 \times 10^{-11}$	3.35 ± 0.011	-	-	6.55×10^{-11}	18.4 (15)	0
Min. EBL	$3.60 \pm 0.05 \times 10^{-11}$	2.65 ± 0.012	-	-	1.51×10^{-10}	5.20 (15)	1.6×10^{-11}
Max. EBL	$5.07 \pm 0.07 \times 10^{-11}$	2.44 ± 0.012	-	-	2.00×10^{-10}	3.23 (15)	2.15×10^{-5}
Log-parabolic	Φ_0	Γ	b	E_{peak} (TeV)	$F_{0.3-3 \text{ TeV}}$	χ_r^2 (d.o.f.)	P_{χ^2}
Absorbed	$1.04 \pm 0.02 \times 10^{-11}$	3.86 ± 0.044	0.771 ± 0.058	0.06	6.62×10^{-11}	1.91 (14)	0.0205
Min. EBL	$3.45 \pm 0.06 \times 10^{-11}$	2.89 ± 0.037	0.376 ± 0.050	0.07	1.45×10^{-10}	0.56 (14)	0.896
Max. EBL	$4.92 \pm 0.08 \times 10^{-11}$	2.61 ± 0.035	0.275 ± 0.047	0.08	1.92×10^{-10}	0.65 (14)	0.828
Broken PL	Φ_0	Γ_1	Γ_2	E_{break} (TeV)	$F_{0.3-3 \text{ TeV}}$	χ_r^2 (d.o.f.)	P_{χ^2}
Absorbed	$1.94 \pm 0.10 \times 10^{-11}$	2.94 ± 0.040	3.66 ± 0.032	0.40 ± 0.015	6.70×10^{-11}	1.25 (13)	0.234
Min. EBL	$4.20 \pm 0.12 \times 10^{-11}$	2.52 ± 0.024	2.92 ± 0.053	0.57 ± 0.049	1.45×10^{-10}	0.82 (13)	0.636
Max. EBL	$5.58 \pm 0.14 \times 10^{-11}$	2.36 ± 0.020	2.71 ± 0.068	0.67 ± 0.075	1.91×10^{-10}	0.61 (13)	0.845

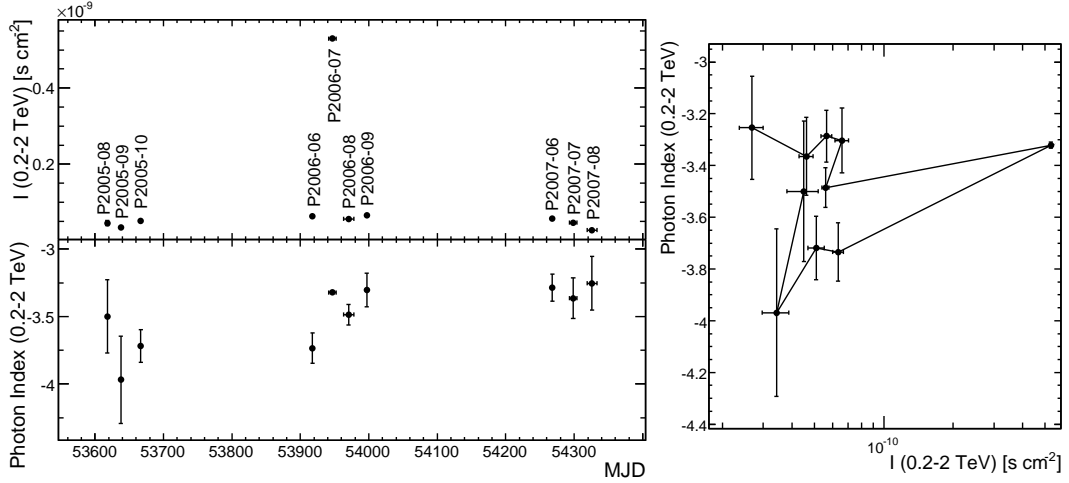


Figure 3.6: *Left panel:* integral flux and photon index between 0.2 and 2 TeV for each observation period between 2005 and 2007. *Right panel:* correlation between integral flux and photon index.

3.3.2 Spectral variability

In order to assess the spectral variability over time, energy spectra were measured separately for all observation periods between 2005 and 2007. A robust way to quantify the spectral hardness is to fit a power law to common energy ranges and compare the photon index, which traces the hardness of the spectrum independently of the exact spectral shape. The evolution of the spectral index between 0.2 and 2 TeV for the observation periods from 2005 to 2007 is shown in figure 3.6. There is no strong spectral variability, as the spectrum is always steep, with an mean value of 3.33 ± 0.01 in this energy range. However, the χ^2 -probability for a constant fit is only 0.02%, showing that there is a small – but significant – spectral variability present. This is mainly due to two effects:

- The spectral index shows a decrease over time. In 2005, the mean photon index is 3.71 ± 0.11 , while it is 3.3 ± 0.08 in 2007. The average energy spectrum in 2007 is therefore harder than in 2005 at a $\sim 3\sigma$ level. However, as these measurements were taken two years apart, it is also possible that there were systematic changes in the telescope system or atmospheric conditions, making it reasonable to consider the full systematic error of 0.1 on the photon index discussed in section 2.2.5. The hardening is therefore not significant enough to draw any definite conclusions.
- The spectrum during the active period of July 2006 is harder than the average spectrum outside of that period, at a level $\sim 4\sigma$, with mean photon indices of 3.32 ± 0.01 and 3.48 ± 0.04 respectively. This suggests a spectral hardening with increasing flux levels, as it is often seen for blazars at VHE (see section 1.2). This behavior can also be seen marginally in the correlation figure in the left panel of figure 3.6 and will be analyzed in more detail in the following.

When analyzing the spectral properties during observation periods, various flux levels are averaged. In order to assess the spectral variability as a function of integral flux with more precision, it is better to group the dataset in flux bands, and to calculate average spectra for each of them. In this work the data was divided into seven flux bands on a run-wise basis. The analysis was performed for all runs with a safe threshold up to 300 GeV, in order to include more runs during high flux states compared to the threshold of 200 GeV used so far. The resulting correlation between flux and spectral index is shown in figure 3.7. The limits of the flux bands are indicated by gray dotted lines in this figure; they were chosen

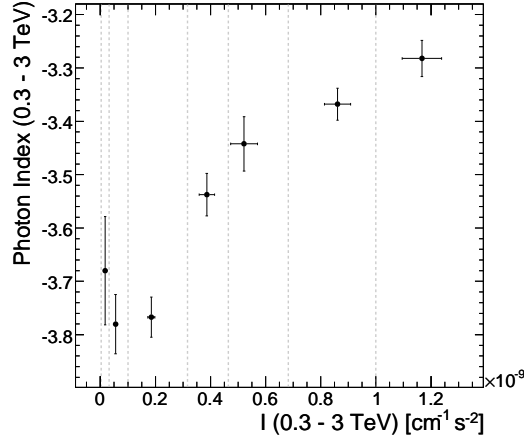


Figure 3.7: Photon index between 0.3 and 3 TeV as a function of the integral flux in the same energy range. The dotted gray lines show the flux ranges of the bands in which the dataset was divided on a run-wise flux basis.

in a way, that comparable event statistics are assured in each band. Figure 3.7 shows a clear “harder when brighter” trend in the data. The hardening is strongest between integral fluxes of $0.2 \times 10^{-9} \text{ cm}^{-2} \text{ s}^{-1}$ and $0.7 \times 10^{-9} \text{ cm}^{-2} \text{ s}^{-1}$, and is less pronounced at lower flux levels ($< 0.2 \times 10^{-9} \text{ cm}^{-2} \text{ s}^{-1}$).

3.4 The Big Flare

On the night of 28 July PKS 2155-304 showed the first major flare during the 2005 to 2007 observations. This flare was seen during three runs of normal monitoring observations on this source. The zenith angle of the observations was low ($< 25^\circ$), therefore all three runs have a safe threshold below 200 GeV. The combination of the exceptionally high fluxes with a wide coverage in energy provided an unprecedented photon statistic (11695 excess events). For the first time in VHE astronomy, this allowed to resolve lightcurves down to one minute resolution. The results of this exceptional night were published in Aharonian et al. (2007b) by the H.E.S.S. collaboration, with Wytan Benbow and Berrie Giebels as corresponding authors. In the following some of the findings of this publication will be recalled and complemented.

3.4.1 Temporal analysis

The lightcurve of the flare in one minute time bins is shown in figure 3.8. The lightcurve shown here differs slightly ($< 3\%$ point to point) from the one in the mentioned publication, as calibration problems were discovered after the publication, leading to a recalibration of the data. The most striking aspect of this lightcurve is its fast variability. This was quantified by fitting the flare with a superposition of five subflares – apparent in figure 3.8 – and a constant component. The subflares were parameterized by generalized Gaussian shapes (see Aharonian et al. (2007b)), showing rise and decay times of ~ 200 s. Such a parameterization of the flare relies on a somewhat arbitrary choice of fit function, but the variability time scale was also confirmed with a Fourier analysis. The Fourier power spectrum of this flare shows significant power above the noise level up to time scales of ~ 600 s (see figure 3.8). Interestingly it is compatible with a red noise process ($P_\nu \propto \nu^{-2}$), similar to what is found in X-rays for this source (Zhang et al. 1999).

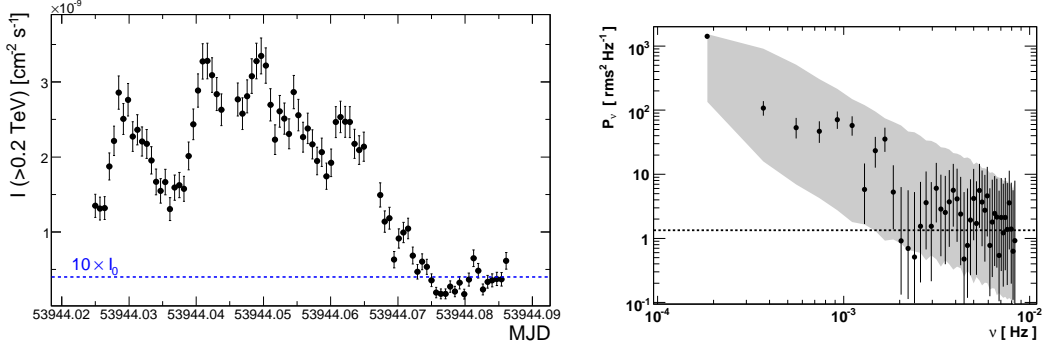


Figure 3.8: *Left panel:* integral flux above 200 GeV as a function of time for the night of 28 July in one minute time bins. The blue dashed line shows the reference flux multiplied by ten. *Right panel:* Fourier power spectrum of the lightcurve. The gray area corresponds to the 90% confidence interval for a lightcurve with a power-law Fourier spectrum $P_\nu \propto \nu^{-2}$ obtained from simulations. The horizontal line is the average noise level. The figure is reproduced from Aharonian et al. (2007b)

As discussed in section 1.3.1, these fast variability time scales constrain the size of the emitting region R via causality arguments for a given Doppler factor D . For the variability time scales at hand, this results in the following condition (Aharonian et al. 2007b):

$$D \geq (60 - 120) \frac{R}{R_S}, \quad (3.1)$$

where $R_S \approx 3 \times 10^{14}$ cm is the Schwarzschild radius of PKS 2155-304. R_S is usually expected to be the smallest size of an emission region in system accreting on a black hole. If this is the case, Eq. 3.1 implies that the Doppler factor of the emitting region is likely larger than 60, much higher than the typical values usually expected for blazars ($D \sim 10$). This value is also higher than the Doppler factors of a few inferred from the superluminal motion of knots seen by VLBI inside of the jet (Piner & Edwards 2004). However, the connection of these radio knots to the radiation region of γ -rays is not clear.

It is interesting to note that the evolution of the lightcurve in different energy bands shows no sign of relative time delays, as will be discussed in chapter 5. Anticipating the result here, a linear dispersion in the arrival times of the photons with energy must be smaller 73 s TeV^{-1} , at a 95% confidence level. This will be used later to set limits on the energy scale of Lorentz violations.

3.4.2 Spectral analysis

The time-averaged energy spectrum during the flare is shown in figure 3.9. Besides a difference in normalization of about one order of magnitude with respect to the time-averaged spectrum over the entire 2005 to 2007 observation, there is qualitatively little difference between the spectral shapes. As expected, the spectrum is however slightly harder, as can be seen by the photon index of 3.19 ± 0.02 obtained for a power-law fit (compared to 3.35 ± 0.01 for the entire 2005-2007 period). There is a significant curvature in the spectrum, best parameterized by a log-parabolic model, with a χ^2 -probability of 18% (see table 3.2). This result differs from the one published in Aharonian et al. (2006a), where the broken power-law fit gave a significantly better χ^2 -probability. This difference is due to the mentioned re-calibration of the data. However, while the χ^2 -probabilities of the fits are different, the best fit value for each parameter remain basically unchanged.

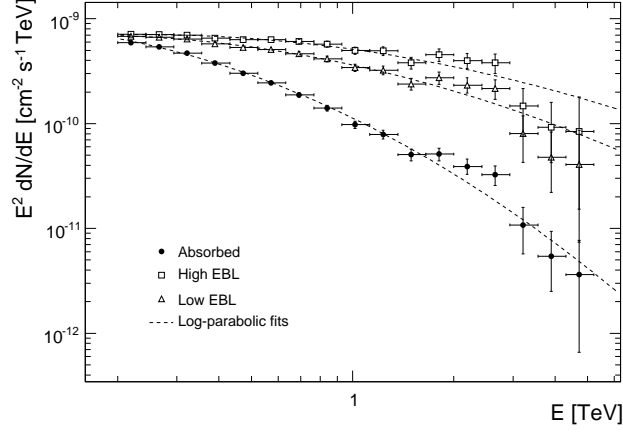


Figure 3.9: Time-averaged energy spectrum during the Big Flare. Black circles show the measured spectrum. Open symbols show the intrinsic source spectra, obtained after deabsorption with the minimal (triangles) and maximal (squares) EBL model.

The intrinsic energy spectrum of the source, obtained after EBL deabsorption, is shown in figure 3.9 for the minimal and maximal EBL models. These spectra also show a significant curvature, well described by a log parabolic or broken power law model. The curvature parameter b of the log-parabolic model is ~ 0.38 , similar to the time-averaged spectrum during the 2005 to 2007 observations. The peak of the SED estimated from the log-parabolic model falls between 150 and 230 GeV, indicating a shift of the SED peak towards higher energies by ~ 100 GeV during the flare.

To assess the spectral variability over time during the flare, spectra were measured in 7 and 14 minute time bins. The variable time binning was chosen to assure comparable event statistics in each bin. The evolution of the photon index over time for the night is shown in figure 3.10. The spectrum is significantly harder during the major part of the flare in the middle of the observation. The right panel of figure 3.10 shows the correlation between photon index and flux between 0.2 and 2 TeV. As for the entire 2005 to 2007 observations, a significant hardening with increasing flux can be seen. The change in spectral index is small ($\Delta\Gamma \sim 0.3$), but significant, with χ^2 -probability of 0.1% for a constant photon index. The correlations between photon index and flux does not follow a simple analytical function, as the spectral indices at the end and beginning of the night are very similar, despite the difference in flux of a factor of ~ 4 . It should be noted that no spectral variability was stated in the publication on this flare. Analysis at the time concluded that spectral variability, if present, can not be very strong (Aharonian et al. 2007b).

Table 3.2: Fit results for the time-averaged energy spectrum of the Big Flare (shown in figure 3.9) and the spectra obtained after EBL deabsorption with the minimal and maximal EBL model.

PL	Φ_0 $\text{cm}^{-2}\text{s}^{-1}\text{TeV}^{-1}$	Γ			$F_{0.3-3 \text{ TeV}}$ $\text{ergs cm}^{-2} \text{s}^{-1}$	χ_r^2 (d.o.f.)	P_{χ^2}
Absorbed	$1.11 \pm 0.02 \times 10^{-10}$	3.19 ± 0.018	-	-	5.86×10^{-10}	8.60 (15)	0
Min. EBL	$3.57 \pm 0.08 \times 10^{-10}$	2.48 ± 0.019	-	-	1.42×10^{-9}	4.13 (15)	1.16×10^{-7}
Max. EBL	$5.06 \pm 0.12 \times 10^{-10}$	2.27 ± 0.020	-	-	1.92×10^{-9}	3.39 (15)	8.52×10^{-6}
Log-parabolic	Φ_0	Γ	b	E_{peak} (TeV)	$F_{0.3-3 \text{ TeV}}$	χ_r^2 (d.o.f.)	P_{χ^2}
Absorbed	$1.13 \pm 0.03 \times 10^{-10}$	3.57 ± 0.057	0.686 ± 0.080	0.07	6.16×10^{-10}	1.33 (14)	0.182
Min. EBL	$3.64 \pm 0.09 \times 10^{-10}$	2.70 ± 0.047	0.420 ± 0.068	0.15	1.41×10^{-9}	0.91 (14)	0.551
Max. EBL	$5.15 \pm 0.13 \times 10^{-10}$	2.45 ± 0.044	0.353 ± 0.065	0.23	1.89×10^{-9}	1.06 (14)	0.392
Broken PL	Φ_0	Γ_1	Γ_2	E_{break} (TeV)	$F_{0.3-3 \text{ TeV}}$	χ_r^2 (d.o.f.)	P_{χ^2}
Absorbed	$1.98 \pm 0.16 \times 10^{-10}$	2.74 ± 0.063	3.49 ± 0.047	0.42 ± 0.025	6.17×10^{-10}	1.83 (13)	0.033
Min. EBL	$4.28 \pm 0.17 \times 10^{-10}$	2.33 ± 0.034	2.89 ± 0.100	0.75 ± 0.087	1.41×10^{-9}	1.32 (13)	0.191
Max. EBL	$5.81 \pm 0.21 \times 10^{-10}$	2.15 ± 0.031	2.71 ± 0.125	0.88 ± 0.127	1.88×10^{-9}	1.18 (13)	0.29

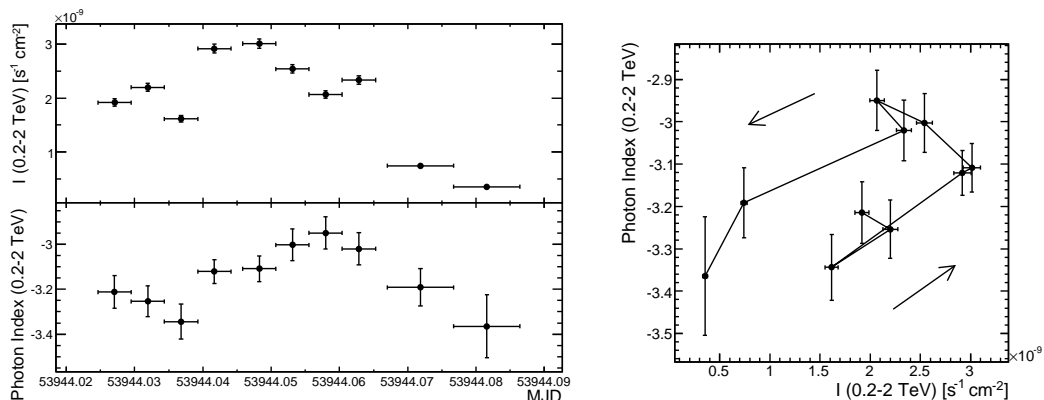


Figure 3.10: *Left panel:* integral flux and photon index between 0.2 and 2 TeV evolution over time. *Right panel:* correlation between integral flux and photon index. The arrows indicate the time evolution of the correlation.

3.4.3 Interpretation within blazar models

Recently, the VHE emission observed during the Big Flare was modeled within leptonic scenarios in several publications, all of which will be briefly discussed in the following. These models have to explain the fast variability measured during the flare as well as the observed energy spectrum.

Kusunose & Takahara (2008) and Ghisellini & Tavecchio (2008) fitted the energy spectrum during the Big Flare with a simple SSC model. Both models are slightly modified versions of the SSC model presented in section 1.4.1 (e.g. Kusunose & Takahara (2008) assumes a electron spectrum described by a power law with an exponential cutoff instead of the broken power law in section 1.4.1). In order to extract meaningful results within SSC models, the synchrotron component needs to be constrained. Therefore, these authors assumed that the X-ray flux observed by Swift from PKS 2155-304 on the night after the Big Flare is close to the values during this night. This assumption is plausible, since the X-ray flux variations during the entire SWIFT observations between MJD 53945 and MJD 53969 are much smaller than the ones observed in γ -rays (Foschini et al. 2007). Both authors conclude that a simple SSC model can describe the fitted SED. The parameter values obtained with both models are similar, with a Doppler factor of 60/100, an emission region radius of $3/5 \times 10^{14}$ cm and a magnetic field of 0.1/0.5 G for the model of Ghisellini & Tavecchio (2008) and Kusunose & Takahara (2008), respectively.

The cooling and light-crossing time in both of the mentioned models is short enough to accommodate the observed variability times; however, neither of the publications gives a detailed modeling of the γ -ray emission over time. This was done by Katarzyński et al. (2008), with a complex SSC model composed of multiple emission regions: five flaring regions, responsible for the five subbursts observed during the flare, and one constant “quiescent” component. The five flaring regions just differ in electron density and sizes. The model is inhomogeneous, as the evolution of electrons and photons is traced in space and time inside of the emission regions. The authors conclude that they can reproduce the lightcurve of the Big Flare with Doppler factors of ~ 30 for the five emission regions.

In Ghisellini & Tavecchio (2008), the authors also applied an External and an Ambient Compton scenario (see section 1.4.1). Both models can also account for the observed SED, while assuring light-crossing and cooling times compatible with the observed variability time. The Doppler factor, size and magnetic field of the emission region in these models are similar to the ones obtained for the SSC models ($D \sim 60$, $R \sim 3 \times 10^{14}$ cm and $B \sim 1$ G). This shows that, while there is a qualitative agreement between the different models on the properties of the emitting region, a more dense multi-wavelength coverage is required to

distinguish between them. This goal was achieved during the Chandra Flare, which occurred two nights later and will be discussed in the next chapter.

Chapter 4

The Chandra Flare - An unprecedented multi-wavelength view

Since the first light of H.E.S.S., a project was developed with specific Target of Opportunity (ToO) proposals to investigate the fast variability timescales of blazars with a whole night (6-8 hours) of continuous, simultaneous multi-wavelength observations during a bright γ -ray state. To this aim, in the X-ray domain Chandra was chosen, because it is the only X-ray satellite capable of full coverage of the entire H.E.S.S. visibility window during most of the year, without the interruptions typical of low-orbit satellites. Following the first days of activity of PKS 2155-304 in July, ToO observations were triggered – also for other X-ray satellites like RXTE and SWIFT – in order to sample the source behaviour over several days and weeks. Unfortunately, the dramatic outburst during the Big Flare on 28 July was too early with respect to the already-triggered but not-yet-started X-ray observations. Therefore, this event of exceptional variability remained without multi-wavelength coverage.

Two nights later, however, on July 30 (MJD 53946), a second flare was observed. This so called Chandra Flare coincided with the Chandra-H.E.S.S. ToO campaign, and with further coverage in the optical band provided by the Bronberg Observatory in South Africa. Snapshot observations of few ks were also taken with RXTE. In this chapter, the multi-wavelength results of this night will be presented. This work was done together with Luigi Costamante, who was the main responsible of the X-ray analysis. The results are currently being prepared for publication on behalf of the H.E.S.S. collaboration. This chapter is a modified version of the current state of this paper; it is organized as follows: the observational findings are given in section 4.1 for the timing analysis and in section 4.2 for the time-resolved spectral analysis. In section 4.3 the flux and spectral correlations between X-ray and γ -ray bands are discussed. In section 4.4 a brief summary of the main observational findings is provided, before discussing the results in the context of the blazar physics in section 4.5.

As this is a very rich and complex dataset, the data will be divided in several subsets. This is done to emphasize different aspects of the observation; for instance, times of similar spectral properties will be averaged to achieve higher event statistics; at other times it will be useful to focus on time windows of maximal and minimal fluxes to emphasize the range of spectral variations. The different subsets used in this chapter are listed and labeled in table 4.1. Each of them will be introduced when it first appears in the text. For simplicity, in this chapter the values of MJD will be given as $\text{MJD}_0 = \text{MJD} - 53900$.

Table 4.1: Summary of various subsets of the VHE data used in this chapter. The label, start/stop times and duration t of each dataset are listed. The number in each label refers to the minimal common energy threshold E_{thr} of the H.E.S.S. observations in GeV during that period. The fifth column shows the number of the figure in which each time window is illustrated. The last column gives a brief comment describing each dataset.

Label	MJD ₀ start	MJD ₀ end	t [h]	Fig.	Comment
T200	45.934618	46.107844	4.16	4.1	Period with $E_{\text{thr}} < 200$ GeV
T300	45.913536	46.129121	5.17	4.1	Period with $E_{\text{thr}} < 300$ GeV
T400	45.892483	46.150125	6.18	4.1	Period with $E_{\text{thr}} < 400$ GeV
T500	45.871450	46.171258	7.20	4.1	Period with $E_{\text{thr}} < 500$ GeV
T700	45.850393	46.171258	7.70	4.1	Period with $E_{\text{thr}} < 700$ GeV
T300-SIM	45.922130	46.129121	4.96	4.3	HESS-Chandra period
T300-SIMMAX	45.922130	45.944699	0.54	4.3	Max. flux during T300-SIM
T400-SIMMIN	46.100000	46.150000	1.20	4.3	Min. flux during T400
T300-RXTE	46.016846	46.033328	0.73	4.3	HESS-RXTE-Chandra period
	46.084624	46.098698			
T400-PEAK	45.896643	45.920474	0.57	4.8	Max. γ -ray flux
T300-HIGH	45.913530	45.970312	1.36	4.7	High γ -ray flux in T300
T300-LOW	46.013252	46.129166	2.78	4.7	Low γ -ray flux in T300

4.1 Temporal analysis

4.1.1 γ -ray lightcurves

The measured γ -ray lightcurve in two-minute time bins is shown in figure 4.1, divided in five different energy bands. As one can see, the time coverage increases with threshold energy, due to the mentioned zenith angle effect. A full coverage of the observation is thus reached for energies above 700 GeV (during the period T700, see table 4.1), while lightcurves (and spectra) down to ~ 300 GeV are obtained only for the central five hours of the observing window (T300).

The source underwent a major flare in the first hours of observation, reaching a peak flux of $\sim 9.9 \times 10^{-10} \text{cm}^{-2} \text{s}^{-1}$ (> 400 GeV) at MJD₀ 45.90, corresponding to ~ 11 times the Crab Nebula flux (Aharonian et al. 2006a) above the same threshold. This peak flux is about 20% higher than the peak flux measured during the Big Flare above the same threshold (~ 9.0 Crab, $\sim 8.0 \times 10^{-10} \text{cm}^{-2} \text{s}^{-1}$ > 400 GeV). The main flare seems to occur with nearly symmetrical rise and decay timescales, of the order of one hour. After the peak, the γ -ray flux decreased during the night reaching the minimum around MJD₀ 46.12, but with two other flares of smaller amplitude superimposed: a second outburst around MJD₀ 45.96 with a duration of ~ 20 minutes, and a longer flare or plateau between MJD₀ 46.0 and 46.1, with a duration of 2-3 hours.

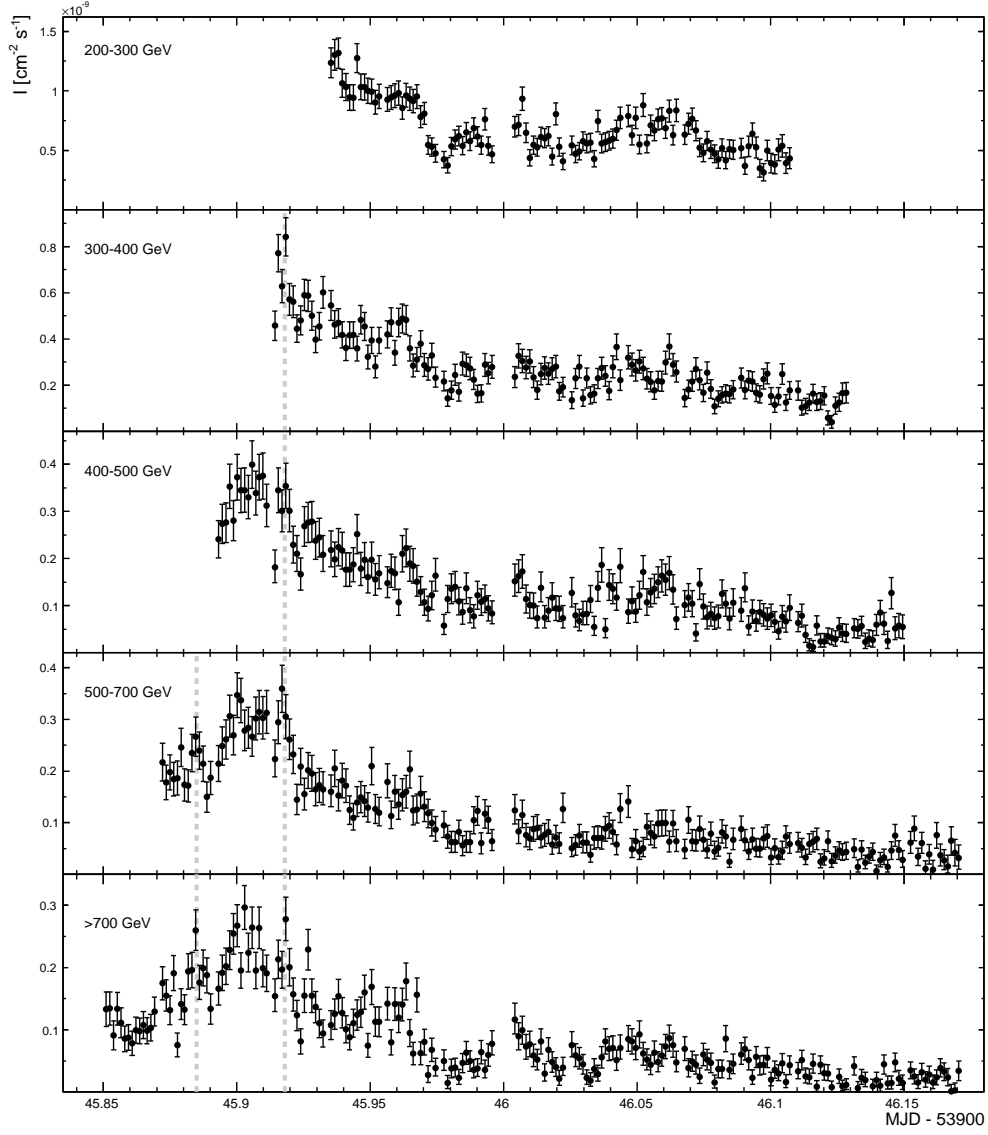


Figure 4.1: Integral flux as a function of time in different energy bands. The time duration of each bin is two minutes. The time windows of each lightcurve and their corresponding labels for future reference are given in table 4.1. The dotted lines mark the positions of fast varying substructures on-top of the main flare (see text).

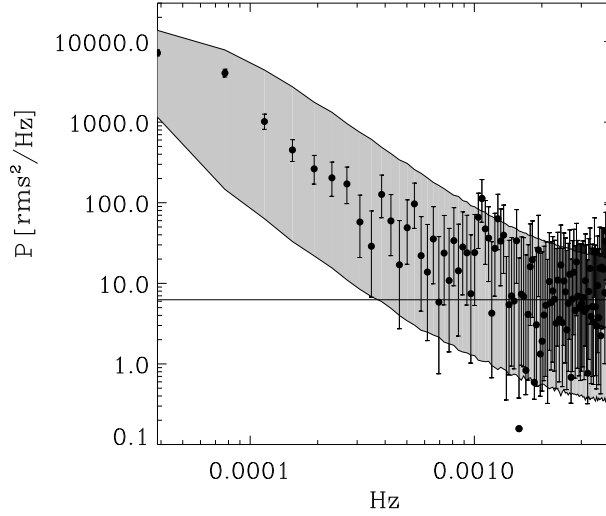


Figure 4.2: Fourier power spectrum of the γ -ray lightcurve above 500 GeV in two minute bins in the T500 period. The gray area corresponds to the 90% confidence interval for a lightcurve with a power-law Fourier spectrum $P_\nu \propto \nu^{-2}$ obtained from simulations. The Fourier analysis was done by Guillaume Dubus, who also provided this figure.

Additionally, two subflares are apparent in all covered energy bands around MJD₀ 45.885 and MJD₀ 45.920 (marked by the dotted lines in figure 4.1). These fast varying structures have a duration of ~ 10 min, similar to ones observed during the Big Flare. However, in comparison to the fast subflares observed on the night of 28 July, they occurred during observations at a higher energy threshold, yielding lower event statistics. The significance of these subflares is therefore limited, and was estimated to 3-4 σ using a Continuous Wavelet Transform (Foster 1996), in a work performed by Andre Claude Clapson. The Fourier power spectrum therefore provides a more robust way to quantify the fastest variability time scales. As a compromise between event statistics and time coverage of the flare, this was done for the lightcurve above an energy threshold of 500 GeV in two minutes time bins. The resulting power spectrum is very similar to the one of the Big Flare and is compatible with a red noise process (see figure 4.2). It shows significant power above the noise level down to time scales of ~ 900 s, slightly higher than the ones observed during the Big Flare (~ 600 s, see section 3.4).

4.1.2 Comparison with X-ray and optical lightcurves

The combined γ -ray, X-ray and optical lightcurves in four minute bins are shown in figure 4.3. The vertical scales in this figure have been adjusted differently for each band, in order to emphasize the specific variability patterns. A significant flaring activity is present in all three bands, but with different amplitudes. In few hours, the γ -ray flux changed by roughly 1.3 orders of magnitude, where the X-ray flux varied only by factor ~ 2 , and the optical flux by less than 15%. The source thus shows a dramatic increase of variability with photon energy. Despite such difference in amplitude, the X-ray and VHE lightcurves are strongly correlated, with the X-ray emission following closely the same pattern traced by the VHE lightcurve (see next section). In the optical band, instead, the flare seems to start simultaneously with the main VHE flare (the chance of coincidence in the observed times span is $< 1\%$, for a 4-min sampling). However, it develops on much longer timescales, reaching the maximum about ~ 2 hours later than at VHE, when both the γ -ray and X-ray fluxes have already strongly decayed, and remaining almost constant thereafter. The optical lightcurve does not correlate at short timescales with the lightcurves in the other two bands,

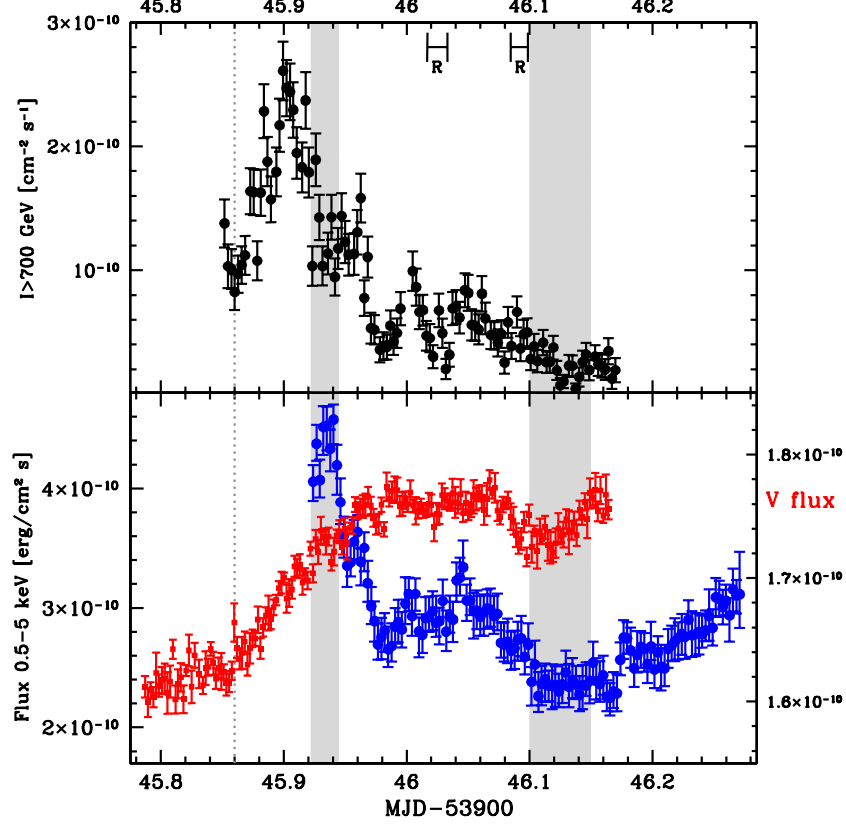


Figure 4.3: Overall lightcurves of PKS 2155-304 in the night of 29-30 July 2006, as seen by H.E.S.S. (T700, *upper panel*), Chandra (lower panel, blue circles) and Bronberg Observatory (optical V band, red squares). Time bins have a duration of 4 minutes. The vertical scales are different in each panel and have been adjusted to highlight the specific variability patterns. The segments on the upper X-axis show the two intervals corresponding to the RXTE exposure (T300-RXTE, large bars labeled with R). *Lower panel*: the left axis gives the integrated 0.5-5 keV flux, the right axis gives the V-band νF_ν flux at the effective frequency 5500 Å; both are in units of $\text{erg cm}^{-2} \text{s}^{-1}$. Both X-ray and optical fluxes are corrected for Galactic extinction ($A_V=0.071$). The shaded area shows the two intervals corresponding highest (T300-SIMMAX) and lowest (T400-SIMMIN) γ -ray states with multi-wavelength coverage. The vertical line marks a visual reference time for the start of both the optical and γ -ray flares.

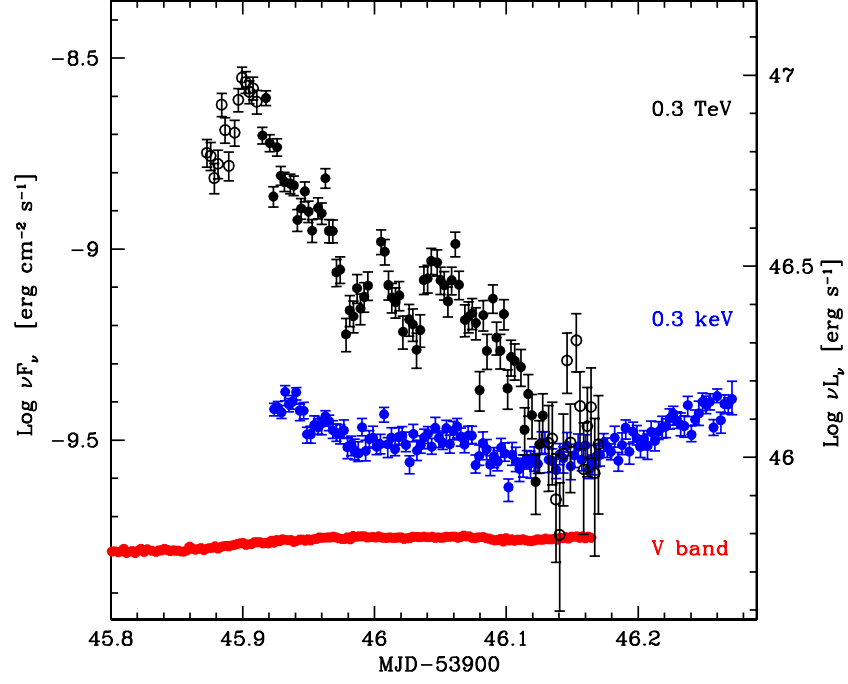


Figure 4.4: Lightcurves of the νF_ν flux at 0.3 TeV (black), 0.3 keV (blue) and 550 nm (red) in 4-minute bins, plotted on the same flux scale. The right axis reports the corresponding luminosity scale. The γ -ray flux is shown for the T500 period and was calculated assuming a power law spectrum with a spectral index of 3.4 (see text). Filled circles are fluxes calculated from the >300 GeV lightcurve; empty circles from the >500 GeV lightcurve extrapolating to the given energy threshold. The VHE fluxes are corrected for extragalactic γ - γ absorption with the minimal EBL model. Using the high EBL model yields fluxes higher by $\sim 35\%$ (~ 0.3 on the Y-axis).

though towards the end of the observation it shows the same pattern and increasing trend displayed by the X-ray lightcurve.

Note that – in contrast to the optical and X-ray band – the γ -ray flux in figure 4.3 is not given in units of energy flux, but in particle flux. The particle flux is directly measured with H.E.S.S.; in order to transform it into an energy flux an energy spectrum needs to be assumed¹. An accurate determination of the energy spectrum is however not possible on these short time-scales (4 minutes), but only on longer time scales (7-14 minutes), as will be discussed later in section 4.2.1. However, anticipating that no strong spectral variability is observed during this night (see section 4.2.1), it is useful to convert the particle flux into an energy flux with the average spectrum of this night, allowing a first qualitative comparison of the energy output between the observed energy bands. Figure 4.4 shows energy flux evolution over time on the same flux scale for all energy ranges in a νF_ν representation. They correspond to slices of the SED at the three energies of 0.3 TeV, 0.3 keV and 2.25 eV. The integral γ -ray fluxes have been deabsorbed for the EBL with the minimal EBL model (see section 1.5). Using the maximal EBL model would increase the fluxes by $\sim 35\%$. Interestingly, the γ -ray flux dominates the energy output during the flare: the energy flux measured at γ -rays is approximately five times higher than the one measured at X-rays. This fact is referred to as *Compton dominance* and will be discussed in more detail in section 4.2.3.

4.1.3 Inter-band time lags

The degree of correlation and possible time lags between different lightcurves have been quantified by means of cross-correlation functions. The correlation analysis was performed both between the hard and soft bands within each passband, and between the X-ray and γ -ray emissions, using the *Discrete Correlation Function* (DCF; Edelson & Krolik (1988)). The DCF for two time series a_i and b_j , with a mean and RMS of \bar{a} and σ_a , and \bar{b} and σ_b respectively, is defined as:

$$\text{DCF}(\tau) = \frac{1}{M} \sum_{i,j} \frac{(a_i - \bar{a})(b_j - \bar{b})}{\sqrt{\sigma_a^2 + \sigma_b^2}}, \quad (4.1)$$

where i and j are summed over all M combinations of values a_i and b_j with a relative time difference between $\tau - \Delta t/2$ and $\tau + \Delta t/2$; Δt is the time binning chosen for the DCF and was always set to the time duration of the bins in the correlated lightcurves. The DCF is specially suited for unevenly spaced data, and the VHE lightcurves have gaps of few minutes every 28 minutes between the stop and start of consecutive runs. The time lags between lightcurves are determined as the maximum of a Gaussian plus linear function fitted to the central peak of the DCF. This procedure is robust against spurious peaks at zero time lag due to correlated errors (Edelson & Krolik 1988).

The error on the measured time lag is determined from simulations. Ten thousand lightcurves were generated by varying each measurement point within its errors, assuming Gaussian probability densities. The entire correlation procedure is redone for each of these simulations, resulting in a Cross Correlation Peak Distribution (CCPD). The RMS of the CCPD then yields an estimate on the statistical error of the measured time lag (Maoz & Netzer (1989); Peterson et al. (1998)). The time binning of the lightcurves and the DCF introduce an additional systematic error. The latter was estimated to 30 s, by comparing the mean value of the time lags measured for artificially injected dispersions in the H.E.S.S. data, on time-scales smaller than the time binning.

At VHE, the analysis was performed on the simultaneous lightcurves between 300-700 GeV and above 700 GeV in two-minute time bins (T300, see figure 4.1). This choice yields a

¹In contrast to the particle flux, the energy flux measurement is more sensitive to the assumed spectral shape (see section 2.2.5). A variation of 0.2 in the photon index of a power law spectrum yields differences of $\sim 10\%$ in energy flux above the observed energy thresholds.

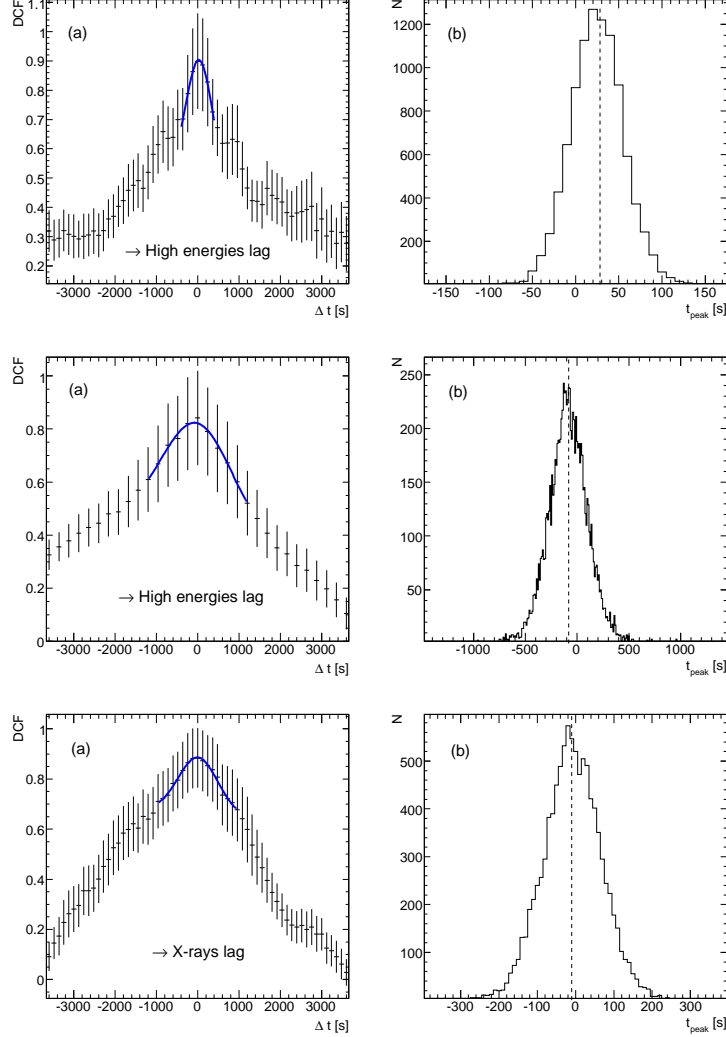


Figure 4.5: Cross-correlation analysis between the hard and soft bands at γ -ray (upper panels) and at X-ray energies (middle panels), and between the X-ray and VHE band (lower panels). *Upper panels:* (a) DCF of the 300-700 GeV and the >700 VHE band in the T300 time window. The blue line shows the best fit Gaussian plus linear function, with a maximum at 28 s. (b) Corresponding Cross Correlation Peak Distribution of 10000 simulated lightcurves. The RMS of the distributions is 30 s. The dotted line marks the position of the maximum in (a). *Middle panels:* same as upper panel, but for the 0.2-1.0 keV and 2.0-6.0 keV X-ray band. The maximum of the DCF is at -82 s and the RMS of the CCPD is 202 s. *Lower panels:* same as the upper panels, but for the VHE lightcurve above 300 GeV and the Chandra 0.2-6 keV band in the simultaneous time window T300-SIM, shown in figure 4.6. The maximum of the DCF is at -10 s and the RMS of the CCPD is 76 s.

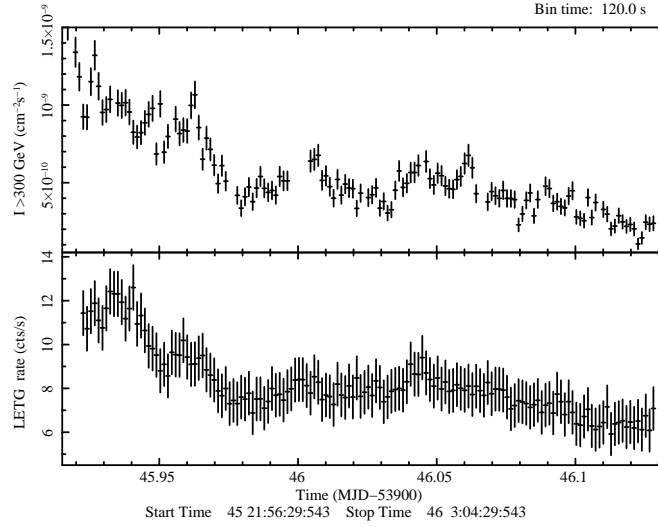


Figure 4.6: H.E.S.S. and Chandra lightcurves in the simultaneous time windows T300-SIM in two-minute time bins. *Upper panel:* integral fluxes above 300 GeV. *Lower panel:* Chandra count rate in the 0.2-6 keV band.

good compromise between event statistics, time coverage and a maximum energy difference between the bands. The resulting time lag between the higher and the lower energy band is $(28 \pm 30_{\text{stat}} \pm 30_{\text{sys}})$ s (see figure 4.5). Since this time lag is not significantly different from zero, a 95% confidence upper limit of 129 s is derived. This value was calculated assuming a Gaussian probability distribution around the measured time lag. The width of the distribution was set to the linear sum of the statistical and systematic error, in order to be conservative. Afterwards symmetric intervals around zero were integrated, until a 95% containment was achieved. In the X-ray passband possible time delays were measured with the same procedure. The Chandra lightcurve was divided in a soft (0.2-1.0 keV) and hard (2.0-6.0 keV) band. Due to the lower count rate, in this case four minute time bins were used. The measured time lag is $(-82 \pm 202_{\text{stat}} \pm 30_{\text{sys}})$ s. This value is again not significantly different from zero, resulting in a 95% upper limit of 482 s.

The cross-correlation analysis between the X-ray and γ -ray emissions was performed on the simultaneous X-ray and γ -ray (T300-SIM) lightcurves with two-minute time bins (figure 4.6), as the best compromise between high overall statistics, time resolution and wide time coverage. The results are shown in the lower panel of figure 4.5. The two emissions are overall highly correlated, with a maximum correlation of $\text{DCF}_{\text{max}} \approx 0.9$, and no significant lag is found. The time delay of the X-rays with respect to the γ -ray is $(10 \pm 76_{\text{stat}} \pm 30_{\text{sys}})$ s. This yields a 95% confidence upper limit for a time lag of 208 s.

4.2 Time-resolved spectral analysis

4.2.1 γ -ray spectra

A search for spectral variations in the VHE data was performed by fitting a power-law spectrum to a fixed energy range in fixed time bins. The high event statistics of this dataset allows the sampling to be done in 7 to 14-minute bins for the part of the night with an energy threshold below 300 GeV (T300). On these short integration times the power-law gives a statistically good description of the data. The result is shown in the left panel of figure 4.7. The spectrum generally hardens with increasing flux, as seen during the Big Flare (see section 3.4) and during the entire 2005 to 2007 campaign (see section 3.3). This can be better appreciated in the correlation plot in the right panel of figure 4.7. The fit to a

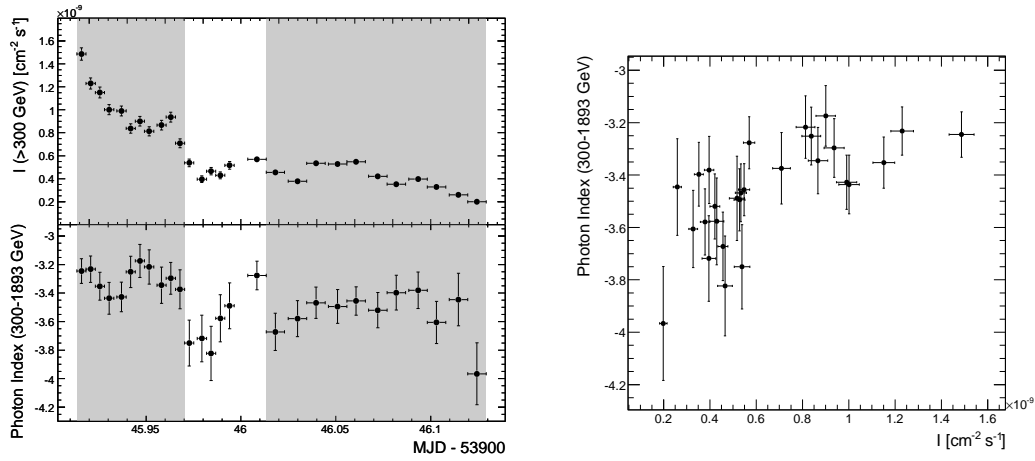


Figure 4.7: *Left panel*: integral flux above 300 GeV and photon index as a function of time. Horizontal error bars show the time interval of each bin, going from 7 to 14 minutes before and after MJD₀ 46.0. The shaded zones mark the two time-intervals corresponding to the average high and low-state spectra fitted in table 4.2 (T300-HIGH and T300-LOW, respectively). *Right panel*: photon index as a function of the integral flux.

constant photon index results in a χ^2 probability of only 1.6%, showing that the hardening is significant. These spectra are also used for comparison with the X-ray spectra extracted in exactly the same time bins, and discussed in section 4.3.

A study of the spectral variations was also performed with an energy threshold of 500 GeV, which allows the sampling of a wider time span and in particular of both the rise and decay phases of the main γ -ray flare (T500). However, the lower event statistics above this threshold requires longer integration times, yielding a lower time resolution. The result is shown in figure 4.8, where spectra have been extracted in 14 and 28 minute bins. The spectral variations follow the same pattern of the 300-GeV spectra, both in time and in the flux-index relation. No significant spectral changes are observed between the rising and decaying part of the flare.

The study of the spectral shape in more detail requires higher event statistics. To achieve this the dataset was divided into similar spectral states, namely a low and a high flux state (T300-LOW and T300-HIGH, see figure 4.7). In addition, spectra were extracted in three other important periods: a) around the peak of the γ -ray emission (T400-PEAK, see figure 4.8); b) in the central five hours characterized by a threshold as low as 200 GeV (T200); c) in the period simultaneous with the RXTE exposure (T300-RXTE), where the X-ray spectrum can be measured over two decades in energy.

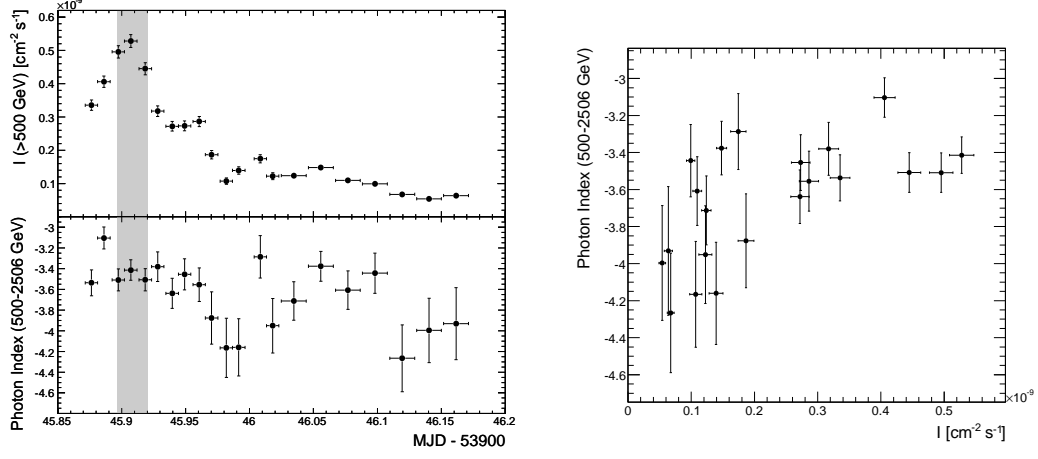


Figure 4.8: *Left panel:* integral flux above 500 GeV and photon index as a function of time. Horizontal error bars show the time interval of each bin, going from 14 minutes at the beginning to 28 minutes towards the end of the night. The shaded area shows the time window of the γ -ray peak spectrum fitted in table 4.2 (T400-PEAK). *Right panel:* photon index as a function of the integral flux.

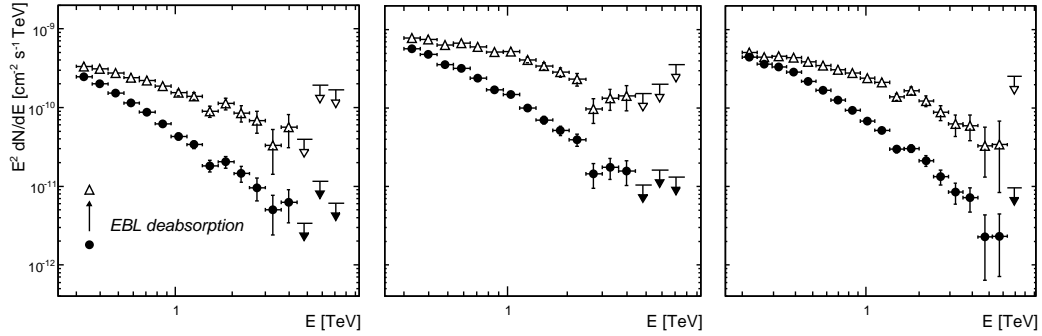


Figure 4.9: Selected γ -ray spectra: average energy spectra above 300 GeV for the T300-Low (left) and T300-HIGH (middle) periods, as shown in figure 4.7, and the average spectrum in T200 above 200 GeV (right). Open symbols correspond to the spectra corrected for EBL absorption with the minimum EBL model. The spectra deabsorbed with the maximum EBL model are not shown for clarity of the figure. The best fit parameters for both models are given in table 4.3.

Table 4.2: Spectral fit of the γ -ray spectra extracted in the following periods: around the VHE maximum (**T400-PEAK**; shaded area in figure 4.8); in the high and low flux state with 300 GeV threshold (**T300-HIGH**, **T300-LOW**; shaded areas in figure 4.7); in the window with a 200 GeV threshold (**T200**; see figure 4.1); in the window simultaneous with the RXTE exposure (**T300-RXTE**; see figure 4.3).

PL fits	Φ_0 $\text{cm}^{-2}\text{s}^{-1}\text{TeV}^{-1}$	Γ			$F_{0.3-3 \text{ TeV}}$ $\text{ergs cm}^{-2} \text{ s}^{-1}$	χ_r^2 (d.o.f.)	P_{χ^2}
T400-PEAK	$2.20 \pm 0.06 \times 10^{-10}$	3.46 ± 0.04	-	-	1.35×10^{-09}	3.66 (11)	3.2×10^{-5}
T300-HIGH	$1.36 \pm 0.03 \times 10^{-10}$	3.36 ± 0.03	-	-	7.88×10^{-10}	4.3 (12)	7.25×10^{-7}
T300-LOW	$4.89 \pm 0.15 \times 10^{-11}$	3.51 ± 0.03	-	-	3.09×10^{-10}	1.36 (12)	0.18
T200	$7.46 \pm 0.12 \times 10^{-11}$	3.25 ± 0.01	-	-	4.06×10^{-10}	16 (16)	0
T300-RXTE	$4.78 \pm 0.30 \times 10^{-11}$	3.53 ± 0.07	-	-	3.07×10^{-10}	1.4 (11)	0.166
Log-parabolic	Φ_0	Γ	b	E_{peak} (TeV)	$F_{0.3-3 \text{ TeV}}$	χ_r^2 (d.o.f.)	P_{χ^2}
T400-PEAK	$2.55 \pm 0.09 \times 10^{-10}$	3.54 ± 0.06	1.05 ± 0.20	0.19	1.25×10^{-09}	0.368 (10)	0.961
T300-HIGH	$1.46 \pm 0.04 \times 10^{-10}$	3.53 ± 0.05	0.62 ± 0.11	0.056	7.94×10^{-10}	1.35 (11)	0.188
T300-LOW	$4.98 \pm 0.16 \times 10^{-11}$	3.66 ± 0.07	0.41 ± 0.16	0.011	3.08×10^{-10}	0.759 (11)	0.682
T200	$7.51 \pm 0.16 \times 10^{-11}$	3.69 ± 0.05	0.78 ± 0.07	0.084	4.29×10^{-10}	2.39 (15)	0.0019
Broken PL	Φ_0	Γ_1	Γ_2	E_{break} (TeV)	$F_{0.3-3 \text{ TeV}}$	χ_r^2 (d.o.f.)	P_{χ^2}
T200	$1.46 \pm 0.10 \times 10^{-10}$	2.73 ± 0.05	3.60 ± 0.04	0.42 ± 0.02	4.31×10^{-10}	1.44 (14)	0.124

Table 4.3: Spectral fit of the same γ -ray spectra given in table 4.2, but corrected for EBL absorption. The fit values are given for the minimum EBL model. The one sided error for each fit-parameter shows the difference to the result obtained for the maximum EBL model. The statistical errors and chi-square probabilities are almost independent of the choice of EBL model.

PL fits	Φ_0 $\text{cm}^{-2}\text{s}^{-1}\text{TeV}^{-1}$	Γ			$F_{0.3-3 \text{ TeV}}$ $\text{ergs cm}^{-2} \text{ s}^{-1}$	χ_r^2 (d.o.f.)	P_{χ^2}
T400-PEAK	$7.18 \pm 0.19 + 3.02 \times 10^{-10}$	$2.66 \pm 0.04 + 0.24$	-	-	$3.01 + 1.00 \times 10^{-9}$	5.13 (11)	4.14×10^{-8}
T300-HIGH	$4.45 \pm 0.10 + 1.88 \times 10^{-10}$	$2.57 \pm 0.03 + 0.24$	-	-	$1.81 + 0.63 \times 10^{-9}$	4.95 (12)	2.92×10^{-8}
T300-LOW	$1.62 \pm 0.05 + 0.69 \times 10^{-10}$	$2.70 \pm 0.04 + 0.24$	-	-	$6.88 + 2.27 \times 10^{-10}$	1.13 (12)	0.326
T200	$2.41 \pm 0.04 + 1.01 \times 10^{-10}$	$2.53 \pm 0.01 + 0.21$	-	-	$9.74 + 3.36 \times 10^{-10}$	7.88 (16)	0
T300-RXTE	$1.59 \pm 0.10 + 0.69 \times 10^{-10}$	$2.72 \pm 0.07 + 0.24$	-	-	$6.84 + 2.25 \times 10^{-10}$	1.17 (11)	0.305
Log-parabolic	Φ_0	Γ	b	E_{peak} (TeV)	$F_{0.3-3 \text{ TeV}}$	χ_r^2 (d.o.f.)	P_{χ^2}
T400-PEAK	$8.67 \pm 0.30 + 3.83 \times 10^{-10}$	$2.73 \pm 0.06 + 0.25$	$1.23 \pm 0.20 - 0.06$	0.51 ± 0.14	$2.9 + 1.00 \times 10^{-9}$	0.393 (10)	0.951
T300-HIGH	$4.82 \pm 0.13 + 2.08 \times 10^{-10}$	$2.73 \pm 0.05 + 0.25$	$0.613 \pm 0.11 - 0.003$	0.26 ± 0.15	$1.82 + 0.61 \times 10^{-9}$	1.79 (11)	0.0493
T300-LOW	$1.66 \pm 0.05 + 0.72 \times 10^{-10}$	$2.83 \pm 0.07 + 0.25$	$0.376 \pm 0.14 + 0.01$	0.08 ± 0.08	$6.81 + 2.20 \times 10^{-10}$	0.508 (11)	0.899
T200	$2.44 \pm 0.01 + 1.03 \times 10^{-10}$	$2.79 \pm 0.04 + 0.26$	$0.484 \pm 0.06 + 0.08$	0.15 ± 0.07	$9.67 + 3.23 \times 10^{-10}$	1.76 (15)	0.0346

The results of the spectral fits are given in table 4.2, with a selection shown in figure 4.9. The spectra present a significant curvature with respect to the pure power-law. The χ^2 probabilities show that the latter is completely excluded in the high states, and is unlikely in the low state. The spectral curvature is generally well described by a log-parabolic function. Most remarkably, the latter model shows that the curvature of the spectrum is strongly variable with time. In particular, the curvature is more pronounced (i.e. b is higher) in the brightest state and decreases as the source dims. This is a direct proof that the curvature of the γ -ray spectrum in PKS 2155-304 also has an intrinsic origin, and cannot be produced entirely by γ - γ absorption on the EBL or on any local or external field which is constant on the observed timescales.

Besides providing the widest energy coverage, the γ -ray spectrum above 200 GeV measured in the central five hours also allows a direct comparison with the time-averaged spectrum of the Big Flare, which was measured above the same energy threshold. Interestingly, the fit of a broken power law yields almost identical results for both nights, with a break energy of ~ 420 GeV and a spectral softening of $\Delta\Gamma \simeq 0.9$ (see table 4.2 and section 3.4). This shows that the source was in a similar state, even though the overall average normalization is about $\sim 30\%$ lower than during the Big Flare for this part of the night.

Absorption-corrected γ -ray spectra

The results of the fits on the intrinsic spectra are provided in table 4.3. even after correction for the steepening induced by EBL absorption, the γ -ray spectra show clear evidence of curvature, and the power-law model is excluded with high confidence for all states but the T300-RXTE period (which has the lowest exposure of 44 minutes). The spectral curvature is well described by the log-parabolic function for all spectra including the > 200 GeV dataset.

The comparison of the curvatures among different states and between the synchrotron and Inverse Compton (IC) components can also provide important clues on the source emission regime (Thomson or Klein-Nishina, see section 1.4.1) and the acceleration mechanisms (Massaro et al. 2006). As one can see by comparison of the spectra in the three different flux states (T400-PEAK, T300-HIGH and T300-LOW in table 4.3), the curvature changes significantly along the night and so does the Compton peak energy. Quite interestingly, a clear trend emerges: both the curvature parameter b and E_{peak} increase with the γ -ray flux. At the maximum of the γ -ray flare the spectrum is strongly curved for the spectra deabsorbed with the minimal EBL level ($b = 1.23 \pm 0.2$), with the Compton peak estimate at $E_{\text{peak}} = 510$ GeV. As during the Big Flare, this value is significantly higher than the average value found between 2005 to 2007 (70-90 GeV, see section 3.3). As the flux decreases, the curvature flattens ($b = 0.61$ to 0.38), while the IC component peak shifts to lower energies ($E_{\text{peak}} = 260$ GeV to $E_{\text{peak}} = 80$ GeV, respectively), reaching again its average value.

Deabsorbing the energy spectra with the maximal EBL model does not substantially change these results: it yields similar curvatures ($b=1.43$, 0.72 and 0.51 , for T400-PEAK, T300-HIGH and T300-LOW) and slightly higher IC peak energies ($E_{\text{peak}} = 650$, 410 and 160 GeV, respectively). It is important to recall that the absolute value of the curvature b depends on the particular choice of the EBL spectrum used, but not the trend itself. This trend is opposite to what is generally observed and expected for the synchrotron emission in TeV blazars. For example, in Mkn 421 the curvature b decreases as both E_{peak} and the flux increase (Massaro et al. 2004). It is also interesting to note that the spectral index Γ does not correlate (and possibly anti-correlate) with the curvature b , contrary to what is observed in the X-ray band for this (see next section) and other High Frequency Peaked BL Lacs (HBL) (Massaro et al. 2004).

4.2.2 X-ray spectra

In order to study the properties and time-evolution of the X-ray spectrum and its correlation with the γ -ray emission, the Chandra spectra were extracted both through a uniform

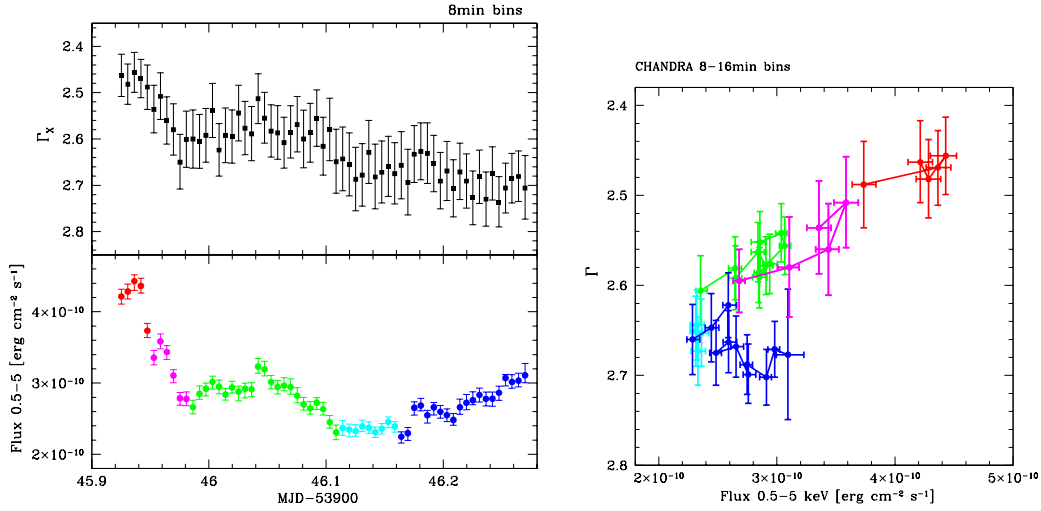


Figure 4.10: Evolution of the X-ray spectrum with time, for the whole Chandra exposure. *Upper left panel:* spectral indices measured in 8-min bins with a single power-law fit model plus galactic absorption. The H.E.S.S. window ends at $\text{MJD}_0=46.16$. *Lower left panel:* energy flux as a function of time. The colors (in time sequence: red, magenta, green, cyan, blue) mark the different zones for the spectrum-flux correlation, shown in the right panel. *Right panel:* spectral index as a function of flux. For better visibility, the cyan and blue intervals are further binned in 16-minutes spectra. There is a clear “higher when brighter” trend in the decaying phase of the first branch (corresponding to the VHE window). The behaviour changes however in the new rising phase: the X-ray spectrum continues to soften while the flux increases, drawing a counter-clockwise pattern.

sampling of the whole exposure, and strictly coincident with the γ -ray time bins. The spectra were all fitted using an equivalent hydrogen column density fixed at Galactic values ($1.69 \times 10^{20} \text{cm}^{-2}$; Dickey & Lockman 1990) with different source models. On short integration times (< 1 hr), a single power-law model provides statistically good fits for all datasets, while evidence for curvature is found only when larger exposures are considered or a wider energy band is available (for example including the RXTE data).

The time evolution of the X-ray spectrum along the whole Chandra pointing – which extends few hours beyond the end of the H.E.S.S. observation – is shown in Figure 4.10. There is a clear trend of “harder when brighter” behaviour in the first part of the dataset, corresponding to the decaying phase of the main γ -ray flare. This behaviour is followed also by the small-amplitude flares, whose paths in the flux–index plane overlap tightly with the overall trend of the decaying phase (figure 4.10 right).

However, the relation changes in the last part of the observation ($\text{MJD}_0 > 46.16$): while the X-ray flux starts to increase again, the spectral index continues to soften. This “softer when brighter” behaviour in the rising phase of a new flare reveals a change of conditions for the emitting region. It is indicative of a slow acceleration/injection process, whose timescale is comparable with the other timescales of the system ($t_{\text{acc}} \approx t_{\text{cool}}$). The information on the flare propagates then from lower to higher energies as particles are gradually accelerated (Kirk et al. 1998; Ravasio et al. 2004). Quite remarkably, this seems also confirmed by the optical data, which in fact show an increasing trend just before the X-ray rising.

Figure 4.11 shows the spectra of the total Chandra exposure and of the RXTE simultaneous window (T300-RXTE). The results of the spectral fits performed on the datasets simultaneous to the VHE intervals of table 4.3 are given in table 4.4. All dataset are strictly simultaneous except for the T300-HIGH spectra, for which the X-ray window does not include the first ~ 10 minutes of the 1.3-hrs VHE window above 300 GeV. Since there are no

significant spectral changes at VHE in that window, the γ -ray spectrum can be considered to accurately represent the spectral shape in the X-ray window.

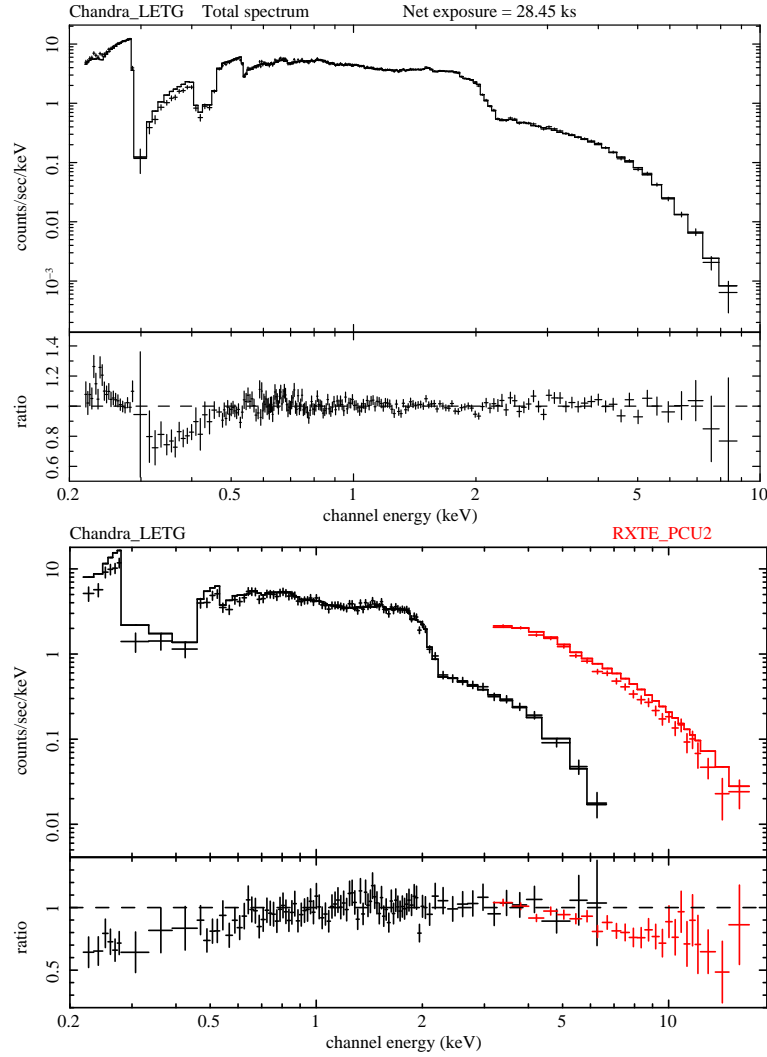


Figure 4.11: *Upper panel:* Chandra spectrum for the total exposure, fitted with a broken power-law plus galactic column density. The additional absorption feature in the 0.3-0.4 keV range is due to the contaminants on the ACIS optical blocking filter, not yet fully accounted by the calibration. It can be accounted for with a simple edge model at 0.31 keV and $\tau_{\text{max}}=0.4$ (see text). *Lower panel:* the simultaneous Chandra+RXTE spectrum in the common 44-min window (T300-RXTE). The plot corresponds to a single power-law with galactic absorption, and the data/model ratio shows the clear evidence of curvature (fit parameters are given in table 4.4). The RXTE/Chandra normalization is fixed at 1.08, as derived from the fit in the overlapping energy range (3-7 keV).

Table 4.4: Fit results of the time-averaged X-ray spectra measured by Chandra in different time windows. The fits in the T300-RXTE window were performed on the simultaneous data taken from Chandra and RXTE (see figure 4.11).

Broken-PL fits	Band keV	Γ_1	E_{break} keV	Γ_2	$F_{0.5-5 \text{ keV}}$ ergs cm $^{-2}$ s $^{-1}$	$F_{2-10 \text{ keV}}$	$\chi_r^2/\text{d.o.f.}$
T300-HIGH (Chandra)	0.2-8	2.35 ± 0.03	1.00 ± 0.07	2.60 ± 0.02	3.88×10^{-10}	1.45×10^{-10}	0.65/204
T300-LOW (Chandra)	0.2-8	2.41 ± 0.02	0.95 ± 0.06	2.71 ± 0.02	2.78×10^{-10}	9.19×10^{-11}	0.74/204
T200 (Chandra)	0.2-9	2.39 ± 0.01	0.95 ± 0.04	2.68 ± 0.01	3.05×10^{-10}	1.05×10^{-10}	0.87/204
T300-RXTE (Chandra + RXTE)	0.2-20	2.56 ± 0.02	2.72 ± 0.22	2.98 ± 0.04	2.79×10^{-10}	9.11×10^{-11}	0.69/117
Log-parabolic fits	Band	Γ	b	$E_{\text{peak}}(\text{eV})$	$F_{0.5-5 \text{ keV}}$	$F_{2-10 \text{ keV}}$	$\chi_r^2/\text{d.o.f.}$
300-HIGH (Chandra)	0.2-8	2.48 ± 0.01	0.18 ± 0.03	46	3.88×10^{-10}	1.41×10^{-10}	0.69/205
300-LOW (Chandra)	0.2-8	2.57 ± 0.01	0.21 ± 0.02	44	2.77×10^{-10}	8.89×10^{-11}	0.83/205
T200 (Chandra)	0.2-9	2.55 ± 0.01	0.21 ± 0.01	49	3.05×10^{-10}	1.01×10^{-10}	1.02/205
T300-RXTE (Chandra + RXTE)	0.2-20	2.56 ± 0.01	0.25 ± 0.02	76	2.81×10^{-10}	8.92×10^{-11}	0.60/118

For all spectra in table 4.4 there is clear evidence of curvature. The spectra show a continuous steepening towards higher energies up to ~ 20 keV, which is well represented by both a broken power-law and log-parabolic models. All spectra have a convex shape and no signs of flattening at high energies, as recently reported from XMM observations in November 2006 (Foschini et al. 2008; Zhang 2008). This means that the peak of the synchrotron emission has not entered at any time the observed energy range, and that there is no sign of a different spectral component emerging at high energies.

It is very interesting to compare the curvature parameters and SED peak location given by the log-parabolic fits. Both the spectral index and the curvature increases (slightly) as the flux decreases. This is also corroborated by the fits of spectra extracted in even shorter intervals at the two extremes of the X-ray flux range (T300-SIMMAX and T400-SIMMIN, see figure 4.4). The log-parabolic fit yields $\Gamma = 2.45 \pm 0.02$ and $b = 0.16 \pm 0.04$ vs. $\Gamma = 2.64 \pm 0.01$ and $b = 0.24 \pm 0.04$, respectively, for an integrated flux $F_{0.5-5} = 4.33$ and 1.65×10^{-10} ergs $\text{cm}^{-2} \text{s}^{-1}$. The change of the two spectral parameters, however, is such that the estimate of the location of the SED peak remains basically constant: for all spectra, the synchrotron E_{peak} falls within the range 44-76 eV. Contrary to what is observed in γ -rays, in the X-ray band the photon index shows a positive correlation with the curvature b , as observed for example in Mkn 421 (Massaro et al. 2004). The absolute values of the curvature are similar to those found in most of the other HBL (Massaro et al. 2008).

4.2.3 Spectral Energy Distributions

To highlight the evolution of the SED along the night, two strictly simultaneous X-ray and γ -ray spectra are shown in figure 4.12. The two SED snapshots correspond to the brightest/hardest γ -ray state (T300-SIMMAX), and to the faintest/softest γ -ray state (T400-SIMMIN). In addition to these pairs, figure 4.12 shows also the spectrum extracted around the maximum of the γ -ray flare (T400-PEAK). This spectrum unfortunately lacks X-ray coverage (the Chandra pointing started few minutes later), but it corresponds to the brightest γ -ray emission ever recorded from PKS 2155-304. For reference, a selection of historical observations is also plotted, in particular the data from the first X-ray/TeV multi-wavelength campaign performed on PKS 2155-203 in October 2003 (Aharonian et al. 2005b). These data (obtained with RXTE and H.E.S.S.) correspond to one of the historically lowest fluxes ever observed at VHE from this object.

In the optical band, PKS 2155-304 is always dominated by the jet emission (see e.g. Dolcini et al. 2007). The historical lightcurves from long-term photometric monitoring in the V band show variations in the range 12.3-13.9 magnitudes (Carini & Miller 1992; Osterman et al. 2007). During this night, the optical flux is very high but still far from the highest fluxes observed from this object. In the X-ray band, instead, the flux is close to the highest state observed historically, as measured by RXTE-PCA in 1996 ($F_{2-10} \sim 1.6 \times 10^{-10}$ ergs $\text{cm}^{-2} \text{s}^{-1}$, Urry et al. 1999). PKS 2155-304 is observed frequently in the X-ray band, since it is a calibration and monitoring source for XMM, Chandra and SWIFT, but was never found at the level observed during this night, in the 2-10 keV band (see e.g. Donato et al. 2001; Massaro et al. 2008). Quite interestingly, the Chandra spectrum in the highest state seems also to connect smoothly with the flux and spectrum measured by RXTE-HEXTE in 1996 (Urry et al. 1999, butterfly in figure 4.12). Comparing the 2003 with 2006 (low-state) data, the overall brightening in the X-ray (2-10 keV) and VHE (>300 GeV) bands is similar ($2.7 \times$ and $5 \times$, respectively), and corresponds to a relation $F_{\gamma} \propto F_{\text{x}}^{1.6}$ between the two periods.

Compton Dominance

One of the most striking characteristics of the SED is the high Compton dominance during the flare, meaning the high ratio between the IC to synchrotron luminosity ($L_{\text{C}}/L_{\text{S}}$). While it can be up to 100 in powerful Flat Spectrum Radio Quasars, boosted by the IC emission on the intense external photon fields from the disk and the Broad Line Region (Sikora et al.

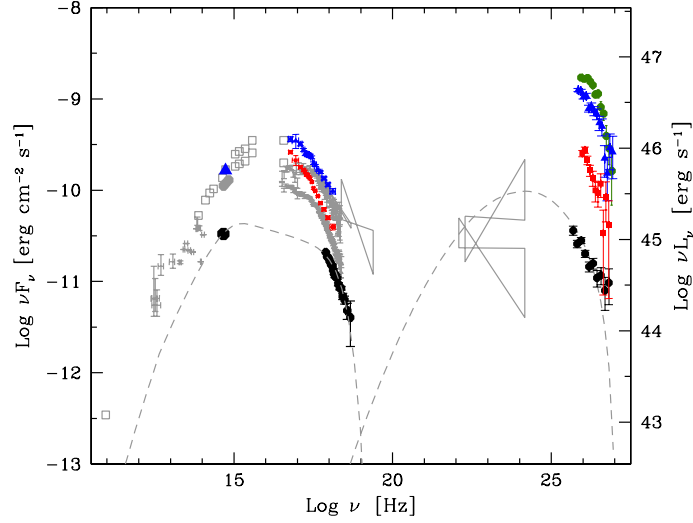


Figure 4.12: Spectral Energy Distributions during the highest (blue triangles; T300-SIMMAX) and lowest (red squares; T400-SIMMIN) flux states during the simultaneous H.E.S.S./Chandra observation. The γ -ray spectrum at the maximum of the γ -ray flare is also plotted (green circles; T400-PEAK). All VHE data are corrected for EBL absorption with the minimal EBL model. For reference the measurements of the RXTE/H.E.S.S. multi-wavelength campaign in 2003 are also shown (black circles), together with the derived SSC model (dashed line; from Aharonian et al. (2005b)). Gray points show other historical data, for references see Chiappetti et al. (1999) and Aharonian et al. (2005b).

1994; Ghisellini et al. 1998), so far it has been of the order of unity or less in HBL. During this event, instead, PKS 2155-304 is strongly Compton dominated, as evident from figure 4.12. The time evolution of the νF_ν fluxes close to the SED peaks is provided by figure 4.4. As one can see, the L_C/L_S ratio is of the order of 3-6 depending on the EBL normalization, but is rapidly variable – on the same timescales of the flux variations – and it decreases to the usual values of $\lesssim 1$ in few hours.

The Compton dominance at the peak of the SED can be estimated from the log-parabolic fit, under the assumption that the curvature of the spectrum remains the same outside of the observed energy band. For the spectra measured in the T300-SIMMAX window one obtains $L_C/L_S \sim 2.5-5$, depending on the EBL normalization. The slightly lower values are due to the fact that the estimate of the synchrotron peak energy (~ 50 eV) locates the X-ray band farther away from the synchrotron peak than the VHE band is from the Compton peak (~ 200 GeV). This is the first time that such high L_C/L_S ratios are observed in an HBL, irrespective of the amount of the intergalactic EBL absorption. So far, high Compton dominance in HBL were obtained only in presence of a high level of the EBL (Aharonian et al. 2002, 2006b), now considered very unlikely.

4.3 X-ray vs. γ -ray correlations

The exceptional γ -ray brightness achieved in this night, coupled with the sensitivity of the H.E.S.S. array and the continuous coverage provided by Chandra, enable one to compare the emission in the two bands with unprecedented detail and time resolution also in the spectral domain.

Figure 4.13 shows the simultaneous flux and spectral properties in the γ -ray and X-ray bands measured in 7 and 14 minute time bins during the central six hours of the night (T300-SIM). In this window, the γ -ray spectra can be measured with an energy threshold

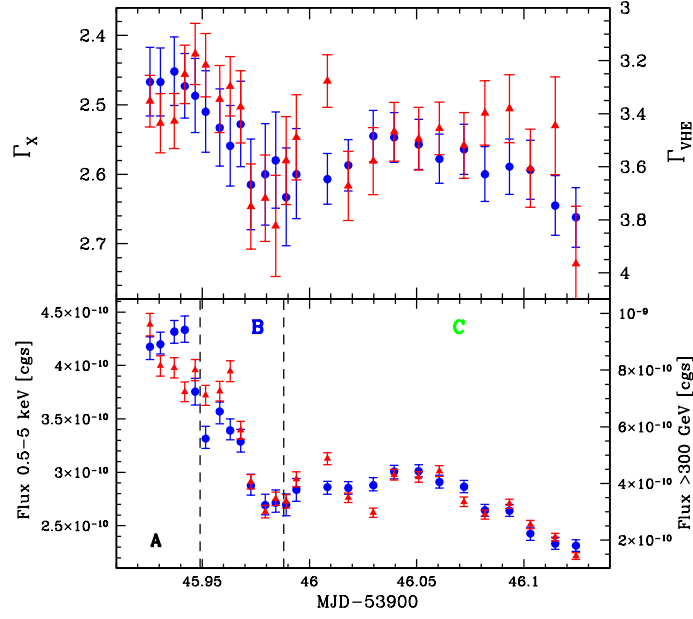


Figure 4.13: Plot of the simultaneous spectral and flux variability in the X-ray (blue circles) and VHE (red triangles) bands. The spectra have been extracted in exactly the same time-bins, with integration times of 7 and 14 minutes (before and after MJD₀ 46.0, respectively). The vertical scales are different (left: X-ray values; right: VHE values) to highlight the variability patterns. *Upper panel:* the scale of the VHE photon indices is $2.6\times$ the X-ray scale. The VHE indices refer to the observed spectra; the corresponding values after correction for EBL absorption with the minimal EBL model can be obtained as $\Gamma_{VHE} - 0.6$. *Lower panel:* integrated energy fluxes in the same units of $\text{erg cm}^{-2} \text{s}^{-1}$. The range of the VHE scale ($15.3\times$) is the cube of the X-ray range ($2.5\times$). The vertical lines mark the three time-zones (A, B and C) referred to in the text and in figure 4.14.

as low as 300 GeV, thus allowing the spectra to be well constrained (± 0.1 in spectral index) over approximately a decade in energy (0.3-2 TeV). The different binning is chosen to achieve comparable signal to noise ratios along the night, and as a good compromise between spectral determination at VHE and time resolution (see section 4.1). Both X-ray and γ -ray spectra have been extracted in exactly the same time bins. The spectra are fitted with a single power-law model, which provides a good fit to the data in each time bin. The integrated energy fluxes are calculated using the specific spectral value measured in each bin.

Two general properties can immediately be noted. The first is that the VHE emission shows a definite correlation with the X-ray emission not only in flux but also spectrally. The spectral evolution follows the same overall pattern in the two bands, though with different amplitudes. The correlation coefficient between the X-ray and γ -ray spectra is $r = 0.65$, with a probability $P < 0.1\%$ of a chance correlation.

The second property, as previously illustrated by figure 4.4, is that the source shows amplitude variations much larger in γ -rays than in X-rays. This is now evident also for the spectra, though not as dramatically as for the flux: the spectral variation at γ -ray is about three times the variations in the X-ray band ($\Delta\Gamma_{VHE} \approx 0.65$ vs $\Delta\Gamma_X \approx 0.21$). In fact, for both panels of figure 4.13 different vertical scales had to be used in order to highlight the similarity of the variability patterns. The combination of such large-amplitude variability at VHE with correlated but small-amplitude variations in X-rays yields perhaps the most important feature of this dataset: the γ -ray flux *varies more than quadratically* with respect to the X-ray flux *during a decaying phase*.

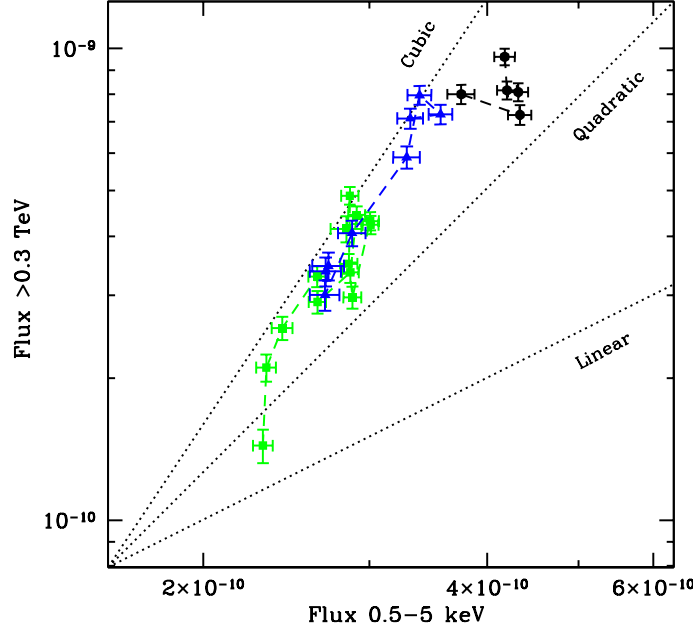


Figure 4.14: Plot of the γ -ray vs X-ray flux correlation, in a log-log diagram and units of $\text{erg cm}^{-2} \text{s}^{-1}$. Different markers correspond to the 3 different intervals shown in figure 4.13: A (black circles), B (blue triangles) and C (green square). For visual reference, the dotted lines show three different slopes of the relation $F_\gamma \propto F_x^\beta$. For better visibility, the Y-scale corresponds to the square of the X-scale, so that a quadratic relation has the slope of one. The best-fit values are given in table 4.5.

Cubic relation between X-ray and TeV fluxes

Figure 4.14 shows the γ -ray flux as a function of the X-ray flux, in a log-log diagram. The data are divided in three subsets (“A”, “B” and “C”) corresponding to three characteristic periods: zone “A” covers the first 35 minutes of the simultaneous window; zone “B” corresponds to the full rise and decay phases of the small-amplitude flare at MJD₀ 45.96; zone “C” covers the rest of the dataset, corresponding to the broader flare (see figure 4.13).

The data are then fitted with a linear relationship in the log-log space ($F_\gamma \propto F_x^\beta$), for the total dataset and in each subset separately. The results are reported in table 4.5, together with the fits of the same datasets with a finer sampling (4-minute bins). The γ -ray flux traces the variations of the X-ray flux much more than quadratically, namely as $F_\gamma \propto F_x^{\sim 3}$. With the exception of the first minutes of zone A, all points lie on a narrow path, also during the small flare on MJD₀ 45.96 (zone B). In zone A, on the other hand, the two emissions do not seem to correlate. The lack of correlation relies only on a few points and is not very significant; however, one may speculate if this is due to small subflares in the VHE domain, which are not mirrored in X-rays. Such subflares have recently been predicted by Ghisellini et al. (2008) and are present in zone A with low significance around MJD₀ = 45.925, as can be seen in figure 4.6. In the periods B and C, instead, the cubic correlation is obtained both considering the two zones separately and together, for which an even steeper slope of $\beta = 3.35$ is obtained. This cubic correlation is robust with respect to the inclusion or exclusion of single data points, and in particular does not depend on the lowest γ -ray point.

The flux-flux correlation is plotted using the same units for both X-ray and VHE bands, namely the integrated energy fluxes. Compared to previous studies, which used simply the observed event rates, the approach presented here is more consistent, and it is justified by the good spectral determination in each time bin. However, the measured relation does not depend significantly on the particular approach used (see discussion in Fossati et al. 2008):

Table 4.5: Values of the slope β of the correlation $F_\gamma \propto F_x^\beta$. Fluxes are integrated over each respective energy band (0.5-5 keV and 0.3-3 TeV) and in strictly simultaneous bins. The parameter is shown for fits performed with two different binnings (4 and 7-14 minutes) and over three different intervals, as shown in figure 4.13.

Datasets	4-min bins	7-14min bins
all	2.21 ± 0.05	2.25 ± 0.05
A	no corr.	no corr
B	2.72 ± 0.17	3.18 ± 0.18
C	2.83 ± 0.17	3.14 ± 0.18
B+C	3.13 ± 0.11	3.35 ± 0.11

a cubic relation is also obtained by using the event rates, both in the VHE band (as photons $\text{cm}^{-2} \text{s}^{-1}$) and in the X-ray band.

As can be seen in table 4.5, the correlation found in the total dataset is less steep than in each subset, while in the B+C zone it is steeper than in B and C taken separately. This is the result of a possible drift of the barycenters of the flux-flux paths among different periods. While individual paths still obey to a specific steep trend, taken together they can produce a flatter (or steeper) envelope. This effect was indeed observed in Mkn 421 (Fossati et al. 2008), considering data from different days.

A cubic relation between the γ -ray and X-ray fluxes during the decaying phase of a flare is quite striking because it cannot be explained in a SSC model, even by a source in the Thomson regime (see section 1.4.1). It is the first time that such a steep slope is observed in the history of the X-ray/TeV correlation studies, though indication for a super-quadratic relation has been recently reported for Mkn 421 (Fossati et al. 2008), during single flares.

So far, these correlations have been studied mainly with the RXTE instrument, which samples higher energies than those observed here. If the spectrum changes with the flux, and with a “harder-when-brighter” behaviour like in this case, the amplitude of the variations changes with energy, and thus the slope of the correlation can depend on the observed band. To quantify this effect, the flux-flux relation has also been investigated by extrapolating the Chandra spectrum in the RXTE band (namely, integrating the best-fit model in the 3-15 keV range), and dividing the VHE range in soft and hard bands (0.3-0.7 and >0.7 TeV, respectively). The result that the same cubic correlation observed in Chandra and H.E.S.S. translates to a quadratic relation (in fact very similar to what observed in Mkn 421) between the hard X-ray and soft VHE bands. This would probably be the result of observations with RXTE and a Cherenkov telescope mostly sensitive to soft γ -ray photons as MAGIC (see section 2.1.1). On the other hand, an even steeper slope ($\beta > 4$) is obtained between the soft X-ray band and hard VHE band.

4.4 Summary of the main observational facts

Before discussing the implications in the context of blazar physics, it is useful to first summarize the main observational findings of this exceptional, complex and phenomenologically rich dataset.

- Large-amplitude γ -ray flux variations are observed, in the presence of smaller X-ray and optical changes: in the course of a few hours, the γ -ray flux changes by ~ 1.3 orders of magnitude, reaching a luminosity of $\approx 10^{47}$ erg/s, while the X-ray flux varies only by a factor overall, and the optical V flux by less than 15%.
- The X-ray and γ -ray emissions correlate strongly, with no evidence of time lags (with a 95% upper limit of ~ 3 minutes for the overall lightcurve). No lags are found in either

passband between the hard and soft energies.

- The optical lightcurve shows a flare which starts simultaneously with the γ -ray flare, but develops on much longer timescales. The optical emission does not correlate at short timescales, reaching the maximum ~ 2 hours later than the γ -ray peak, and remaining almost constant thereafter.
- When correlated, the γ -ray flux decreases as the cube of the X-ray flux ($F_\gamma \propto F_x^{\sim 3}$). This cubic relation holds both during the overall decaying phase and considering shorter intervals separately.
- The X-ray and γ -ray (> 300 GeV) spectral indices correlate as well, following similar patterns in their time evolution, but again with different amplitudes. The VHE variations ($\Delta\Gamma_{\text{VHE}} = 0.65$) are wider by a factor of three than those in the X-ray band ($\Delta\Gamma_X = 0.21$).
- The γ -ray spectra are significantly curved, and the curvature changes with time, in correlation with the flux state: the higher the flux, the more curved the spectrum.
- X-ray and γ -ray spectra show a similar “harder when brighter” behaviour in the simultaneous window. The X-ray data alone sample the start of another flare characterized by instead a “softer when brighter” behaviour at the end of the night.
- The synchrotron peak frequency is estimated to be close to its historical value of ≈ 50 eV, without significant variations throughout the night. The peak of the IC component instead, is estimated to be at $\approx 510 - 650$ GeV at the maximum of the flare, shifting towards to $\approx 80 - 160$ GeV at the end of the night.
- A large Compton dominance ($L_C/L_S \sim 3-6$) was observed during the flare maximum. This is the first time such a high Compton dominance has been seen in an HBL.

4.5 Discussion

The results obtained from this campaign apparently pose a dilemma for blazar emission models, since they seem to both corroborate and challenge the one-zone SSC interpretation. On the one hand, the strong correlation between variations in the X-ray and VHE bands – the emissions follow the same variability patterns both in flux and spectrum, and without apparent lags – do indicate that the same particle distribution, in the same physical region, is likely responsible for the activity in both energy bands. The simultaneity of the occurrence of the optical and VHE flares also suggests that the emission in all three bands correspond to the same flaring event. On the other hand, the cubic relation during the decaying phase cannot be accounted for in a one-zone SSC scenario (see section 1.4.1). A further ingredient is therefore needed to explain this observation.

Two-SED scenario

A simple and realistic solution is provided by the superposition of two SED components, produced by two different emission regions. The first region is responsible for the usual “persistent” SED of PKS 2155-304 and has energy fluxes F_γ^p and F_x^p in the γ -ray and X-ray domain, respectively; its flux varies on time scales which are longer than the ones in question during this flare. The second “flaring” region has fluxes F_γ^f and F_x^f in the same energy bands; it is responsible for the dramatic flaring activity of this night and most likely of all the active period of July 2006. The flaring zone needs to be much more compact and with higher bulk motion compared to the persistent region to account for the much faster variability timescales. This flaring region might in fact be related to a recent expulsion from

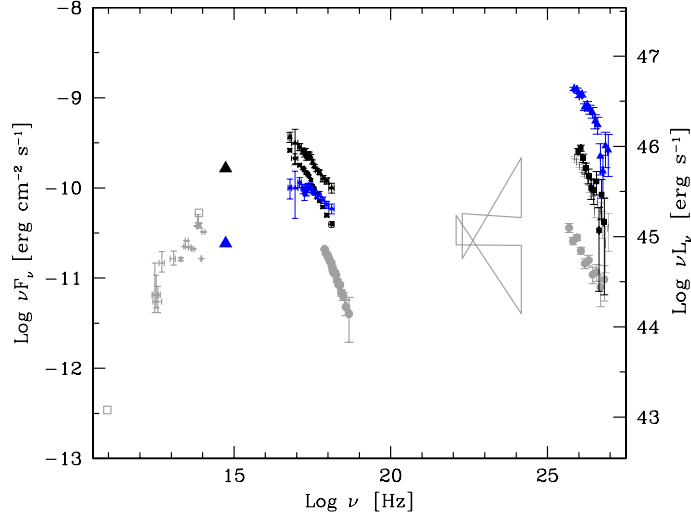


Figure 4.15: Possible SED of the new flaring component in PKS 2155-304, varying beneath the “persistent” emission of PKS 2155-304 (blue triangles, see text). Black points mark the same high and low-state data showed in figure 4.12.

the central engine, of which the extremely fast variability during the Big Flare could be the first manifestation.

Within this two-zone scenario, the cubic correlation measured between the γ -ray and the X-ray flux results from the superposition of the emission from both regions. The large amplitude variations in the VHE domain show that the flaring zone dominates the VHE emission during this night; this is not the case in the X-ray domain, where the smaller amplitude of the variations suggest that the persistent component is dominating the energy output. The measured correlation therefore corresponds to:

$$F_\gamma = F_\gamma^p + F_\gamma^f \approx F_\gamma^f \propto F_x^3 = (F_x^p + F_x^f)^3 = F_x^{p3} + 3F_x^{p2}F_x^f + 3F_x^pF_x^{f2} + F_x^{f3}. \quad (4.2)$$

Therefore, a linear or quadratic dependency between F_γ^f and F_x^f can mimic a cubic relationship between F_γ and F_x for $F_x^f < F_x^p$ (as the F_x^{f3} term is negligible to first order in equation 4.2 in this case). The actual variations of the X-ray emission from the flaring zone can therefore be as large as the γ -ray ones, but are simply seen diluted in the “persistent” X-ray component. The variations at VHE can then be allowed to scale linearly or quadratically with the X-ray variations inside the flaring zone, as required by the specific modeling. Such a scenario is also in agreement with the spectral variations being larger in the VHE band than in the X-ray band (for the same diluting effect). Within this scenario the small amplitude of variations in the optical band compared to the X-ray band, is due to a relatively stronger persistent component at optical frequencies. The lack of correlation between the optical and the γ -ray and X-ray photons can be explained by the fact, that optical photons are emitted by lower energy electrons. The optical band therefore reacts to the electron injection in the rising phase of the flare, but not in the decaying phase, due to the longer cooling times of lower energy electrons.

Within this two-zone scenario, one can try to estimate the highest SED of the flaring component during the simultaneous Chandra and H.E.S.S. observations, as shown in figure 4.15. The γ -ray SED component of the flaring region is to first order given by the highest VHE spectrum in this time window (T300-SIMMAX). In the optical band the flux increase at the flare maximum is 15%, so the optical flux of the flaring region should be ~ 0.15 times the observed optical flux. In the X-ray band the lowest-state spectrum observed at the end of the night (T400-SIMMIN) can be used as background level for the highest-state spectrum

(T300-SIMMAX). The resulting X-ray spectrum of the flaring component has an energy flux of $F_{0.5-5\text{ keV}}^f = 2 \times 10^{-10} \text{ ergs cm}^{-2} \text{ s}^{-1}$, yielding a Compton dominance of ~ 15 (even higher than the observed $L_\gamma/L_X \sim 5$). The X-ray spectrum is well fitted by a log-parabolic model with $\Gamma_{1\text{keV}} = 2.17 \pm 0.06$ and curvature $b = 0.22 \pm 0.11$. This gives an estimate for the synchrotron peak position around 0.4 keV, which is also consistent with the optical flux being much lower than the X-ray flux (see figure 4.15).

A detailed modeling of the SED evolution in this night within the proposed two-zone scenario is beyond the scope of this work, and is currently being worked on within the H.E.S.S. collaboration. Recently, similar multi-zone models have been proposed to explain the VHE observations during the Big Flare (see section 3.4.3). These models will be tested with the multi-wavelength data of this night.

New modes of flaring in HBL

It is interesting to compare this flare of PKS 2155-304 with the other major flaring events observed in both the X-ray and VHE bands, namely from Mkn 421 in 2001, Mkn 501 in 1997 and 1ES 1959+650 in 2002 (for references see section 1.2). There are many common traits: they all display a pre-flare, “persistent” SED with the synchrotron emission peaking in the UV/soft-X-ray band, a steep X-ray spectrum which hardens during the flare pivoting around the UV/soft-X-ray band, and a flare luminosity approximately one order of magnitude higher than the typical source luminosity. The mechanisms and properties of the flare injection seem thus common, but the radiative output differs significantly.

In the previous events such large luminosity was emitted mostly through the synchrotron process, leading to a dramatic shift of the peak position in the SED according to the new peak frequency of the emerging component. The typical Compton luminosity, even at the flare maximum, has always been equal or less than the synchrotron luminosity (using the same EBL model for all sources). In this event, instead, the bulk of the flare luminosity is emitted through the Compton channel, yielding only minor modifications of the overall synchrotron emission.

A bimodality therefore seems to emerge for flaring HBL: either synchrotron dominated or Compton dominated, with the most extreme example possibly provided by the “orphan flare” event of 1ES 1959+650 (see section 1.2). It is intriguing to note that this difference might simply depend on the environment, namely on the location of the flaring zone with respect to the region responsible for the persistent SED: if the new injection/flare is taking place far away, there is little radiative interplay between the two zones, leading to a typical SSC-type flare. When the flare occurs close to it, or close to the black hole where external fields are more intense, the outcome are external Compton-dominated flares. More campaigns targeted on intra-night variability are needed to address this issue, but the diagnostic potential on the jet structure and the location of the “ γ -ray zone” is already very promising.

Chapter 5

The Big Flare as a testbed of Lorentz Invariance

The VHE observations during the Big Flare (see section 3.4) will be used to test Lorentz Invariance (LI) in this chapter. As discussed in section 1.3.1, LI is based on the fact that the speed of light is constant. Particularly, this implies that the speed of light cannot depend on the energy of the photon. Such an energy dependence was however predicted by several models of quantum gravity and can be tested with flares of VHE. The work presented in this chapter was published in an abridged form in Aharonian et al. (2008b) on behalf of the H.E.S.S. collaboration.

5.1 Probing an energy dependence of the speed of light

Albert Einstein’s postulate “*that light is always propagated in empty space with a definite velocity c which is independent of the state of motion of the emitting body*” (Einstein 1905) is one of the pillars of modern physics. Modification of this postulate would lead to LI violations and have far-reaching consequences for our understanding of nature. It is therefore important to constantly improve the verification of its validity. Particularly in the past few decades, a possible energy dependence of the speed of light has been predicted in the framework of quantum gravity models (Alfaro et al. 2002; Ellis et al. 2008; Amelino-Camelia et al. 2005) and effective field theory (Myers & Pospelov 2003), leading to deviations from this postulate (for reviews see Amelino-Camelia et al. (1998); Mattingly (2005); Ellis et al. (2000)). The speed of light modifications have different functional dependencies on the photon energy and helicity in different models. Predictions usually entail free parameters such as the relevant mass scale. However, it is commonly expected that this modification should appear at energies of the order of the Planck energy ($E_P = 1.22 \times 10^{19}$ GeV). For energies much smaller than the Planck energy, a series expansion is therefore expected to be applicable, allowing the energy dependence of the speed of light to be parameterized in a model-independent way (Amelino-Camelia et al. 1998). The photon speed c' is written up to second order in energy E as:

$$c' = c \left(1 + \xi \frac{E}{E_P} + \zeta \frac{E^2}{E_P^2} \right), \quad (5.1)$$

where ξ and ζ are free parameters. Even for the highest photon energies currently measured, the corrections are expected to be very small. However, Amelino-Camelia et al. (1998) suggested that these minuscule modifications can add up to measurable time delays for photons from cosmological sources. At a redshift z , simultaneously-emitted photons, with energies E_1 and E_2 , will arrive at the observer with a time delay $\Delta t = t_1 - t_2$ per energy

difference $\Delta E = E_1 - E_2$ of (Jacob & Piran 2008):

$$\frac{\Delta t}{\Delta E} \approx \frac{\xi}{E_P H_0} \int_0^z dz' \frac{(1+z')}{\sqrt{\Omega_m(1+z')^3 + \Omega_\Lambda}}, \quad (5.2)$$

where $\Omega_m = 0.3$, $\Omega_\Lambda = 0.7$ and $H_0 = 70 \text{ km s}^{-1} \text{ Mpc}^{-1}$ are the cosmological parameters as currently measured. In the case of a vanishing linear term, the mean time delay of the photons per squared energy difference $\Delta E^2 = E_1^2 - E_2^2$ is:

$$\frac{\Delta t}{\Delta E^2} \approx \frac{3\zeta}{2E_P^2 H_0} \int_0^z dz' \frac{(1+z')^2}{\sqrt{\Omega_m(1+z')^3 + \Omega_\Lambda}}. \quad (5.3)$$

The absence of such an energy dispersion has been used to set bounds on the parameters ξ and ζ . Gamma-ray bursts and VHE flares of active galaxies have been the primary targets of these “time-of-flight” studies. For the linear dispersion term in Eq. 5.1, these measurements reach limits of $|\xi| < 70\text{--}150$ (Schaefer 1999; Boggs et al. 2004; Ellis et al. 2006; Bolmont et al. 2008; Lamon et al. 2008; Rodríguez Martínez et al. 2006) for gamma-ray bursts. For active galaxies, dispersion measurements exist for only two sources: Mkn 421 and Mkn 501. Both are located at a similar redshift of ~ 0.03 . For Mkn 421, a limit of $|\xi| < 200$ was set by the Whipple collaboration during a flare in 1996 (Biller et al. 1999). For Mkn 501, an indication of higher energy photons lagging the lower energy ones was reported during a flare in 2005 by the MAGIC collaboration (Albert et al. 2007). This dispersion was recently quantified to $|\xi| \sim 30$ in Albert et al. (2008). Since the signal is however also marginally consistent with zero dispersion, limits of $|\xi| < 60$ and $|\zeta| < 2.2 \times 10^{17}$ were derived (Albert et al. 2008). While limits in ξ from time-of-flight measurements are approaching unity and probing Planck-scale energies, limits on ζ are generally still far from this domain.

Alternative methods to time-of-flight measurements have also been applied to search for an energy dependence of the speed of light. These measurements set more stringent limits relying on additional assumptions: Limits of $|\xi| < 10^{-7}$ are deduced if the speed of light modifications in Eq. 5.1 are helicity dependent (Gleiser & Kozameh 2001; Fan et al. 2007), as predicted by some of the models (Alfaro et al. 2002; Myers & Pospelov 2003). Also, constraining limits of $|\xi| < 10^{-14}$ and $\zeta > -10^{-6}$ were recently reported in Galaverni & Sigl (2008) under several assumptions, for example the sign of the speed of light modification is assumed to be negative or helicity dependent and standard kinematics are required to be valid in a Lorentz-violating regime. While limits from alternative methods are more stringent by orders of magnitude than those currently achieved by time-of-flight measurements, the latter provide the most direct and model-independent test of the constancy of the speed of light with energy.

A caveat of time-of-flight measurements is that dispersion might be introduced by intrinsic source effects, which could cancel out dispersion due to modifications of the speed of light. In the case of a non-detection of dispersion this scenario is unlikely, since it requires both effects to have the same time scale and opposite sign. However, this “*conspiracy of nature*” (Biller et al. 1999) can only be ruled out with certainty by observations of sources at multiple distances, as – in contrast to dispersion from speed of light modifications – source intrinsic dispersion should not scale with distance. Population studies of this kind have been performed for gamma-ray bursts, resulting in limits of $|\xi| < 1300$ (Ellis et al. 2000, 2006; Bolmont et al. 2008; Lamon et al. 2008). For active galaxies the dataset is currently too sparse to perform these studies.

In this work, photon time delays were searched for during the Big Flare of PKS 2155-304. As shown in section 3.4, the light curve shows fast variability ($\sim 200 \text{ s}$) and covers an energy range of a few TeV, providing a perfect testbed. Due to the low energy threshold of the observations, it provides a larger event statistics compared to the Chandra Flare (see chapter 4), allowing a more accurate determination of the dispersion over a wider energy range. In order to quantify the dispersion, time delays between lightcurves of different energies were sought for in an analysis similar to the one applied in section 4.1.3.

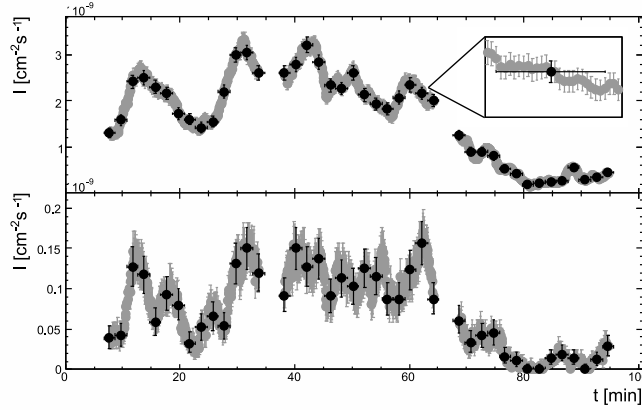


Figure 5.1: Black points show the integral flux VHE lightcurves measured on July 28 from PKS 2155-304 by H.E.S.S. between 200-800 GeV (upper panel) and >800 GeV (lower panel), binned in two-minute time intervals. The zero-time point is set to MJD 53944.02. Gray points show the oversampled lightcurve, for which the two-minute bins are shifted in units of five seconds. The inlay in the upper panel illustrates this in a zoom, where the horizontal error bar shows the duration of the bin in the original lightcurve.

5.1.1 The Modified Cross Correlation function

Time lag between two lightcurves were determined with the Modified Cross Correlation Function (MCCF, Li et al. (2004)). The MCCF is a standard DCF (see section 4.1.3) applied to oversampled lightcurves. This allows time delays below the duration of the flux bins to be resolved (Li et al. 2004) and avoids the systematic error due to the bin duration compared to the analysis presented in section 4.1.3. To optimize the energy gap between two energy bands, while keeping good event statistics in both, the correlation analysis was performed on the lightcurves between 200 and 800 GeV and above 800 GeV (see figure 5.1). The mean difference of the photon energies between the two bands is 1.0 TeV and the mean quadratic difference is 2.0 TeV². The MCCF of these lightcurves is shown in figure 5.3. In order to measure the time delay, the central peak of this distribution was fitted by a Gaussian function plus a first-degree polynomial, resulting in a maximum at $\tau_{\text{peak}} = 20$ s.

The error on the measured time delay is determined by propagating the flux errors via simulations. Ten thousand simulated lightcurves were generated for each energy band by varying the flux points of the original lightcurve within its measurement errors. As the lightcurves are oversampled neighboring bins are highly correlated. This correlation is mimicked by simulating flux variations on a finer time grid, corresponding to the time shift between neighboring flux bins. The exact prescription of this simulations is shown in figure 5.2. The applied method assures that the simulated fluxes are thrown according to the flux measurement errors, taking into account bin correlations. For each pair of simulated lightcurves, the peak of the the MCCF was determined, resulting in a Cross Correlation Peak Distribution (CCPD), shown in the right panel of figure 5.3. The CCPD has an RMS of 28 s and yields the probability density of the error of τ_{peak} (Maoz & Netzer 1989; Peterson et al. 1998). For 21% of the simulations the time delay is negative, therefore the measured time delay of 20 s is not significantly different from zero.

The response of the MCCF to energy dispersion is complex. Primarily, dispersion is expected to shift lightcurves in time according to their mean energy. However, dispersion also broadens their structures and photons might even get shifted out of a burst, decreasing the overall correlation. These “second order” effects become increasingly important once the time shifts approach the time scale of the observed structures in the lightcurve. The response of the MCCF to dispersion was therefore determined by injecting artificial dispersion into

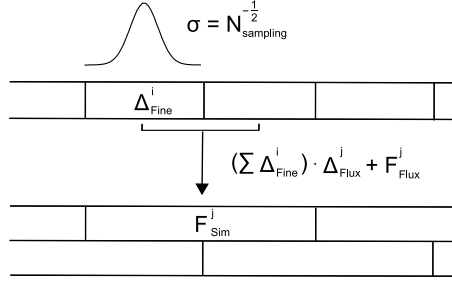


Figure 5.2: Sketch of the method applied in the simulations to take into account bin correlations: Simulated lightcurves are thrown by adding a random values to the measured flux points F_{Flux}^j within the measurement error Δ_{Flux}^j . For this, random numbers Δ_{Fine}^i are thrown according to a Gaussian distribution with a width of $N_{\text{sampling}}^{-\frac{1}{2}}$ on a fine grid (upper row). The simulated error F_{Sim}^j is obtained by adding all thrown Δ_{Fine}^i within the time window of each flux bin and multiplying it with the measurement error Δ_{Flux}^j ; this resulting value is added to the measured flux to obtain the simulated lightcurve (lower row). As can be seen by error propagation, the simulated flux values vary within the flux errors of the measured lightcurve.

the H.E.S.S. data and measuring its effect on the CCPD. As shown in figure 5.4, the CCPD follows the injected time shift per energy linearly for small dispersion values, confirming the expected behaviour. The second order effects mentioned introduce deviations visible at higher dispersion values. These deviations are stronger for a quadratic dispersion in energy, as it generally implies larger time shifts. In order to take these effects into account, the measured time delays are transformed to dispersion-per-energy with the calibration curves shown in figure 5.4. Since the measured τ_{peak} was compatible with zero, 95% confidence upper limits of 73 s TeV^{-1} and 41 s TeV^{-2} are given for the linear and quadratic dispersion respectively.

5.1.2 Systematic tests

The accuracy of the MCCF method was verified with an independent set of simulations. Eleven thousand new photon lists were generated from the real data using a parametric bootstrap method. The parametric model is shown in figure 5.5 and was obtained from a polynomial spline fit to the lightcurves from real data in time bins of one minute. The probability density of the energy distribution of the simulated events was obtained analogously, by fitting the energy distributions of the measured events on a run-wise basis. The CCPD of these new simulations confirmed the previously measured error on the time delay. The shifts of the CCPD for injected dispersion values confirmed the behaviour found in the last section, as shown in figure 5.6.

The effect of the choice of preset parameters was also investigated. Varying the energy ranges and the time binning of the light curves or the fit range of the MCCF peak, within a range of $\sim 100 \text{ GeV}$, $\sim 30 \text{ s}$, $\sim 100 \text{ s}$ respectively, had only a small effect ($< 5 \text{ s}$) on the final result of the dispersion measurements. Finally, it should be noted that the dispersion measurement was also verified with an independent method relying on peak association between lightcurves by Agnieszka Jacholkowska, confirming the presented results. More details on this analysis can be found in Aharonian et al. (2008b).

5.1.3 Limits on an energy dependence of the speed of light

The measured limits on the energy dispersion translate into limits on the energy scale for LI violating corrections to the speed of light with Eq. 5.2 and 5.3. For a linear dispersion

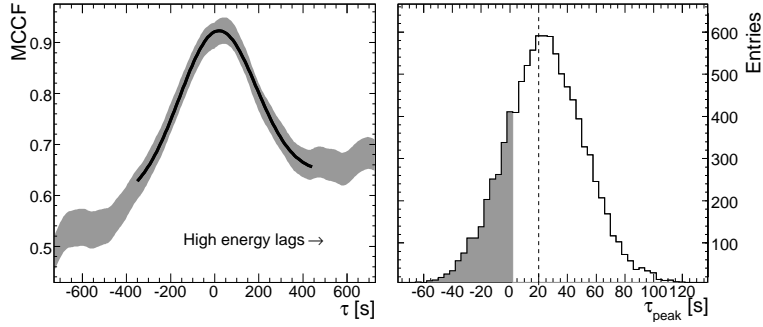


Figure 5.3: *Left panel:* MCCF of the lightcurves in figure 5.1. The black line shows the best fit of a Gaussian plus first degree polynomial. The peak of the fitted function is located at $\tau_{\text{peak}} = 20$ s. *Right panel:* Cross Correlation Peak Distribution (CCPD) obtained from 10000 simulated lightcurves. The shaded area shows the range of the CCPD for $\tau_{\text{peak}} \leq 0$, corresponding to 21% of the total area. The dotted line shows the position of τ_{peak} from the left panel. The CCPD is slightly asymmetric, with a mean of 25 s and an RMS of 28 s

in energy, Eq. 5.2 yields $|\xi| < 17$ (or $|\xi|^{-1} E_p > 7.2 \times 10^{17}$ GeV), at 95% confidence. This limit is the most constraining from time-of-flight measurements to date. For a quadratic dispersion in energy, Eq. 5.3 yields $|\zeta| < 7.3 \times 10^{19}$ (or $|\zeta|^{-1/2} E_p > 1.4 \times 10^9$ GeV).

This measurement opens a new redshift range for population studies of time delays from active galaxies, which are needed to rule out the possibility of time delay cancellation. For a final verdict on this question further VHE observations of active galaxies are needed. The dispersion value from the three blazar measurements to date are shown in figure 5.7 as a function of redshift. While this sample is still very sparse, the result already shows that the time delay reported for Mkn 501 in Albert et al. (2008), if considered significant, is likely due to source intrinsic effects, since speed of light modification would imply higher dispersion values for PKS 2155-304 than the ones found in this chapter.

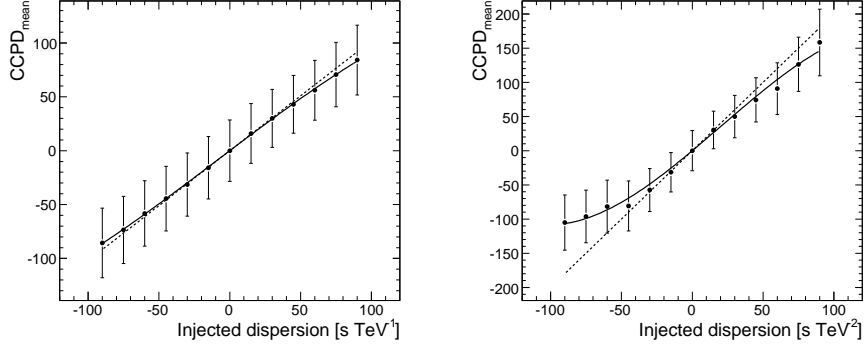


Figure 5.4: Mean of the CCPD as a function of the dispersion injected in the H.E.S.S. data for linear (left) and quadratic (right) dispersion. The points have been shifted by the mean value of the CCPD of the original data shown in figure 5.3 to emphasize the relative time shifts. Each CCPD is derived from ten thousand simulated lightcurves. The error bars show the RMS of distributions. The solid line shows the calibration curve used to transform time shifts into dispersion. For comparison, the dotted line shows the linear response function expected for small dispersion values from the mean energy of the correlated lightcurves (see text).

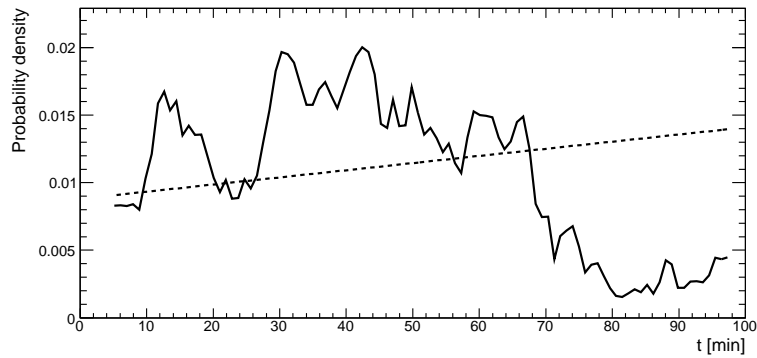


Figure 5.5: Probability densities used for the bootstrap simulations for throwing on-events (straight line) and off-events (dashed line).

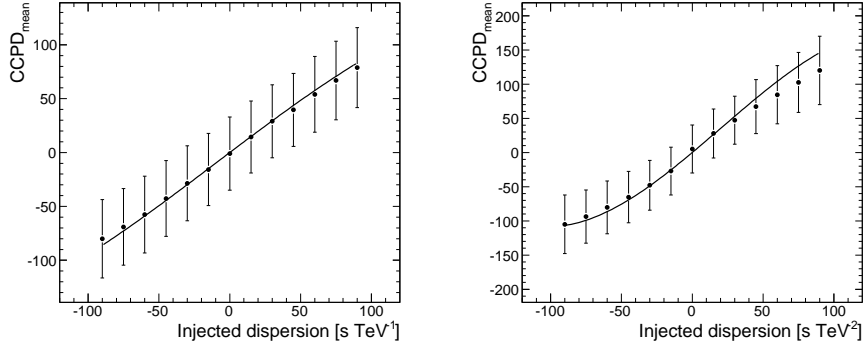


Figure 5.6: Mean of the CCPD as a function of the dispersion injected in the bootstrap simulations for linear (left) and quadratic (right) dispersion. Each CCPD is derived from one thousand simulated lightcurves. The error bars show the RMS of distributions. The solid lines show the calibration curve used to transform time shifts into dispersion from figure 5.4 for comparison.

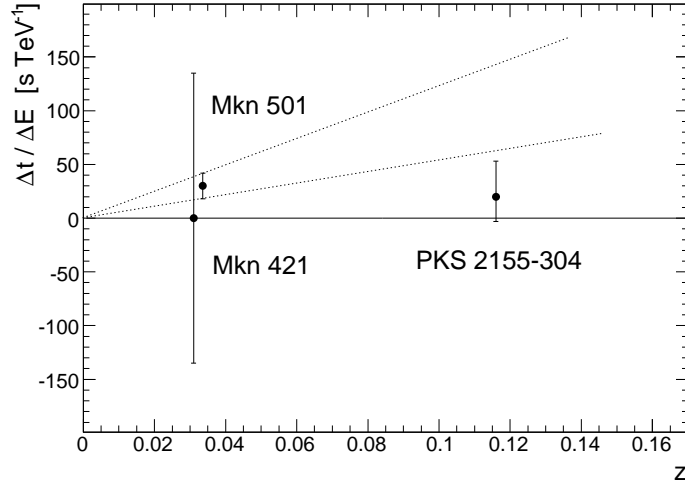


Figure 5.7: Dispersion as a function of redshift for the three dispersion measurements from blazars to date. The dotted lines show the linear extrapolation of the lower and upper error bar for the dispersion measurement of Mkn 501, expected for a linear modification of the speed of light.

Chapter 6

Summary & outlook

An analysis and interpretation of the 2005 to 2007 H.E.S.S. observations of the active galaxy PKS 2155-304 were presented in this work. The source emitted a typically flux of $I_0 = 4 \times 10^{-11} \text{ cm}^2 \text{ s}^{-1}$ above 200 GeV. The observed γ -ray fluxes were close to this value during the entire 2005 and 2007 observation. In 2006, however, PKS 2155-304 was highly active during the observation period of July. In this period, the source showed flux variability on all resolved time scales (from weeks to minutes). On 28 and 30 July, the source exhibited flux values more than two orders of magnitude above the typical flux value. These flares were named Big Flare (28 July) and Chandra Flare (30 July). The fluxes in these nights are among the highest ever observed in VHE astronomy and provided a rich dataset.

The Chandra Flare was simultaneously observed by the Chandra and RXTE satellites in X-rays and by the Bronberg Observatory in the optical band. The exceptional strength of the flare, in combination with the high sensitivity of the involved instruments, resulted in an unprecedented multi-wavelength view of PKS 2155-304. Simultaneous integral fluxes and energy spectra were derived down to two and seven minutes, respectively. The most striking finding of these observations is a cubic decrease of the γ -ray flux as a function of the X-ray flux during the decaying phase of the flare. Such a correlation can not be accounted for within standard Synchrotron Self Compton models and points towards an X-ray emission originating in (at least) two different regions.

The experimental results provided by the Chandra Flare and the rest of the 2005 to 2007 H.E.S.S. observations provided a wealth of information, of which only some aspects could be discussed in the context of blazar models in this work. Many of these findings will be interpreted in more detail in the future, hopefully giving us further insights into the high energy processes taking place in blazars. Some of the most interesting results are:

- The energy output during the flare Chandra Flare was dominated by the Inverse Compton component of the SED ($L_\gamma/L_X = 3 - 6$, depending on the EBL level), something which had not been seen before in High Frequency Peaked BL Lacs, such as PKS 2155-3004
- The absence of any observable time delay within the VHE domain during both flares. Additionally, the multi-wavelength observations during the Chandra Flare revealed no time delay between X-ray and γ -ray photons.
- A spectral hardening with increasing γ -ray flux was measured throughout the 2005 to 2007 observations. Particularly interesting is that the dependency of these two quantities during the Big Flare cannot be explained by a simple analytical function.
- A shift of peak of the high energy component of the SED towards higher energies was observed during both VHE flares. At the same time, no shift of the peak of the synchrotron component was seen during the Chandra Flare.

The VHE observations of the Big Flare were also used to derive limits on the energy scale of Lorentz Invariance (LI) violations. These violations are expected within several quantum gravity models, which predict an energy dependence of the speed of light. Such an energy dependence would lead to an energy dependent dispersion in the VHE emission of PKS 2155-304. The absence of an observable dispersion during this flare was used to set bound on the energy scale of LI violations. The fast flux variability observed during this flare (~ 200 s) allowed the derivation of a stringent upper limit of 73 s TeV^{-1} on a dispersion linear in energy. This upper limit translates into a lower limit of $7.2 \times 10^{17} \text{ GeV}$ on the energy scale of LI violations, which is the most stringent model-independent limit to date.

The results presented in this work show that VHE observations of blazars can give important clues about both the high energy processes taking place in blazars and the validity of LI. Concerning blazar physics, a dense simultaneous multi-wavelength coverage is the key for distinguishing between emission models. The Fermi satellite, launched earlier this year, will give us an important additional piece of information by mapping the SED of blazars between MeV to GeV energies. Regarding the limits on energy dependence of the speed of light, future Cherenkov Telescopes – such as the planned CTA or AGIS – will increase the sensitivity of these studies. Current Cherenkov telescopes can already make these results more robust by measuring the energy dispersion at VHE for sources at different redshifts (this is needed to rule out the possibility that a dispersion due to LI violations is canceled out by source-intrinsic effects). The Fermi satellite will also provide stringent limits on the energy scale of LI violations. This will complement the results obtained from VHE observations, as any hypothetical detection of LI violation would undoubtedly need to be confirmed by different experiments.

Appendix A

List of Very High Energy AGN

Table A.1: List of detected AGN at VHE energies till November 2008. Also listed is the redshift of the source and the reference of the discovery publication. The data was taken from Wagner (2008).

Source	Redshift	Discovery publication
Mkn 421	$z=0.030$	Punch et al., Nature 358 (1992)
Mkn 501	$z=0.034$	Quinn et al., ApJL 456 (1996)
1ES 2344+514	$z=0.044$	Catanese et al., ApJ 501 (1998)
1ES 1959+650	$z=0.047$	Nishiyama, Proc. 26th ICRC (1999)
PKS 2155-304	$z=0.116$	Chadwick et al., ApJ 513 (1999)
1H 1426+428	$z=0.129$	Horan et al., ApJ 571 (2002)
M87	$z=0.0044$	Aharonian et al., A&A 421 (2004)
PKS 2005-489	$z=0.071$	Aharonian et al., A&A 436 (2005)
1ES 1218+304	$z=0.182$	Albert et al., ApJL 642 (2006)
H 2356-309	$z=0.165$	Aharonian et al., Nature 440 (2006)
1ES 1101-232	$z=0.186$	Aharonian et al., Nature 440 (2006)
PG 1553+113	$z>0.09$	Aharonian et al., A&A 448 (2006)
Mkn 180	$z=0.045$	Albert et al., ApJL 648 (2006)
PKS 0548-322	$z=0.069$	Superina et al., 30th ICRC (2007)
BL Lacertae	$z=0.069$	Albert et al., ApJL 666 (2007)
1ES 0229+200	$z=0.140$	Aharonian et al., A&A 475 (2007)
1ES 0347-121	$z=0.185$	Aharonian et al., A&A 473 (2007)
1ES 1011+496	$z=0.212$	Albert et al., ApJL 667 (2007)
3C 279	$z=0.536$	Teshima et al., 30th ICRC (2007)
RGB J0152+017	$z=0.080$	Aharonian et al., A&A 481 (2008)
1ES 0806+524	$z=0.138$	Swordy et al., ATEL #1415 (2008)
W Comae	$z=0.102$	Swordy et al., ATEL #1422 (2008)
S5 0716+71	$z=\text{unknown}$	Teshima et al., ATEL #1500 (2008)

Appendix B

Measurement of the cosmic-ray iron spectrum with H.E.S.S.

The first nine months of this three year thesis I completed a measurement of the cosmic-ray iron flux started during my diploma thesis (Bühler 2005). The measurement relies on a method proposed in Kieda et al. (2001a) to detect heavy nuclei with IACTs from the ground, by resolving the Cherenkov Light they emit prior to their first interaction (the *Direct Cherenkov Light*). The technique was applied to the H.E.S.S. data and yielded one of the most precise measurements of the cosmic-ray iron flux between 10 to 200 GeV. This result and a detailed description of the analysis was published in Aharonian et al. (2007c) under the title “First ground based measurement of atmospheric Cherenkov light from cosmic rays”. In this chapter the content of this publication will be reproduced. The chapter concludes in section B.2 with a description of the improvements made on this analysis during my PhD thesis.

B.1 First ground based measurement of atmospheric Cherenkov light from cosmic rays

B.1.1 Introduction

Motivation

Cosmic rays reach the earth at a rate of approximately $1000 \text{ s}^{-1} \text{ m}^{-2}$. Their energy spectrum is steeply falling and remarkably featureless over ten orders of magnitude in energy (Hörandel 2003). The differential flux is well described by a power law ($\Phi \sim E^{-\gamma}$) with a steepening of the spectrum at a few PeV (the so-called “knee”) and a flattening around 10 EeV (the so-called “ankle”). Despite advances in the field, the origin of cosmic rays is still unresolved. Supernova explosions are thought to be the major contributor at energies up to 1 PeV (Ginzburg & Syrovatskii 1964; Hillas 2006), but conclusive proof is still missing. The High Energy Stereoscopic System (H.E.S.S.; Hinton (2004)) has clearly identified supernova shock waves as sources of high-energy particles (Aharonian et al. 2006c, 2004b). However, the nature of these particles – electrons or cosmic-ray nucleons – remains under debate.

The elemental composition of cosmic rays is similar to the composition of the solar system, if one accounts for propagation effects through the galaxy (Longair 1994). At present the best measurements of elemental spectra in the energy range 1 GeV to 0.5 PeV come from long duration balloon flights (Derbina 2005). Because of the decreasing flux of cosmic rays and the limited collection area of these experiments ($\approx 1 \text{ m}^2$), it is hard to extend such measurements to higher energies. A further improvement in the accuracy and energy range of composition measurements could provide crucial information about the

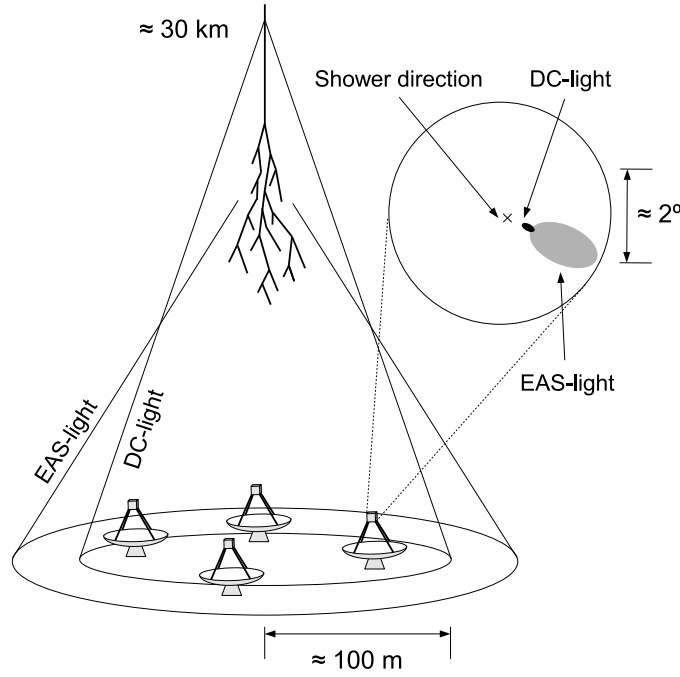


Figure B.1: Schematic representation of the Cherenkov emission from a cosmic-ray primary particle and the light distribution on the ground and in the camera plane of an IACT.

acceleration mechanism and propagation of these particles, and therefore provide further clues about their origin.

In 2001, Kieda et al. (Kieda et al. 2001a) proposed a new method for the measurement of cosmic rays with *Imaging Atmospheric Cherenkov Telescopes* (IACTs). The central idea of this method is to detect the Cherenkov light emitted by *primary* cosmic-ray particles (so-called *DC-light*) from the ground. While DC-light has been measured in the past by balloon experiments (Sood 1983; Clem 2002), the measurement from the ground takes advantage of the huge detection area ($\approx 10^5 \text{ m}^2$) of IACTs, in principle enabling the extension of spectral and composition measurements up to $\sim 1 \text{ PeV}$. Here we review this technique and describe its application to data from H.E.S.S. We present the measurement of the iron spectrum and give an outlook on future applications of this method.

Technique

When cosmic rays enter the atmosphere they emit Cherenkov light above an element-dependent energy threshold. The Cherenkov angle increases with the density of the surrounding medium. The emission angle of the DC-light therefore increases with increasing depth of the primary particle in the atmosphere, creating a light cone on the ground with a radius of roughly 100 m (see Fig. B.1). At a typical height of 30 km the particle interacts and a particle cascade is induced (Extensive Air Shower, EAS). The Cherenkov light from these secondary particles creates a second, wider, light cone on the ground.

The intensity of the DC-light is proportional to the square of the charge Z of the emitting particle, and can therefore be used to identify the primary particle. The challenge for detecting DC-light is to distinguish it from the much brighter EAS-light background (Fig. B.2). Because the DC-light is emitted higher in the atmosphere, it is emitted at a smaller angle than the EAS-light, and is therefore imaged closer to the shower direction in the camera plane. A typical emission angle for DC-light is 0.15° to 0.3° , whereas most of the

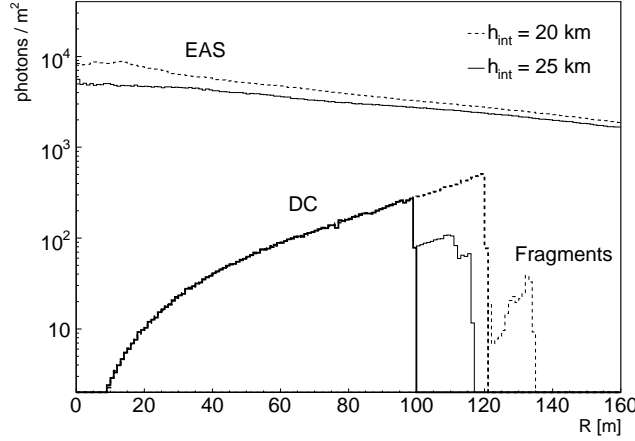


Figure B.2: Simulated intensity distribution on the ground for the EAS-light and DC-light of an individual 50 TeV iron nucleus, as a function of distance from the shower core, for two different first interaction heights (the shower core is defined as the intersection point of the shower axis on the ground). The zenith angle is 0° . The drop in DC-intensity at 100/120 m reflects the first interaction height. The low intensity tail at larger radii is caused by Cherenkov light from fragments of the primary nucleus.

EAS-light is emitted at angles greater 0.4° from the direction of the primary particle (for a more detailed discussion see Kieda et al. (2001a)). Cherenkov cameras, with pixel sizes of $\sim 0.1^\circ$ are therefore able to resolve the DC-emission as a single bright pixel between the reconstructed shower direction and the *center of gravity* (cog) of the EAS-image in the camera plane (Fig. B.1).

Unfortunately, the number of emitted DC-photons also depends on the emission height and on the energy of the primary particle (Fig. B.3). The height of first interaction of hadrons typically varies between 20 to 40 km, hence the total amount of emitted DC-photons of particles with the same atomic number and energy varies significantly. As will be discussed later, this makes the estimation of the primary charge more difficult.

The energy range to which this technique can be applied depends on the charge of the primary particle (Kieda et al. 2001a). At lower energies the limiting factor is that the primary particle momentum must exceed the Cherenkov threshold. At very high energies, the EAS-light outshines the DC-light, making the detection of the latter impossible. The reason for this is that the intensity of the EAS-light increases approximately linearly with energy, whereas the amount of emitted DC-photons remains basically constant above a certain energy (see Fig. B.3).

The aim of the current work is to demonstrate that the technique of DC-light detection can be applied to instruments such as H.E.S.S. to measure the flux of cosmic-ray iron nuclei. Because of their large atomic number and high flux compared to other heavy elements, iron nuclei are well suited for DC-light detection. The lower energy threshold for the detection of these nuclei is ~ 10 TeV.

The H.E.S.S. instrument used for this measurement consists of four IACTs situated in the Khomas highland of Namibia, at a height of 1830 m above sea level. Each telescope is equipped with a 960 pixel camera. Each pixel has an angular diameter of 0.16° , providing a total field of view of 5° diameter. The four telescopes are triggered in coincidence and image the Cherenkov light from EASs. The exact trigger conditions can be found in Funk et al. (2005); Aharonian et al. (2006a) and are far below the applied analysis cuts described in the next section. As will also be described there, the properties of the primary particle

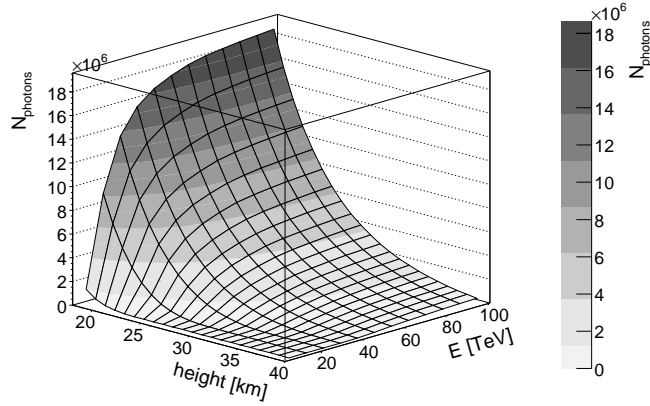


Figure B.3: Total number of emitted DC-photons as a function of energy and first interaction height for an iron nucleus at a zenith angle of 0° , calculated using an atmospheric profile appropriate for the H.E.S.S. site.

(such as direction or energy) can be reconstructed from the shower images.

H.E.S.S. is a γ -ray experiment. The main challenge in detecting γ -rays is to distinguish them from the much larger background of hadronic cosmic rays (see for example Aharonian et al. (2006a)). This background, recorded during normal γ -ray observations, is now used to search for events with DC-light.

B.1.2 Event selection and reconstruction

Shower reconstruction and candidate event selection

As for the standard H.E.S.S. analysis, the raw shower images are calibrated (Aharonian et al. 2004a) and the pixel intensities are corrected to account for the loss of optical efficiency of the system over time (Aharonian et al. 2006a). Afterwards the images are cleaned to remove low intensity substructure in the shower images and hence improve shower reconstruction. The image cleaning consists of a two-staged tail-cut, which requires pixels to have an intensity greater than 20 (10) photo-electrons (pe) and a neighboring pixel with an intensity of 10 (20) pe. Afterwards, an “island cleaning” is applied, where all pixels that are not connected to the pixel with the maximum intensity by neighboring pixels are removed. For a further reduction of shower fluctuations the same procedure is applied again with stronger cuts (200 and 100 pe). By default the soft-cleaned images are used for the shower reconstruction. The strong-cleaned images are only used instead if they contain more than 7 pixels in more than two camera images.

The showers are reconstructed using the standard *stereoscopic Hillas analysis* (Hofmann et al. 1999), whereby the shower (and therefore particle) direction and the intersection point of the shower axis on the ground are reconstructed by intersecting the major axes of the different shower images. The energy of the primary particles is reconstructed from the total image intensity I_{tot} , the impact parameter R_{core} (perpendicular distance from the shower axis to the telescope) and the zenith angle θ , by comparing these parameters to simulations. The mean EAS-light yield at a fixed energy varies with the atomic number of the primary particle, which introduces a systematic shift in the energy reconstruction between different elements. In this analysis all energies are reconstructed under the assumption that the primary particle is an iron nucleus.

This energy reconstruction technique leads to a systematic bias close to the energy thresh-

Parameter	Cut Condition
Q_{DC}	$< 0.14 \ln\left(\frac{I_{\text{tot}}[p.e./161]}{\cos(\theta)}\right)$
$\Delta_{\text{DC}}^{\text{dir}}$	$< 0.45^\circ$
$\Delta_{\text{DC}}^{\text{cog}}$	$> 0.17^\circ$
Δ_{DC}^\perp	$< 0.91^\circ$
R_{core}	$> 40 \text{ m}$
	$< 170 \text{ m}$
$I_{\text{DC-pixel}}$	$< 2500 \text{ pe}$

Table B.1: Cut parameters for DC-pixel detection. For definitions of the parameters see text.

old for detection (Aharonian et al. 2006a). Therefore only events with a reconstructed energy greater than 13 TeV were considered, for which the energy bias is less than 5% (the exact energy value is 12.59 TeV, which corresponds to $\log_{10}(E/\text{TeV}) = 1.1$ and will always be referred to as 13 TeV in the following). Additionally, to avoid images truncated at the camera edge, only images with a center of gravity less than 2° from camera center are used. Finally, to select well reconstructed showers, only events that contain at least two camera images with an *Aspect Ratio* smaller than 0.75 ($\text{Aspect Ratio} \equiv \frac{\text{image width}}{\text{image length}}$) were considered.

DC-light detection

DC-Light can be identified as a single high intensity pixel between the reconstructed shower direction and the cog of the EAS-shower in the camera images (Fig. B.1). The main selection parameter for finding this DC-pixel in the camera image is the *DC-ratio*, defined as:

$$Q_{\text{DC}} = \frac{I_{\text{max.neighb.}}}{I_{\text{pixel}}}, \quad (\text{B.1})$$

where $I_{\text{max.neighb.}}$ is the maximum intensity of the neighboring pixels. The pixel with the minimum Q_{DC} is determined in the relevant angular region in each camera image. The parameters used to constrain this region are the angular distance from the DC-pixel to the shower direction ($\Delta_{\text{DC}}^{\text{dir}}$), to the cog of the EAS ($\Delta_{\text{DC}}^{\text{cog}}$) and to the line connecting these two points (Δ_{DC}^\perp). Afterwards a selection on the impact parameter is applied to ensure that the telescope is inside the DC-light cone. Finally, to avoid detector saturation effects, the intensity of the DC-light candidate pixel $I_{\text{DC-pixel}}$ has to be below the saturation intensity. The exact cut values for the identification of a DC-pixel were optimized using iron simulations and are summarized in Table B.1. To illustrate the applied cuts on one example, the distribution of Q_{DC} for iron nuclei and the cut values are shown in Fig. B.4 as a function of the total image intensity I_{tot} . The mean Q_{DC} value depends on I_{tot} because at higher energies more and more Cherenkov light from secondary particles falls into the angular region of the DC-light, while the DC-intensity remains basically constant above a certain energy threshold.

Once a pixel in the camera image fulfills all the mentioned selection parameters the DC-light intensity I_{DC} is reconstructed by subtracting the mean intensity of the neighboring pixels $I_{\text{neighb.pixels}}$ from the DC-pixel intensity:

$$I_{\text{DC}} = I_{\text{DC-pixel}} - \langle I_{\text{neighb.pixels}} \rangle \quad (\text{B.2})$$

B.1.3 Data analysis and simulations

Simulations

As for all air shower experiments, the present analysis relies on comparisons to Monte Carlo simulations. Simulations are used to calibrate the energy and charge (section B.1.3)

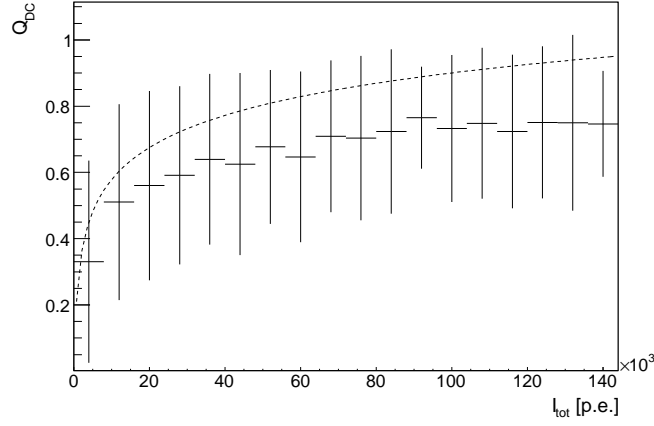


Figure B.4: Mean DC-ratio Q_{DC} as a function of the total intensity of the camera image I_{tot} for iron events from simulations (events which interacted in the atmosphere before passing the Cherenkov energy threshold were not considered since they contain no DC-light). The zenith angle is 0° . The error bars show the RMS of the distribution in each bin. The dotted line shows the selection function given in table B.1.

Z range	representative element	$F_{13}^{200} [10^{-4} \text{ s}^{-1} \text{ sr}^{-1} \text{ m}^{-2}]$
1-6	p (Z=1)	12.6
7-9	O (Z=8)	1.43
10-16	Mg (Z=12)	2.09
17-24	Ca (Z=20)	0.56
25-28	Fe (Z=26)	2.50

Table B.2: Representative element and integrated flux between 13 and 200 TeV, F_{13}^{200} , of the reference composition (Hörandel 2003; Wiebel-Sooth et al. 1998) for the five charge bands of the simulated flux.

estimation and to determine the detection efficiency of the system (section B.1.5). In order to perform a direct comparison between simulations and data, simulations have been produced for five different elements, representative of five different charge bands (see Table B.2). The charge bands cover a Z range from 1 to 28. The contribution of elements with $Z > 28$ is likely negligible: although no flux measurements for these *ultra heavy cosmic rays* exist in the energy region of importance here, measurements of energy spectra for elements with $Z > 28$ at lower energies (George 1999; Hörandel 2003) and flux predictions (Kieda et al. 2001b) in the TeV energy region are more than three orders of magnitude below the flux of the iron band.

The contribution of each charge band to the total simulated flux and the energy distribution of the events inside each band are weighted according to the measured fluxes given in Wiebel-Sooth et al. (1998) and Hörandel (2003) (referred to in the following as *reference composition*). Ref. Wiebel-Sooth et al. (1998) shows a parameterization of the different elemental spectra, obtained by combining measurements from several experiments. The errors given on the absolute flux normalization are $\leq 10\%$. However, they probably do not reflect the entire uncertainty in the spectra, since systematic uncertainties may have been underestimated in the individual data sets (Wiebel-Sooth et al. 1998). Additionally, in the energy range of interest here, specifically for the calcium band, the values given are extrapolated from measurements at lower energies. Ref. Hörandel (2003) presents the same parameterization with more recent data for the proton, helium and iron flux. The normalization of the flux for these elements differs by approximately 25% between the two parameterizations. For the mentioned reasons we assume this difference to be a realistic error in the integral fluxes of the different charge bands between 13 and 200 TeV. In the following comparisons between the data and the simulations, this error is always included. Since the 25% error is still somewhat arbitrary, we will also discuss the effect of a more conservative error of 50% on the presented measurements at the end of this work.

The shower parameters of relevance here depend on the details of high energy hadronic interactions. To assess the systematic errors arising from uncertainties in these interactions, the analysis is performed with simulations based on two independent hadronic interaction models, SIBYLL 2.1 (Fletcher et al. 1994) and QGSJET 01f (Kalmykov et al. 1997). (The newer version QGSJET 02 (Ostapchenko 2006) was not available at the time of the analysis. However, the hadronic interaction uncertainty estimation with QGSJET 01f should be more conservative, since more recent hadronic models are expected to model the interactions more accurately). The simulations for both models were performed using the shower simulation program CORSIKA 6.0321 (Heck 1998). For each model a total of $\sim 10^6$ showers were simulated in an energy range from 1 to 200 TeV. The zenith angle of the simulations was chosen to match the mean zenith angle of the data set (13.6°) described in the next section.

Data

The data considered here were taken between 2004 and 2006 with the full four telescope H.E.S.S. array. Because cosmic rays are deflected by magnetic fields in the galaxy, their flux in the measured energy region is expected to be very close to isotropic (Longair 1994). Therefore it is possible to use all available H.E.S.S. data, independent of the target position. However, to reduce systematic uncertainties due to zenith angle effects on detection efficiencies and energy reconstruction, only data runs with a mean zenith angle smaller than 22° are considered. After standard quality selection criteria and dead time correction, the data set amounts to 357 hours of observation time.

In total, 35364 events in the energy region from 13 to 200 TeV passed the selection criteria. One example of an event with DC-light in all four telescopes is shown in Fig. B.5. High intensity pixels close to the reconstructed shower direction are evident in all four images (indicated by arrows). In agreement with the expected trend from Fig. B.2, the highest/lowest DC-pixel intensity also corresponds to the largest/smallest impact parameter, respectively.

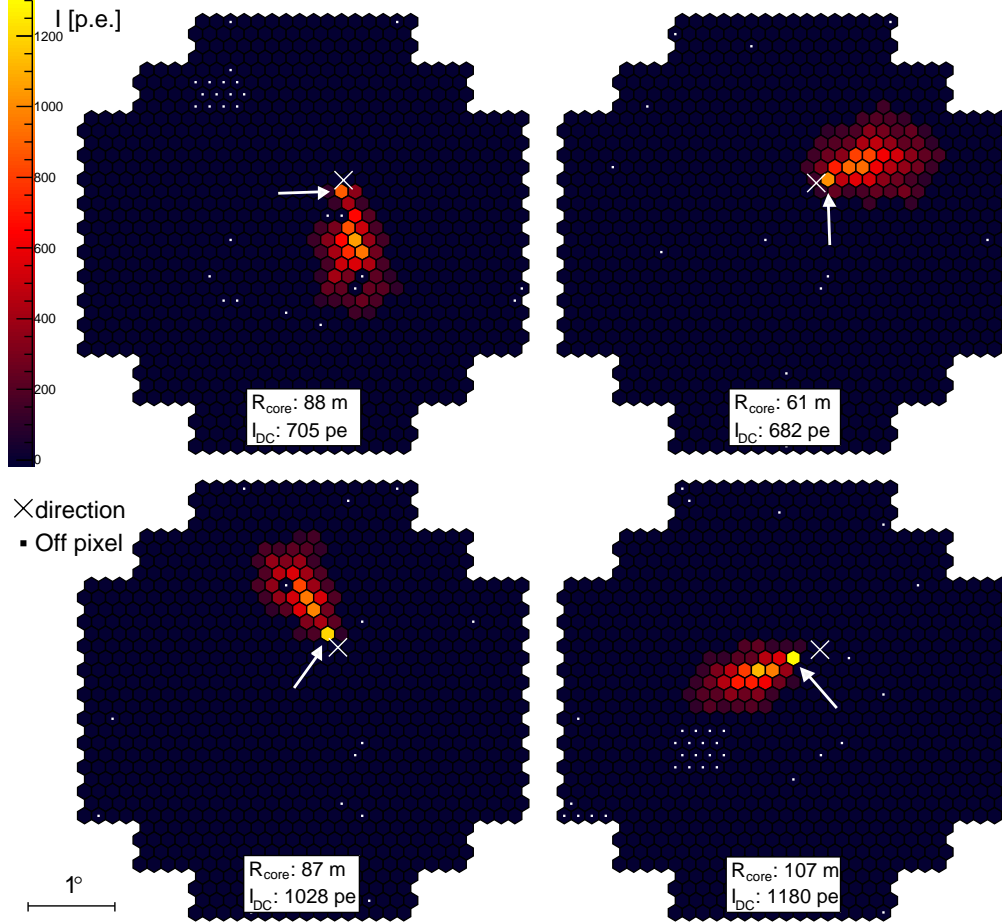


Figure B.5: A measured event with indications of DC-light in all four cameras images (indicated by arrows), after high threshold image cleaning. The reconstructed shower direction is shown by a cross (\times) in each image. The reconstructed energy of this event is 50/48 TeV based on QGSJET/SIBYLL simulations. The reconstructed impact parameter and DC-light intensity for each telescope are shown in the lower panels in each image. The energy and impact parameter resolutions are $\approx 20\%$ and ≈ 20 m, respectively. The white points mark disabled pixels.

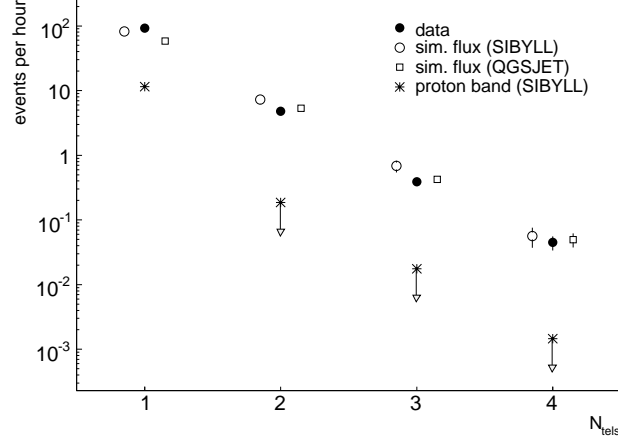


Figure B.6: Event rate for different telescope multiplicities N_{tel} compared to the expected rate from the simulation of the cosmic-ray flux using the SIBYLL and QGSJET interaction models. Additionally, the background event rate from the proton band, estimated using SIBYLL simulations, is shown. No background events were identified for $N_{\text{tel}} \geq 2$ and upper limits are shown (this result is the same for both hadronic models, which is why only the SIBYLL simulations are shown). An upper limit at 95% confidence level is shown for $N_{\text{tel}} = 2$. The upper limits for $N_{\text{tel}} > 2$ are derived under the assumption that they have the same ratio to the detected event rate as the $N_{\text{tel}} = 2$ events. This is a conservative estimate since the fraction of misidentification is expected to decrease with increasing N_{tel} .

Fig. B.6 shows the DC-light detection rate as a function of the telescope multiplicity N_{tel} (number of telescopes in which DC-light is detected simultaneously) for data and simulations for both hadronic models. While the shape of the distributions agrees well, the event rate is higher by $\approx 25\%$ for the SIBYLL simulations. This difference between the models gives an estimate of the systematic error introduced in the analysis due to hadronic interaction uncertainties. Taking this systematic error into account, the simulated rates and the data are consistent.

Background

The detection rate of events with DC-light is expected to have some background due to misidentifications. These misidentifications can occur due to shower fluctuations, which can lead to single high intensity pixels in the EAS-light images. The rate of false detections can be estimated using proton simulations. Protons dominate the cosmic-ray flux in the energy region of interest (see Table B.2). Additionally, protons emit only a negligible amount of DC-light compared to their EAS-light yield at these energies (Kieda et al. 2001a), therefore any detection of DC-light in proton simulations can be considered a fluctuation of the EAS-light yield and therefore a false detection. As shown in Fig. B.6, the expected misidentification rate for the proton band is $\approx 10\%$ of the measured event rate in the data for $N_{\text{tel}}=1$. However, for $N_{\text{tel}} \geq 2$ there are no misidentified events found in the proton band for either hadronic interaction model. The upper limit derived for the misidentification rate for these events is almost two orders of magnitude below the detected event rate in the data. Events with $N_{\text{tel}} \geq 2$ can therefore be considered as essentially background-free.

In order to minimize systematic uncertainties due to background estimation in the presented analysis, only events with $N_{\text{tel}} \geq 2$ were considered. They will be referred to in the following as *DC-events*. In total, 1899 DC-events were found in the data. The resolution of

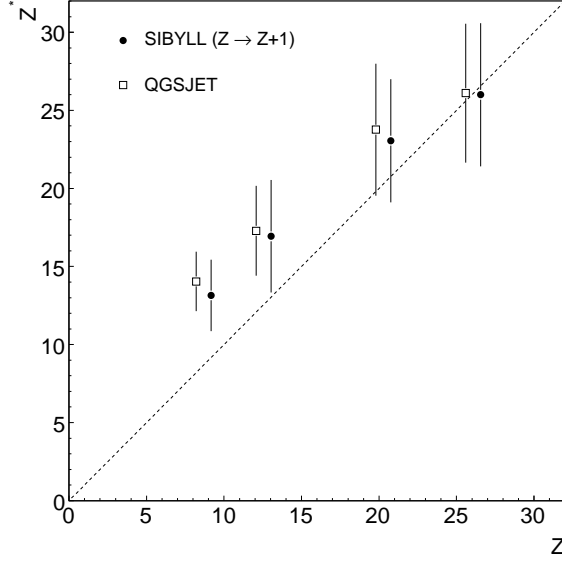


Figure B.7: Mean reconstructed charge Z^* as a function of the true charge Z for DC-events in an energy range of $1.5 < \log_{10}(E/\text{TeV}) < 1.7$ for both hadronic models. For clarity the x-axis is shifted by +1 for SIBYLL. The error bars show the RMS of the distribution in each bin.

the shower parameter reconstruction for these events is $\approx 0.1^\circ$ for the shower direction, ≈ 20 m on the shower core position and $\approx 15\%$ on the primary energy.

Primary charge reconstruction

The elemental composition of the DC-events can be estimated using the Z dependence of the DC-light intensity. The reconstructed charge Z^* is defined as:

$$Z^* = d(E, \theta) \sqrt{I_{\text{DC}}}, \quad (\text{B.3})$$

where $d(E, \theta)$ is a factor that normalizes the mean of the Z^* distribution from iron simulations to the atomic number Z of iron. The energy dependence of d is due to the energy dependence on the number of emitted DC-photons, since the emission for iron nuclei is not saturated in the lower part of the observed energy range (Fig. B.3). The zenith angle θ dependence of d arises from the increasing distance between the average first interaction point to the telescopes with increasing θ .

The charge resolution achieved using Z^* is energy dependent and improves for higher energies, for two principal reasons:

1. The separation of the DC-light intensity distributions, and hence the Z^* distributions, for different elements is maximized when the elements compared have high enough energies that their DC-light emission is saturated. The saturation energy increases with charge. The heaviest element in this analysis is iron, for which the saturation energy is ≈ 50 TeV, which means that the charge separation of Z^* continues to improve up to this energy.
2. A significant fraction of the detected DC-events are dominated by emission from secondary particles created in the first interaction. The reconstructed charge Z^* for these

events is lower than the charge of the primary particle. Simulations show that the fraction of DC-events dominated by the DC-light from secondary particles decreases with energy. For iron it is $\approx 60\%$ at low energies (≈ 13 TeV) and drops to $\approx 35\%$ above the saturation energy.

Fig. B.7 shows the charge resolution obtained in an intermediate energy range for both hadronic models. The charge resolution achieved is not sufficient to assign the charge of the primary on an event-wise basis to one of the four charge bands. However, as will be shown later, it is possible to measure the fraction of elements belonging to the iron band in the data on a statistical basis, and therefore estimate the iron flux.

The main reason for the relatively broad distribution of Z^* for each element is that the DC-light intensity depends not only on the charge of the primary, but also on the emission height of the DC-light (Fig. B.3). The mean emission height is determined by the first interaction height distribution of the primary particles in the atmosphere. As mentioned this varies significantly from event to event, with a FWHM of ≈ 10 km. This dependence on the emission height is one of the reasons for the observed bias in the charge reconstruction at lower atomic numbers, since the mean first interaction height varies between elements. A second reason is that the reconstruction of Z^* is normalized to the charge of iron, which has not saturated its DC-emission in this energy region.

In principle a more accurate measurement of the primary charge could be achieved by constraining the mean emission height h_{DC} . This is possible because h_{DC} is directly related to $\Delta_{\text{DC}}^{\text{dir}}$ and R_{core} via:

$$h_{\text{DC}} \simeq \frac{R_{\text{core}}}{\Delta_{\text{DC}}^{\text{dir}}}, \quad (\text{B.4})$$

This equation follows directly from the geometry of the emission, where $\Delta_{\text{DC}}^{\text{dir}}$ is the mean Cherenkov angle under which the DC-light is emitted. However, in the case of the H.E.S.S. telescope system, little is gained by including the h_{DC} dependence in Z^* , since the pixel size of 0.16° and the spread of the direction and impact parameter reconstruction for DC-events are too coarse to provide a sufficiently precise determination of $\Delta_{\text{DC}}^{\text{dir}}$ and R_{core} . It should be noted that the limited reconstruction accuracy of R_{core} also limits other techniques, such as that proposed in Kieda et al. (2001a), which rely on this parameter.

B.1.4 Systematic checks

Since the reconstruction of the energy spectrum of cosmic-ray iron relies on Monte Carlo simulations, it is important to demonstrate adequate agreement between the measured and simulated distributions of parameters used in the reconstruction. Fig. B.8 shows such comparisons for the impact parameter, the DC-light intensity, the mean Cherenkov angle and the shower maximum X_{max} . The shower maximum is the atmospheric depth at which the maximum number of Cherenkov photons is emitted in the EAS. The panels beneath the distributions show the mean values of the distributions for the data and both hadronic models. The error bars on the simulated points include both the statistical uncertainties and the uncertainty in the cosmic-ray mass composition in this energy regime.

The distributions of R_{core} , I_{DC} and $\Delta_{\text{DC}}^{\text{dir}}$ show a good agreement between data and simulations. Their mean values agree within 1σ . For the height of the shower maximum X_{max} , a shift of $\approx 5\%$ between SIBYLL simulations and the data is apparent. However, no significant shift in this parameter is present in the QGSJET simulations. This difference between the models is again an estimate for the systematic error arising from hadronic interaction uncertainties. Within this systematic uncertainty data and simulations agree reasonably well for X_{max} . However, that the mean X_{max} values for both hadronic models are larger than the data is an indication that there might be additional systematic uncertainties in the reconstruction of this parameter. These could for example come from the uncertainty in the atmospheric profile at the H.E.S.S. site, which is estimated to be $\sim 3 \text{ g cm}^{-2}$. However,

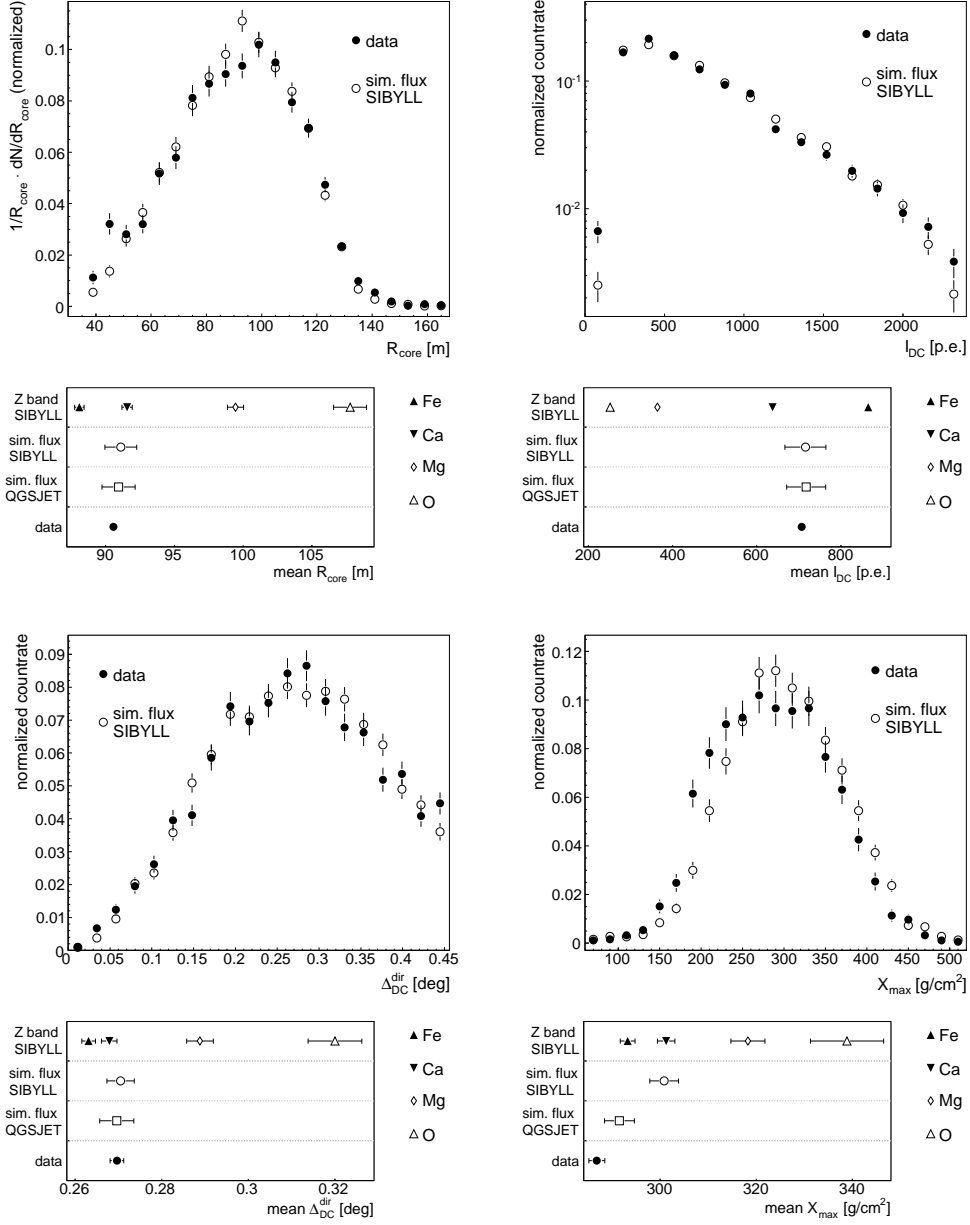


Figure B.8: Comparison of shower parameter distributions for data and simulations of the cosmic-ray flux. The bigger panels show normalized distributions of R_{core} , I_{DC} , $\Delta_{\text{DC}}^{\text{dir}}$ and X_{max} for SIBYLL simulations and data. The smaller panels underneath the distributions show their mean values and the mean value for the different charge bands of which the simulated flux is composed. Additionally, they show the mean value for the distributions for the QGSJET simulations. When comparing the mean values for the simulated fluxes one should bear in mind that roughly equal contributions to the error bars come from statistical errors and from uncertainties in the reference composition, which is the same for both models. The systematic difference between the mean values for the shower maximum X_{max} is not unexpected, since this quantity is difficult to treat in the simulations (see text).

	$\log_{10}(E/\text{TeV})$	$k_{\text{Fe}}^{\text{data}} \pm \Delta k_{\text{fit}} \pm \Delta k_{\text{comp}}$	$\chi_{\text{data}}^2 / \text{ndf}$	$k_{\text{Fe}}^{\text{ref}}$
SIBYLL	1.1-1.3	$0.56 \pm 0.047 \pm 0.026$	6.9/15	0.55 ± 0.09
	1.3-1.5	$0.64 \pm 0.049 \pm 0.027$	31.5/17	0.64 ± 0.08
	1.5-1.7	$0.77 \pm 0.054 \pm 0.019$	15.4/15	0.70 ± 0.07
	1.7-1.9	$0.66 \pm 0.097 \pm 0.013$	12.0/14	0.80 ± 0.06
	1.9-2.3	$0.93 \pm 0.07 - 0.151 \pm 0.008$	3.4/12	0.84 ± 0.04
QGSJET	1.1-1.3	$0.47 \pm 0.050 \pm 0.026$	11.6/15	0.50 ± 0.10
	1.3-1.5	$0.55 \pm 0.059 \pm 0.029$	13.3/17	0.66 ± 0.08
	1.5-1.7	$0.70 \pm 0.063 \pm 0.023$	14.3/15	0.75 ± 0.06
	1.7-1.9	$0.54 \pm 0.128 \pm 0.034$	9.3/14	0.79 ± 0.06
	1.9-2.3	$0.69 \pm 0.160 \pm 0.012$	6.2/12	0.84 ± 0.05

Table B.3: The best fit value of the iron fraction in the data k_{Fe} and the χ^2 values of the fit are shown for both hadronic models in five energy bands. The error of k_{Fe} is composed of the statistical error of the fit Δk_{fit} and the systematic error from the uncertainty in the assumed composition of the lighter nuclei Δk_{comp} (see text). Additionally shown for comparison is the fraction of iron in the simulated cosmic-ray flux ($k_{\text{Fe}}^{\text{ref}}$) for both models.

since no cut is applied on X_{max} , these systematic effect could only affect the results indirectly and must be smaller than the hadronic model uncertainties.

The larger difference between the two hadronic models for X_{max} compared to the other parameters shown is not completely unexpected. The shower maximum depends on the exact modeling of the fragmentation processes in the EAS-shower. The differences in the fragmentation process between hadronic models are well known (see for example Heck (2005), Swordy (2002)). In contrast to the shower maximum, the distributions of R_{core} , $\Delta_{\text{DC}}^{\text{dir}}$ and I_{DC} of the DC-events are dominated by the properties of the DC-light. These are easier to model because they are completely determined by the distribution of the first interaction height for a given energy and atmospheric profile. Since composition measurements with the DC-light technique rely primarily on the DC-light intensity, they are expected to be relatively model independent.

B.1.5 Spectrum extraction

Iron fraction

The first step in the derivation of the flux of iron nuclei is the measurement of fraction k_{Fe} of iron events among the DC-events. k_{Fe} is estimated via a fit of a two-component model to the Z^* distribution of the data. The first component of this model is the Z^* distribution of simulated iron nuclei. The second component is a sum of the Z^* distribution of lighter nuclei. The relative composition of the lighter charge bands (= all except the iron band) is kept fixed to the reference composition, so that k_{Fe} is the single free parameter of the fit.

The fit was performed in five energy bands. The Z^* distribution from the data and the fitted model using SIBYLL simulations are shown in Fig. B.9. The fit results (k_{Fe}) and corresponding χ^2 values (χ_{data}^2) for the fits are summarized in the Table B.3 for QGSJET and SIBYLL. The values for k_{Fe} for the two hadronic models agree with each other within statistical errors Δk_{fit} (the standard deviation of the fit result) for individual energy bands. However, the QGSJET values are shifted by ≈ -0.1 .

Apart from statistical uncertainties, k_{Fe} is affected by the systematic uncertainty in the assumed composition of the lighter nuclei Δk_{comp} . This is estimated by varying the weight of the individual lighter charge bands of the fitted model by 25% and performing the fit for each possible combination. The minimum and maximum deviation between these fit results and the previously obtained k_{Fe} value are then taken as errors on the composition uncertainty. Since these errors are close to symmetric, their absolute values are averaged to give Δk_{comp} .

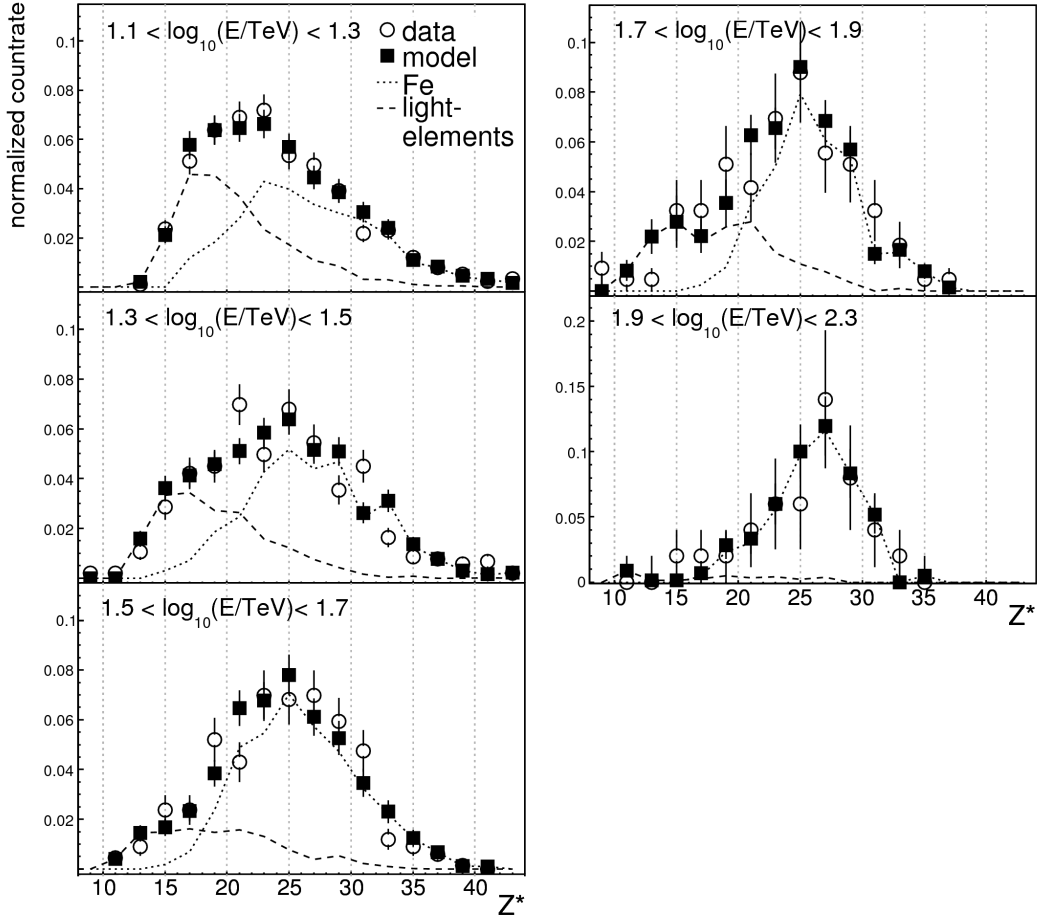


Figure B.9: Z^* distributions of data (open circles) and the fitted SIBYLL model (black boxes) in five energy bands. The curves show the charge distributions of iron (dotted) and of the lighter charge bands (dashed) that compose the fitted model. The fit results are summarized in Table B.3. Note that, as mentioned in section B.1.3, the charge resolution improves with energy, observable by a narrowing of the Z^* distribution of iron with increasing energy.

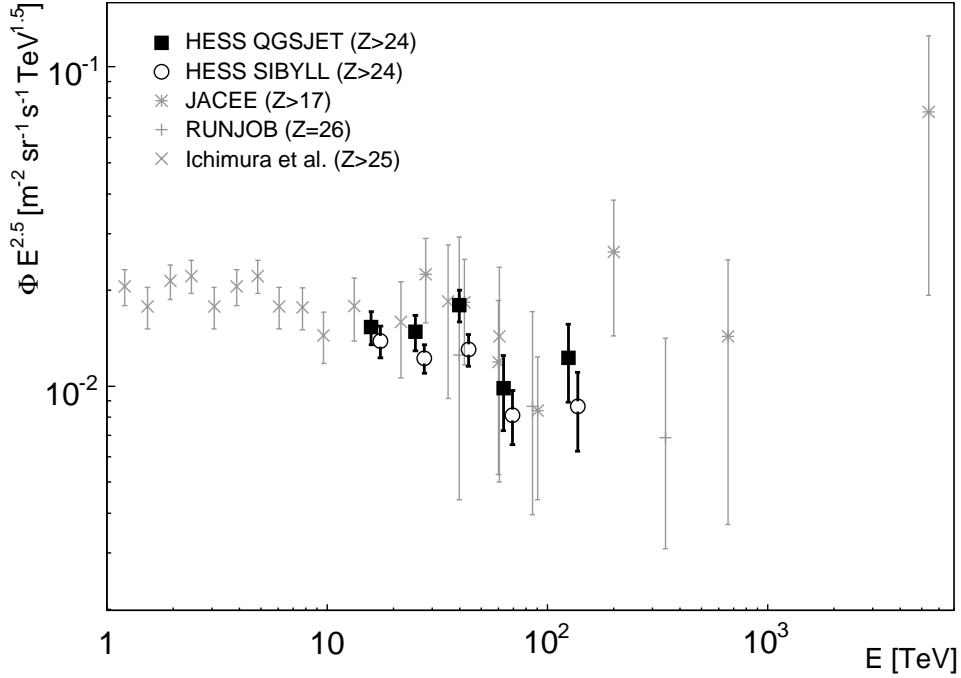


Figure B.10: Differential iron energy spectrum measured with H.E.S.S. for the hadronic models QGSJET and SIBYLL multiplied by $E^{2.5}$ for better visibility of structures. The spectral points for both models are measured for the same energies. For better visibility the SIBYLL points were shifted 10% upwards in energy. The error bars show the statistical errors. The systematic flux error in each bin is 20%. The measurements from balloon experiments with data points at the highest energies are shown for comparison (Asakimori 1995; Derbina 2005; Ichimura 1993) (a compilation with more measurements from balloon experiments and space born measurements can be found in (Hörandel 2003)). For a better visibility no horizontal bars marking the bin ranges are shown, they can be found in the respective papers. When comparing the measurements one should bear in mind that the experiments have different charge thresholds for their definition of the iron band (see legend).

Table B.3 also shows the expected iron fractions $k_{\text{Fe}}^{\text{ref}}$ from simulations of the cosmic-ray flux assuming the reference composition. These values agree with the best fit values. This implies, together with the reasonable χ^2/ndf values of the fits, that no significant deviation from the reference composition can be found in the data. For the iron band this statement will be quantified in the next section.

Iron Flux

Since the identification of DC-events is effectively background-free, the differential iron flux $\phi(E)$ can be estimated as:

$$\phi(E) = \frac{N_{\text{DC}}(E)}{A_{\text{eff}}(E) \cdot \Delta E \cdot t} \cdot k_{\text{Fe}}, \quad (\text{B.5})$$

where $N_{\text{DC}}(E)$ is the number of detected DC-events in the energy interval from E to $E + \Delta E$, t is the total live-time of the dataset and A_{eff} is the mean effective area times the field of view of the detector, averaged over the zenith angle of the observations, taking into account

the efficiency of selection cuts. A_{eff} is derived from simulations of iron nuclei via:

$$A_{\text{eff}} = \frac{N_{\text{DC}}^{\text{MC}}(E) \cdot A^{\text{MC}} \cdot \Omega^{\text{MC}}}{N^{\text{MC}}(E)}, \quad (\text{B.6})$$

where $N^{\text{MC}}(E)$ is the total number of simulated events in the energy interval from E to $E + \Delta E$ and $N_{\text{DC}}^{\text{MC}}$ is the corresponding number of identified DC-events. A^{MC} and Ω^{MC} are the area and angular region over which the simulations were performed.

The energy spectrum is measured in the five energy bins of the k_{Fe} fit. The result is shown in Fig. B.10 for both hadronic models together with the highest energy balloon measurements. The derived spectrum agrees well with these measurements for both models. The measured spectrum is fitted well by a power law $\phi(E) = \phi_0(\frac{E}{\text{TeV}})^{-\gamma}$. The best fit values for the SIBYLL spectrum are given by $\phi_0 = (0.029 \pm 0.011) \text{ m}^{-2}\text{sr}^{-1} \text{ TeV}^{-1}$ and $\gamma = 2.76 \pm 0.11$ with an χ^2/ndf of 3.0/3. For the QGSJET spectrum the best fit values are $\phi_0 = (0.022 \pm 0.009) \text{ m}^{-2}\text{sr}^{-1} \text{ TeV}^{-1}$ and $\gamma = 2.62 \pm 0.11$ with χ^2/ndf of 5.3/3. The integrated flux above 13 TeV is $F(> 13\text{TeV}) = (1.9 \pm 0.7) \cdot 10^{-4} \text{ s}^{-1}\text{sr}^{-1} \text{ m}^{-1}$ for SIBYLL and $F(> 13\text{TeV}) = (2.3 \pm 0.9) \cdot 10^{-4} \text{ s}^{-1}\text{sr}^{-1}\text{m}^{-1}$ for QGSJET.

Since both spectra are derived using the same dataset, the differences in the spectral index $\Delta\gamma = 0.14$ and integrated flux $\Delta F/F = 17\%$ again provide an estimate of the systematic error due to hadronic interaction uncertainties. Additional systematic errors, arising from uncertainties in the atmospheric profile and the absolute detection efficiency of the H.E.S.S. instrument are discussed in detail in Aharonian et al. (2006a) and lead to a systematic error of 20% in the integrated flux and $\Delta\gamma = 0.1$ in the spectral index. The effect of the systematic error Δk_{comp} in k_{Fe} on the spectrum amounts to $\Delta\gamma = 0.015$ and $\Delta F/F = 5\%$. Assuming a more conservative error of 50% in the integral fluxes of the lighter elements in the model of the k_{Fe} fit increases Δk_{comp} by 0.03 on average and leads to errors of $\Delta\gamma = 0.04$ and $\Delta F/F = 11\%$ in the presented spectrum. This error is still small compared to the previously mentioned uncertainties. The total systematic uncertainty of the measurement is therefore estimated to $\Delta\gamma = 0.17$ for the spectral index and $\Delta F/F = 28\%$ for the integrated flux.

The statistical error on the measured iron flux is comparable to these systematic errors. This means that without an improvement in the latter, the total error of the measurement can not be significantly reduced by increasing the exposure time of the data set. However, an increased dataset would enable one to extend the measurement towards higher energies. We note that, despite the systematic uncertainties, the iron flux determined with this technique is one of the best measurements in this energy range. The good agreement between the measured fluxes from balloon experiments and those given here lends confidence to the results from both techniques.

B.1.6 Summary & outlook

A technique for the detection of cosmic rays by resolving the Cherenkov emission from primary particles has been presented and applied to H.E.S.S. data. As a result 1899 events with Direct Cherenkov light in at least two telescopes were detected and it was shown that these DC-events can be considered as background-free. Different parameter distributions of these events were compared to simulations using two different hadronic interaction models and good agreement with the data was found for both. The strong correlation between the DC-light and the charge of the primary shower particle made a charge estimate possible, from which the energy dependent fraction of iron in the data was derived. The energy spectrum of iron nuclei was determined in an energy range of 13 to 200 TeV. The result confirms the flux measurements from balloon experiments with an independent technique and is one of the most precise measurements in this energy range.

Future improvements of the DC-light technique could extend the energy range of the measurement to an energy of ~ 1 PeV. Besides larger statistics, this extension requires additional separation power of the DC-light from the EAS-light. The reason for this is

that the DC-light yield remains constant above a certain energy while the EAS light yield increases approximately linearly with energy. As shown in Kieda et al. (2001a), additional separation power can be achieved using the time structure of the DC-light, since it arrives with a typical delay of 4 ns with respect to the EAS light. This fact could not be exploited in the analysis presented because the H.E.S.S. data used here were taken with the standard integration window of 16 ns. However, current and planned Cherenkov telescopes, which routinely store pulse timing information (Cortina 2005a; Holder 2006), may take advantage of this characteristic.

Due to the strong dependence of the DC-light yield on the charge of the primary particle, the DC-light technique has great potential for composition measurements. The limiting factor is currently the accuracy of shower reconstruction, needed to constrain the emission height of the DC-light. Since the typical shower images in the present work contain ~ 100 pixels, the limitation in the reconstruction accuracy of the shower with the Hillas technique arises from the strong fluctuations in hadronic showers and not from the limited angular resolution of the system. This puts a physical limit to the charge resolution when the showers are reconstructed using this technique.

In order to reduce the sensitivity to shower fluctuations, the DC-light itself could in principle be used to reconstruct the shower. One simple extension of the current method would be to determine the principal axes of the shower images as the line connecting the center of gravity of the image to the DC-pixel. However, exploitation of this technique would require pixels with smaller angular scale for the accurate localization of the DC-light spot. Another possibility, with an array of many nearby telescopes, would be to reconstruct the shower from the DC-light intensity distribution on the ground. Both techniques would take advantage of the very small fluctuations of the DC-emission. A quantitative statement on the level of improvement for both techniques would require detailed simulations and is beyond the scope of this paper.

Finally, the agreement of the distribution of the reconstructed charge Z^* for large charges ($Z^* > 28$) disfavors a significant contribution from ultra heavy elements to the cosmic-ray flux, as expected. It should also be noted that the present analysis is not sensitive to exotic states of matter, such as *quark matter* or *magnetic monopoles* as proposed in Kieda et al. (2001b). The high charges of these states ($Z \gg 100$) imply DC-intensities which would saturate the photomultipliers in the H.E.S.S. cameras.

B.2 Analysis improvements since the diploma thesis

As mentioned in the introduction, the work presented in this chapter was already started during my diploma thesis, after which the analysis was already quite advanced. It included the following components:

- A DC-light detection algorithm based on the selection cuts described in section B.1.2. The DC-ratio was defined as main cut parameter.
- A charge reconstruction algorithm based on multiple parameters, including R_{core} and Δ_{DC}^{dir} .
- An algorithm to provide differential energy spectra for an assumed elemental composition of the detected events.
- A qualitative discussion of the systematic error due to hadronic model uncertainties.

The major improvement during the PhD thesis was the measurement of the iron fraction through the fitting of the reconstructed charge distribution (as presented in section B.1.5). For this, multiple forms of charge reconstruction were tested, yielding the result that the parameters as R_{core} and Δ_{DC}^{dir} do not improve the shower reconstruction; therefore, the simple charge reconstruction described in B.1.3 was chosen. The second major improvement

during the PhD thesis was a quantitative estimate of hadronic model uncertainty. This was done by performing the same analysis with two hadronic models. It was also shown that the distributions of the most important parameters for the DC-light detection agree reasonably well between the data and the simulations for both hadronic models, showing that the systematic errors of the measurement are understood to the level of the quoted values (section B.1.4).

In practice, the made improvements involved a rewriting/structuring of a large fraction of the analysis chain, during which numerous detail improvements were implemented, the most important of which are:

- Correction of the energy, charge and spectrum reconstruction for loss of optical efficiency of the telescope system.
- Inclusion of broken pixels in the estimation of the effective areas.
- Improvement of the DC-light detection algorithm by restricting detections to just one pixel (as opposed to two pixels before). This improves the DC-light reconstruction and lowers the rate of false detections, as less noise enters the measurement.
- Optimization of the selection cuts with the help of simulations (as described in section B.1.2).
- Last but not least, the code was thoroughly checked for possible mistakes. As, in contrast to H.E.S.S. standards, the presented results were not confirmed by a secondary analysis, it was particularly important to assure their correctness.

Bibliography

- Achterberg, A., Gallant, Y. A., Kirk, J. G., & Guthmann, A. W. 2001, MNRAS, 328, 393
- Aharonian, F. 2000, New Astronomy, 5, 377
- Aharonian, F. 2001, in International Cosmic Ray Conference, Vol. 27, I250
- Aharonian, F. 2004, Very High Energy Cosmic Gamma Radiation (World Scientific Publishing Co. Pte. Ltd.)
- Aharonian, F., Akhperjanian, A., Barrio, J., et al. 2002, A&A, 384, L23
- Aharonian, F., Akhperjanian, A. G., Aye, K.-M., et al. 2005a, A&A, 430, 865
- Aharonian, F., Akhperjanian, A. G., Aye, K.-M., et al. 2004a, Astroparticle Physics, 22, 109
- Aharonian, F., Akhperjanian, A. G., Barres de Almeida, U., et al. 2007a, A&A, 475, L9
- Aharonian, F., Akhperjanian, A. G., Barres de Almeida, U., et al. 2008a, A&A, 481, L103
- Aharonian, F., Akhperjanian, A. G., Bazer-Bachi, A. R., & Behera, B. 2007b, Ap. J. Letters, 664, L71
- Aharonian, F., Akhperjanian, A. G., Bazer-Bachi, A. R., & Behera, B. 2008b, Physical Review Letters, 101
- Aharonian, F., Akhperjanian, A. G., Bazer-Bachi, A. R., et al. 2006a, A & A, 457, 899
- Aharonian, F., Akhperjanian, A. G., Bazer-Bachi, A. R., et al. 2005b, A&A, 442, 895
- Aharonian, F., Akhperjanian, A. G., Bazer-Bachi, A. R., et al. 2006b, Nature, 440, 1018
- Aharonian, F., Akhperjanian, A. G., Bazer-Bachi, A. R., et al. 2006c, A&A, 449, 223
- Aharonian, F., Akhperjanian, A. G., Bazer-Bachi, A. R., et al. 2007c, Phys. Rev. D, 75, 042004
- Aharonian, F. A., Akhperjanian, A. G., Aye, K.-M., et al. 2004b, Nature, 432, 75
- Aharonian, F. A., Akhperjanian, A. G., Barrio, J. A., et al. 1999a, A&A, 349, 11
- Aharonian, F. A., Akhperjanian, A. G., Barrio, J. A., et al. 1999b, A&A, 342, 69
- Albert, J., Aliu, E., Anderhub, H., et al. 2007, ApJ, 669, 862
- Albert, J., Ellis, J., Mavromatos, N. E., et al. 2008, Phys. Lett. B in press, 668, 253
- Alfaro, J., Morales-Técotl, H. A., & Urrutia, L. F. 2002, Phys. Rev. D, 65, 103509
- Amelino-Camelia, G., Ellis, J., Mavromatos, N. E., Nanopoulos, D. V., & Sarkar, S. 1998, Nature, 395, 565

- Amelino-Camelia, G., Mandanici, G., Procaccini, A., & Kowalski-Glikman, J. 2005, *International Journal of Modern Physics A*, 20, 6007
- Antonucci, R. 1993, *ARA&A*, 31, 473
- Asakimori, K. 1995, *Proc. 24th ICRC*
- Bell, A. R. 1978, *MNRAS*, 182, 147
- Berezhko, E. G. & Ellison, D. C. 1999, *ApJ*, 526, 385
- Berge, D. 2006, PhD thesis, Universität Heidelberg
- Berge, D., Funk, S., & Hinton, J. 2007, *A&A*, 466, 1219
- Bernlohr, K. 2000, *Astroparticle Physics*, 12, 255
- Bernlöhr, K., Carrol, O., Cornils, R., et al. 2003, *Astroparticle Physics*, 20, 111
- Bettoni, D., Falomo, R., Fasano, G., & Govoni, F. 2003, *A&A*, 399, 869
- Biller, S. D., Breslin, A. C., Buckley, J., et al. 1999, *Physical Review Letters*, 83, 2108
- Blandford, R. D. & Payne, D. G. 1982, *MNRAS*, 199, 883
- Blandford, R. D. & Znajek, R. L. 1977, *MNRAS*, 179, 433
- Boggs, S. E., Wunderer, C. B., Hurley, K., & Coburn, W. 2004, *Ap. J. Letters*, 611, L77
- Bolmont, J., Jacholkowska, A., Atteia, J.-L., Piron, F., & Pizzichini, G. 2008, *ApJ*, 676, 532
- Bolz, O. 2004, PhD thesis, Universität Heidelberg
- Brinkmann, W., Maraschi, L., Treves, A., et al. 1994, *A&A*, 288, 433
- Bühler, R. 2005, Diploma Thesis, Detection schwerer Kerne in der kosmischen Höhenstrahlung mit HESS
- Carini, M. T. & Miller, H. R. 1992, *ApJ*, 385, 146
- Chadwick, P. M. 1999, in *International Cosmic Ray Conference*, Vol. 3, 338
- Chadwick, P. M., Lyons, K., McComb, T. J. L., et al. 1999, *ApJ*, 513, 161
- Chiappetti, L., Maraschi, L., Tavecchio, F., et al. 1999, *ApJ*, 521, 552
- Chiappetti, L. & Torroni, V. 1997, *IAU Circ.*, 6776, 2
- Clem, J. 2002, *Astroparticle Physics*, 16, 387
- Cortina, J. 2005a, *Proc. 29th ICRC*
- Cortina, J. 2005b, *Ap&SS*, 297, 245
- Davies, J. & Cotton, E. 1957, *Journal of Solar Energy Sci. and Eng.*
- de Naurois, M. 2006, *ArXiv Astrophysics e-prints*
- Derbina, V. A. 2005, *The Astrophysical Journal*, 628
- Dermer, C. D. & Schlickeiser, R. 1993, *ApJ*, 416, 458
- Dolcini, A., Farfanelli, F., Ciprini, S., et al. 2007, *A&A*, 476, 1219
- Donato, D., Ghisellini, G., Tagliaferri, G., & Fossati, G. 2001, *A&A*, 375, 739

- Duffy, P., Drury, L. O., & Voelk, H. 1994, *A&A*, 291, 613
- Edelson, R. A. & Krolik, J. H. 1988, *Ap. J.*, 333, 646
- Einstein, A. 1905, *Annalen der Physik*, 322, 891
- Einstein, A. 2002, *The Collected Papers of Albert Einstein; Fundamental Ideas and Methods of the Theory of Relativity*, Vol. 7 (Princeton University Press)
- Ellis, J., Farakos, K., Mavromatos, N. E., Mitsou, V. A., & Nanopoulos, D. V. 2000, *ApJ*, 535, 139
- Ellis, J., Mavromatos, N. E., & Nanopoulos, D. V. 2008, *Physics Letters B*, 665, 412
- Ellis, J., Mavromatos, N. E., Nanopoulos, D. V., Sakharov, A. S., & Sarkisyan, E. K. G. 2006, *Astroparticle Physics*, 25, 402
- Falomo, R., Pesce, J. E., & Treves, A. 1993, *Ap. J. Letters*, 411, L63
- Fan, Y.-Z., Wei, D.-M., & Xu, D. 2007, *Monthly Notices Royal Astronomical Society*, 376, 1857
- Feldman, G. J. & Cousins, R. D. 1998, *Phys. Rev. D*, 57, 3873
- Fermi, E. 1949, *Physical Review*, 75, 1169
- Ferrarese, L. & Ford, H. 2005, *Space Science Reviews*, 116, 523
- Fletcher, R. S., Gaisser, T. K., Lipari, P., & Stanev, T. 1994, *Phys. Rev. D*, 50, 5710
- Foschini, L., Ghisellini, G., Tavecchio, F., et al. 2007, *ApJ*, 657, L81
- Foschini, L., Treves, A., Tavecchio, F., et al. 2008, *ArXiv e-prints*, 0805.0190
- Fossati, G., Buckley, J. H., Bond, I. H., et al. 2008, *ApJ*, 677, 906
- Foster, G. 1996, *AJ*, 112, 1709
- Franceschini, A., Rodighiero, G., & Vaccari, M. 2008, *A&A*, 487, 837
- Funk, S. 2005, PhD thesis, Universität Heidelberg
- Funk, S., Hinton, J., Hermann, G., et al. 2005, in *American Institute of Physics Conference Series*, Vol. 745, *High Energy Gamma-Ray Astronomy*, 753–757
- Gaidos, J. A., Akerlof, C. W., Biller, S. D., et al. 1996, *Nature*, 383, 319
- Galaverni, M. & Sigl, G. 2008, *Physical Review Letters*, 100, 021102
- Georganopoulos, M. & Kazanas, D. 2003, *ApJ*, 594, L27
- Georganopoulos, M., Kazanas D. and Perlman, E., Wingertand, B., Graffand, P., & Castro, R. 2008, <http://jca.umbc.edu/markos/cs/index.html>
- George, J. 1999, *Proc. 26th ICRC*
- Ghisellini, G., Celotti, A., Fossati, G., Maraschi, L., & Comastri, A. 1998, *MNRAS*, 301, 451
- Ghisellini, G. & Madau, P. 1996, *MNRAS*, 280, 67
- Ghisellini, G. & Tavecchio, F. 2008, *MNRAS*, 386, L28
- Ghisellini, G., Tavecchio, F., Bodo, G., & Celotti, A. 2008, *ArXiv e-prints*

- Ghisellini, G., Tavecchio, F., & Chiaberge, M. 2005, *A&A*, 432, 401
- Ginzburg, V. L. & Syrovatskii, S. I. 1964, *The Origin of Cosmic Rays*, New York: Macmillan
- Gleiser, R. J. & Kozameh, C. N. 2001, *Phys. Rev. D*, 64, 083007
- Griffiths, R. E., Briel, U., Chaisson, L., & Tapia, S. 1979, *ApJ*, 234, 810
- Heck, D. 1998, Forschungszentrum Karlsruhe Report, FZKA 6019
- Heck, D. 2005, http://www-ik.fzk.de/~heck/publications/corsika-school2005_modelcompare.pdf
- Heck, D., Knapp, J., Capdevielle, J., Schatz, G., & Thouw, T. 1998, http://www-ik.fzk.de/corsika/physics_description/corsika_phys.pdf
- Heitler, M. . . 1960, *The Quantum Theorie of Radiation* (Oxford, Clarendon)
- Hillas, A. M. 2006, *astro-ph/0607109*
- Hinton, J. 2008, *New Journal of Physics* in print, 803
- Hinton, J. A. 2004, *New Astron. Rev.*, 48, 331
- Hofmann, W., Jung, I., Konopelko, A., et al. 1999, *Astroparticle Physics*, 12, 135
- Holder, J. 2006, *Astroparticle Physics*, 25, 391
- Hörandel, J. R. 2003, *Astroparticle Physics*, 19, 193
- Ichimura, M. 1993, *Phys. Rev. D.*, 48, 1949
- Jacob, U. & Piran, T. 2008, *Journal of Cosmology and Astro-Particle Physics*, 1, 31
- Kalmykov, N. N., Ostapchenko, S. S., & Pavlov, A. I. 1997, *Nucl. Phys. B (Proc. Suppl.)*, 52B, 17
- Katarzyński, K., Ghisellini, G., Tavecchio, F., et al. 2005, *A&A*, 433, 479
- Katarzyński, K., Lenain, J.-P., Zech, A., Boisson, C., & Sol, H. 2008, *MNRAS*, 390, 371
- Kieda, D. B., Swordy, S., & Wakely, S. 2001a, *Astroparticle Physics*, 15, 287
- Kieda, D. B., Swordy, S., & Wakely, S. 2001b, *Proc. 27th ICRC*
- Kirk, J. G., Rieger, F. M., & Mastichiadis, A. 1998, *A&A*, 333, 452
- Kotilainen, J. K., Falomo, R., & Scarpa, R. 1998, *A&A*, 336, 479
- Krawczynski, H. 2008, <http://jelley.wustl.edu/multiwave/spectrum/>
- Krawczynski, H., Hughes, S. B., Horan, D., et al. 2004, *ApJ*, 601, 151
- Kubo, H., Asahara, A., Bicknell, G. V., et al. 2004, *New Astronomy Review*, 48, 323
- Kusunose, M. & Takahara, F. 2008, *ApJ*, 682, 784
- Lamon, R., Produit, N., & Steiner, F. 2008, *General Relativity and Gravitation*, 40, 1731
- Lemoine-Goumard, M., Degrange, B., & Tluczykont, M. 2006, *Astroparticle Physics*, 25, 195
- Li, T.-P. & Ma, Y.-Q. 1983, *ApJ*, 272, 317

- Li, T.-P., Qu, J.-L., Feng, H., et al. 2004, Chinese Journal of Astronomy and Astrophysics, 4, 583
- Longair, M. S. 1994, High Energy Astrophysics (Volume 1,2) (Cambridge Univ. Press)
- Lucek, S. G. & Bell, A. R. 2000, MNRAS, 314, 65
- Ma, C., Arias, E. F., Eubanks, T. M., et al. 1998, AJ, 116, 516
- Maier, G. 2007, ArXiv e-prints, 709
- Malkov, M. A., Diamond, P. H., & Völk, H. J. 2000, ApJ, 533, L171
- Mannheim, K. 1993, A&A, 269, 67
- Maoz, D. & Netzer, H. 1989, Monthly Notices Royal Astronomical Society, 236, 21
- Maraschi, L., Ghisellini, G., & Celotti, A. 1992, ApJ, 397, L5
- Massaro, E., Perri, M., Giommi, P., & Nesci, R. 2004, A&A, 413, 489
- Massaro, E., Tramacere, A., Perri, M., Giommi, P., & Tosti, G. 2006, A&A, 448, 861
- Massaro, F., Tramacere, A., Cavaliere, A., Perri, M., & Giommi, P. 2008, A&A, 478, 395
- Mattingly, D. 2005, Living Reviews in Relativity, 8, 5
- Mazin, D. & Raue, M. 2007, A&A, 471, 439
- Mücke, A. & Protheroe, R. J. 2001, Astroparticle Physics, 15, 121
- Myers, R. C. & Pospelov, M. 2003, Physical Review Letters, 90, 211601
- Nakase, T. 2003, in International Cosmic Ray Conference, Vol. 5, 2587
- Nicastro, F., Zezas, A., Drake, J., et al. 2002, ApJ, 573, 157
- Nolan, S. 2007, in International Cosmic Ray Conference
- Ostapchenko, S. S. 2006, Nucl. Phys. B (Proc. Suppl.), 151, 143
- Osterman, M. A., Miller, H. R., Marshall, K., et al. 2007, ApJ, 671, 97
- Peacock, J. A. 1981, MNRAS, 196, 135
- Perley, R. A., Dreher, J. W., & Cowan, J. J. 1984, ApJ, 285, L35
- Peterson, B. M., Wanders, I., Horne, K., et al. 1998, The Publications of the Astronomical Society of the Pacific, 110, 660
- Piner, B. G. & Edwards, P. G. 2004, ApJ, 600, 115
- Piron, F., Djannati-Atai, A., Punch, M., et al. 2001, A&A, 374, 895
- Pohl, M. & Schlickeiser, R. 2000, A&A, 354, 395
- Punch, M. 2007, International Cosmic Ray Conference
- Ravasio, M., Tagliaferri, G., Ghisellini, G., & Tavecchio, F. 2004, A&A, 424, 841
- Rico, J., de Ona-Wilhelmi, E., Cortina, J., & Lorenz, E. 2007, ArXiv e-prints, 709
- Rieger, F. M., Bosch-Ramon, V., & Duffy, P. 2007, Ap&SS, 309, 119
- Rieger, F. M. & Duffy, P. 2004, ApJ, 617, 155

- Rodríguez Martínez, M., Piran, T., & Oren, Y. 2006, *Journal of Cosmology and Astro-Particle Physics*, 5, 17
- Rolke, W. A., López, A. M., & Conrad, J. 2005, *Nuclear Instruments and Methods in Physics Research A*, 551, 493
- Rosswog, S. & Brüggen, M. 2007, *Introduction to High-Energy Astrophysics* (Cambridge Univeristy Press)
- Schaefer, B. E. 1999, *Physical Review Letters*, 82, 4964
- Sikora, M. 1994, *ApJS*, 90, 923
- Sikora, M., Begelman, M. C., & Rees, M. J. 1994, *ApJ*, 421, 153
- Sikora, M., Błażejowski, M., Moderski, R., & Madejski, G. M. 2002, *ApJ*, 577, 78
- Sood, R. K. 1983, *Nature*, 301, 44
- Stern, B. E. & Poutanen, J. 2008, *MNRAS*, 383, 1695
- Swordy, S. P. 2002, *Astroparticle Physics*, 18, 129
- Tavecchio, F., Maraschi, L., Pian, E., et al. 2001, *ApJ*, 554, 725
- Tramacere, A. 2008, http://www.asdc.asi.it/ssc_at/
- Tramacere, A., Giommi, P., Massaro, E., et al. 2007, *A&A*, 467, 501
- Urry, C. & Padovani, P. 2008, <http://heasarc.gsfc.nasa.gov/docs/cgro/images/epo/gallery/agns/index.html>
- Urry, C. M. & Padovani, P. 1995, *PASP*, 107, 803
- Urry, C. M., Sambruna, R. M., Brinkmann, W. P., & Marshall, H. 1999, *Nuclear Physics B Proceedings Supplements*, 69, 419
- Vestrand, W. T. & Sreekumar, P. 1999, *Astroparticle Physics*, 11, 197
- Vestrand, W. T., Stacy, J. G., & Sreekumar, P. 1995, *ApJ*, 454, L93
- Wagner, R. 2008, <http://www.mppmu.mpg.de/~rwagner/sources/>
- Wagner, S. J. & Witzel, A. 1995, *ARA&A*, 33, 163
- Wandel, A. & Urry, C. M. 1991, *ApJ*, 367, 78
- Weekes, T. C., Cawley, M. F., Fegan, D. J., et al. 1989, *ApJ*, 342, 379
- Wiebel-Sooth, W., Biermann, P. L., & Meyer, H. 1998, *A&A*, 330, 389
- Zhang, Y. H. 2008, *ArXiv e-prints*, 0804.3626
- Zhang, Y. H., Celotti, A., Treves, A., et al. 1999, *ApJ*, 527, 719